Projection of Future Storm Surges around the Korean Peninsula considering Climate Change Effect

Jung-A Yang

2017

Kyoto University
Graduate School of Engineering
Civil and Earth Resources Engineering

Projection of Future Storm Surges around the Korean Peninsula considering Climate Change Effect

Jung-A Yang

2017

Abstract

The long-term assessment of storm surge depending on oceans and regions considering climate effect is one of the important factors in coastal risk reduction.

This study was conducted targeting the Korean Peninsula (hereafter, KP) which located in Northwest Pacific region toward following objectives: (1) to evaluate the reproducibility of the numerical model for a regional scale by considering various typhoons characteristics and topographic features of the coastline, (2) to suggest a method to improve the reproducibility of the numerical model considering topographic characteristics of the coastline, (3) to assess the uncertainties of projection of future storm surge heights (hereafter, SSHs) based on results of ensemble experiments with different global warming scenarios and different spatial patterns of sea surface temperature using a single global climate model (hereafter, GCM) and (4) to project future SSHs based on results of mega ensemble experiments using a single GCM and to identify a storm surge vulnerable region around the KP under the future climate.

The followings were made clear.

- Calculation error of storm surge height was related to the distance between the typhoon and the observatory and the complexity of the topography.
- Bias correction method considering the topography complexity improved the accuracy of the numerical model by 14 % to 23%.
- Vulnerable area to future storm surge and the extent of future SSHs depend on the spatial pattern of sea surface temperature and the global warming scenario.
- SSH around the KP is projected to increase under the future climate except for some areas in the south coast. The magnitude of future change of SSH vary spatially.

It can be considered that the results of this study may lead us to a better understanding of impact of climate change on future storm surge risk.

Acknowledgements

I joined the coastal engineering laboratory, DPRI, Kyoto University in April 2014 and started the study on storm surge. This thesis is achievement of my doctoral course for three years six months. I was able to write this thesis with the help of many people.

I am deeply grateful to my supervisor Associate Professor Nobuhito Mori and Emeritus Professor Hajime Mase of Kyoto University for their support and assistance throughout this study. Their experience and wisdom inspired me and their advice was always invaluable. It was a great pleasure to gain experience in research with their guidance. I also thank Associate Professor Tomohiro Yasuda of Kansai University and Assistant Professor Sooyoul Kim of Tottori University for their assistance.

I would like to thank the Japanese government, specifically the Ministry of Education, Culture, Sports, Science and Technology (MEXT) for the financial support during my doctoral course in Japan.

I am grateful to say my thanks to all of the members of our laboratory. I really enjoyed the laboratory life with them. In particular, I wish to thank Dr. Marc Kjerland and Yu Chida for their kind consideration.

I would like to say thanks to Dr. Heedo Ahn, Dr. Jaeseol Shim and Jinyong Jeong of KIOST and Professor In-Sik Chun of Konkuk University who helped me prepare for studying in Japan.

Finally, I would like to express my gratitude to my parents and parents in-raw giving me the opportunity to be awarded the Ph.D and my husband Daemyeong Song supporting me always as well as our junior who will be born in December 2017.

Table of contents

List of Tables

List of Figures

List of Abbreviations

Abbreviations	Definition
AGCM	Atmospheric Global Climate Model
AS	cumulus convection scheme by Arakawaï Schubert
CGCM	the coupled global climate model
CMIP3	the Coupled Model Inter-comparison Project phase 3
CMIP5	the Coupled Model Inter-comparison Project phase 5
COBE-SST2	Sea Surface Temperature data from Centennial in situ Observation-Based Estimates
CRE	a Cubic Regression Equation
d4PDF	Database for Policy Decision-Making for Future Climate Change
$d4PDF_{future}$	the outputs from future climate experiments of d4PDF
$d4PDF_{past}$	the outputs from past climate experiments of d4PDF
GCM	Global Climate Model
GEBCO	the General Bathymetric Chart of the Oceans
HadISST1	the Hadley Centre Global Sea Ice and Sea Surface Temperature dataset
HFA-rcp26-c0	Climate experiment with CMIP5 mean SST under RCP2.6 scenario
HFA-rcp26-c3	Climate experiment with CMIP5 cluster3 SST under RCP8.5 scenario
HFA-rcp45-c0	Climate experiment with CMIP5 mean SST under RCP4.5 scenario
HFA-rcp85-c0	Climate experiment with CMIP5 mean SST under RCP8.5 scenario
HFA-rcp85-c1	Climate experiment with CMIP5 cluster1 SST under RCP8.5 scenario
HFA-rcp85-c2	Climate experiment with CMIP5 cluster2 SST under RCP8.5 scenario
HPA	Climate experiment under present condition
IBTrACS	the International Best Track Archive for Climate Stewardship
IPCC AR4	the Fourth Assessment Report of the Intergovernmental Panel on Climate Change
KF	cumulus convection scheme by Kainï Fritsch
KP	Korean Peninsula
LRE	a Linear Regression Equation
MRI-AGCM3.2H	Atmospheric Global Climate Model with 60 km resolution developed by the Japanese Meteorological Research Institute
NTC	National Typhoon Center
RCP	the Representative Concentration Pathway

Abbreviations	Definition
SIC	sea-ice concentration
SIT	Sea-Ice Thickness
SSH	Storm Surge Height / Sea Surface Heights
SST	Sea Surface Temperature
SuWAT	a coupled Surge, WAve and Tide model
SWAN	Name of a third-generation wave model ñSimulating Waves Nearshoreò
TC	Tropical Cyclone
WMO	World Meteorological Organization
YS	cumulus convection scheme by Yoshimura

Chapter 1.
Introduction

1.1 Background of the research and its main objective

Almost two-thirds of the world population (about 4.6 billion people) live within 60 km from the coastline with potentially high risk by natural disaster (The United Nations Atlas of the Oceans, 2016). Tropical cyclones generating extreme winds, rainfall and storm surge are one of the elements that pose hazards to low lying coastal areas. Among the tropical cyclone-related disasters, salt water flooding associated with storm surge is the primary cause of death (WMO, 2006). There were several severe tropical cyclones in the last 50 years. Cyclone Bhola caused up to 300,000 deaths in Bangladesh in 1970. In the United States, Hurricane Katrina in 2005 inflicted the death of over 1,800 people and property damage of approximately $81 billion. In 2013, Typhoon Haiyan struck the Philippines, causing 5,982 fatalities with an additional 1,799 missing and 27,022 injured and economic losses to the tune of US$802 million (Anthes, 1982; Knabb *et al.*, 2005; National Disaster Risk Reduction and Management Council, 2013). Storm surge is defined as the sea level rise above the astronomical sea level caused primarily by storm winds and secondarily by the surface pressure drop near the storm center. The long-term assessment of storm surge is one of the important factors in coastal risk reduction.

According to recent studies, it is expected for global climate change to lead to sea level rise (IPCC AR4, 2007) and more severe tropical cyclones (Emanuel, 2005; Webster *et al.*, 2005; Elsner *et al.*, 2008; Rozynski *et al.*, 2009; Kuntso *et al.*, 2010, Bender *et al.*, 2010; Schiermeier, 2010; Woodruff *et al.*, 2013). As results, it is anticipated that future storm surge heights (hereafter, SSHs) and other coastal disaster aspects will be changed depending on oceans and regions. Therefore, quantifying the impact of climate change on tropical cyclone-induced storm surges requires explicit modeling of the development of storms and induced surges at regional scales under projected climates (Lin *et al.*, 2012; Mori and Takemi, 2016).

The Korean Peninsula (hereafter, the KP) is located in the Northwest Pacific. Two coasts of the KP, west and south, have suffered from storm surge damage due to its topographic features. The western coast of the KP is an area of geological submergence and tidal flats up to 1,700 km^2 are exposed at a low tide. In this area, tidal variations are large, reaching up to 10 m at Kyunggi Bay (Kim, 2007). When typhoons hit the area at a high tide, this area is vulnerable to flooding. The southern coast of the KP has a complex coastline with hundreds of islands. Its complex topography can amplify SSHs but it also makes it difficult to conduct numerical modeling for storm surge. Historically, as the KP is located in the pathways of typhoons, it has been directly and indirectly affected by an average of three typhoons every year from 1904 to 2015 (NTC, 2016). These typhoons which directly and indirectly affected the KP have become influential over the years as the typhoons become more intense (Park *et al.*, 2006; Oh *et al.*, 2011; Ahn *et al.*, 2008; Choi and Kim, 2007; Choi and Moon, 2008). Owing to topographic and geographical factors of the KP, the western and southern coasts of the KP actually suffered from storm surge-induced disaster several times in the past (refer to Figure 1.1).

In addition to the topographic and geographical characteristics of the KP, the regional sea level rise due to climate change around the KP is expected to be higher than the global average (IPCC AR4, 2007). Furthermore, it is anticipated that the total number of tropical cyclones affecting the northwest Pacific region will decrease while the frequency of tropical cyclones with very high intensity will increase (Mori and Takemi, 2016). These factors raise concern about increased storm surge disasters in East Asia (Yasuda *et al.*, 2014; Kim *et al.*, 2014). To reduce the damage resulting from storm surge, much research has been carried out targeting the KP: 1) development and operation of storm surge forecast and warning systems by numerical simulations (e.g. Park *et al.*, 2009; Kwon *et al.*, 2007; You and Seo, 2009; Suh *et al.*, 2012), 2) projection of future storm surge height (e.g. Yang and Kim, 2014; Hur *et al.*, 2006(a); Hur *et al.*, 2006(b) ; Moon *et al.*, 2006), 3) flood inundation mapping considering climate change (e.g. Moon *et al.*, 2007; Kang *et al.*, 2010) and 4) development of disaster countermeasure technology for flood-prone areas (e.g. Shim *et al.*, 2017).

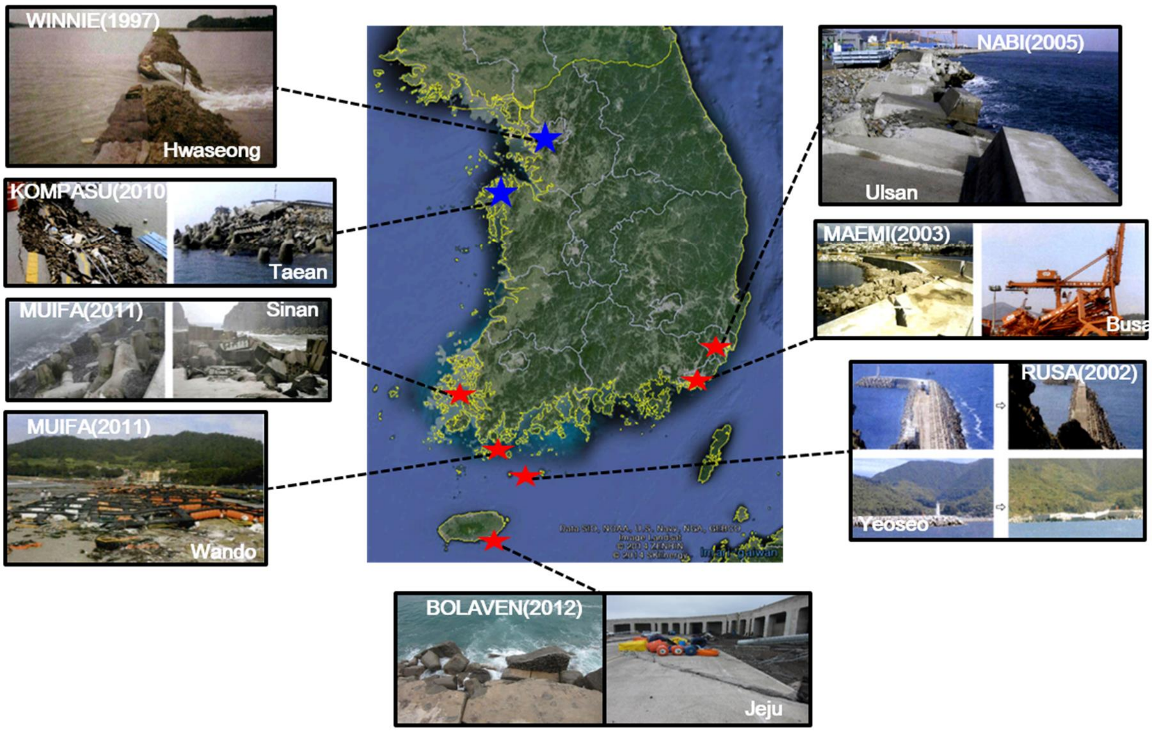

Figure 1.1 Storm surge-induced disasters along the KP in the past

However, there are some limitations of previous studies related to projection of future storm surge height. First, the target area for projecting future SSHs is limited to one or a few specific locations (e.g. Yang and Kim, 2014; Hur *et al.*, 2006(a); Moon *et al.*, 2006). There are few studies discussing regional scales (e.g. Hur *et al.*, 2006(b)). Though it is important to identify vulnerable points after projecting future storm surge height on a regional scale for policy making to prioritize where to take action and to find appropriate site-specific solutions against the SSHs in the future climate condition along the coastlines (Vousdoukas *et al.*, 2016; Lapidez *et al.*, 2015), studies for regional scales should be undertaken promptly.

The second limitation is the inadequacy of the numerical model verification. Many researchers have validated numerical models by adjusting the values of the physical parameters in the model to obtain simulated SSHs values close to the observed values for a particular typhoon at a particular location/site (e.g. Takayama *et al.*, 2004; Shibutani *et al.*, 2015; Nakajo *et al.*, 2015). However, it is not generalizable for other locations, events, and model configurations, as hindcasting a specific typhoon-induced storm surge has uncertainties depending on topographic features, typhoon characteristics and model configurations. In particular, the complex coastline in the southern coast of the KP makes it difficult to carry out accurate storm surge simulations. For example, Takayama *et al.* (2004) described numerical reproducibility of the storm surge in Masan and Busan which are located in the southeastern coast of the KP caused by Typhoon Maemi in 2003. It was revealed that under the same model configurations the storm surge in Busan can be numerically reproduced with high accuracy, but the one in Masan is approximately 1 m smaller than the observed one. In other words, the degree of accuracy of the numerical model for a single point within a target region does not represent those of other points in the area. Thus, when performing model validation to project future SSHs for a regional scale, accuracy assessment of the numerical model for a regional scale is required.

The last limitation is the use of the unscientific typhoon information to project future SSHs. In previous studies, the projection of future SSHs and flood inundation mapping considering climate change effect were conducted based on typhoon scenarios by combining the characteristics of past events (e.g. Hur *et al.*, 2006 (b); Moon *et al.*, 2007). This method lacks scientific support because meteorological dynamics are not ensured. Additionally, it is difficult to estimate the return level and the return period which are used as important information to estimate the freeboard of the structures near the coastal zone for coastal disaster prevention under climate change.

Therefore, the main purposes of this study are:

(1) To identify a storm surge vulnerable region around the KP under the past climate

(2) To evaluate the reproducibility of the numerical model for a regional scale by considering various typhoons characteristics and topographic features of the coastline

(3) To suggest a method to improve the reproducibility of the numerical model considering topographic characteristics of the coastline

(4) To assess the uncertainties of projection of future SSHs based on results of ensemble experiments with different global warming scenarios and different spatial pattern of SSTs using a single global climate model (hereafter, GCM)

(5) To project future SSHs based on results of mega ensemble experiments using a single GCM

(6) To identify a storm surge vulnerable region around the KP under the future climate

1.2 Organization of the thesis

The structure of this manuscript is organized in six chapters including this introduction. An overview of the content of each chapter is given below.

In Chapter 2, the storm surge-prone area where high SSHs have occurred and the properties of typhoons that resulted in the high SSHs are identified by analyzing historical tidal data from tidal stations around the Korean Peninsula. Then, a series of storm surge hindcasts are conducted for this area by the historical typhoons that caused extreme SSH. The reproducibility of the numerical model is evaluated according to typhoon characteristics and different terrain characteristics.

Chapter 3 suggests a formula for bias correction between the observed SSHs and the calculated SSHs using a geographic parameter, in particular the coastline complexity factor, to improve the reproducibility of the numerical model considering model resolution. First, we draw a relational expression between bias and coastline complexity factors. Next, the degree of coastline complexity at each location in the target area is calculated using the concept of fractal dimension and then bias is expressed as a function of the degree of coastline complexity by deriving regression equations between them. Finally, the verification of this bias correction method and the estimation of the effect on the projection of potential maximum SSHs are conducted.

Chapter 4 assesses the uncertainties of the projection of future SSHs based on results of ensemble experiments using a single GCM, denoted MRI-AGCM3.2H which was developed by the Japanese Meteorological Research Institute (Mizuta *et al.*, 2012). The ensemble experiments were carried out in consideration of various kinds of sea surface temperatures and climate change scenarios. The elements which can influence future SSHs around the KP are investigated.

In Chapter 5, the future SSHs around the KP is projected based on the typhoons extracted from the results of mega-ensemble experiments with the MRI-AGCM3.2H (Mizuta *et al.*, 2016). The assessment of a return level of extremely low frequency such as once every 100, 500 and 1,000 years are performed.

Finally, the major findings are summarized in Chapter 6.

Chapter 2.

Hindcasting of historical storm surge events in the Korean Peninsula

In this chapter, the first storm surge-prone areas where high storm surge heights historically occurred are examined and the properties of typhoons that resulted in the high storm surge heights/sea surface heights (abbreviated as SSHs) are identified by analyzing observed tidal data at tidal stations installed around the Korean Peninsula (hereafter, KP). Then, a series of hindcasting of storm surge targeting these areas is conducted. Finally, the reproducibility of the numerical model is evaluated according to typhoon characteristics and different terrain characteristics.

2.1 Historical storm surge events and observed tidal data along the Korean coast

According to the National Typhoon Center (NTC, 2016), the KP was impacted directly and indirectly by 345 typhoons from 1904 to 2015, on average three typhoons per year. As it is too expensive to hindcast all storm surge events by all of the typhoons that affected the KP historically, this study considers only typhoons that produced SSHs higher than 1.0 m around the KP.

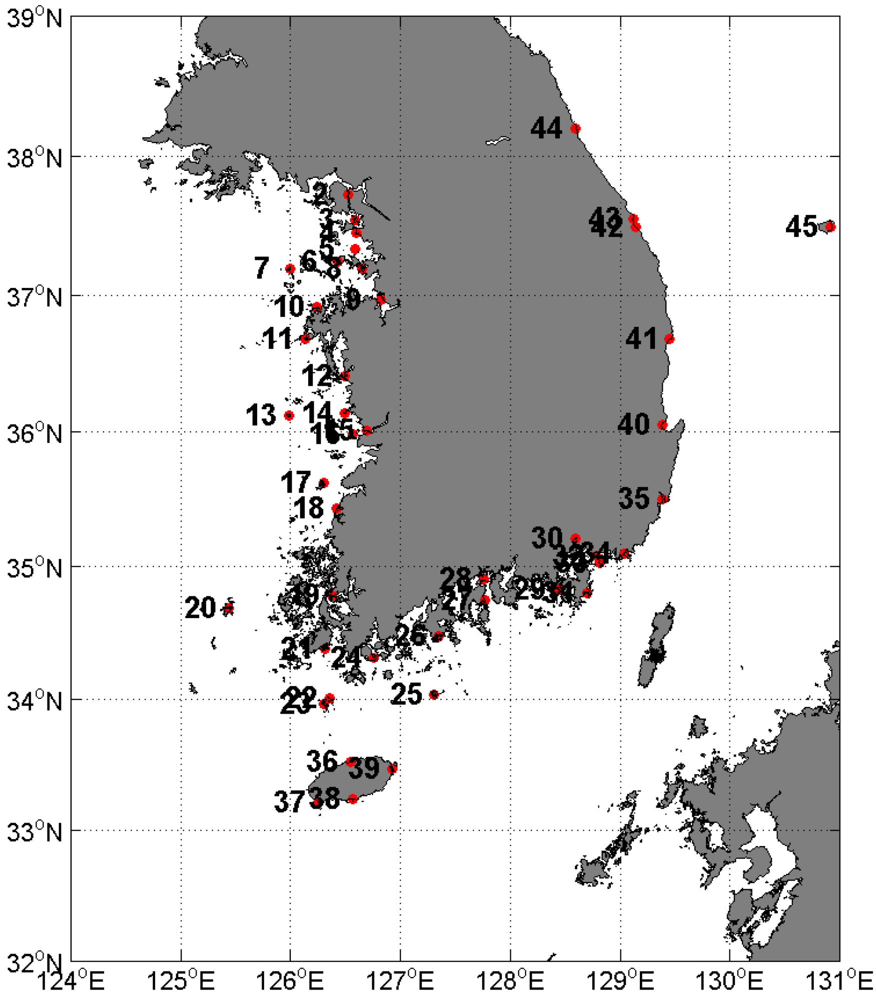

Figure 2.1 Forty-five tidal stations located along the KP. Each number in the left of red circles is tidal stationôs numbers by KHOA numbering

Since the installation of the first tidal station in 1952, forty-five tidal stations have been established along the coast of the KP (shown by red circles in Figure 2.1) and have been operated by the Korea Hydrographic and Oceanographic Agency (hereafter, KHOA). Observed tidal data from each tidal station are available in the Korea Real Time Database for Near-GOOS (http://www.khoa.go.kr/koofs/eng/observation/obs_real.do). The observed tidal data is provided in two types with different temporal resolutions: one hour and one minute interval, respectively. However, the data with one minute interval is only provided since 2000. In this study, the observed tidal data with one hour interval from 1979 to 2013 between May to October (hereafter referred to as the target period) is analyzed to recognize the area vulnerable to storm surge where high SSHs occurred in the past and the properties of typhoons which resulted in the high SSHs. The reason for using only the tidal data observed between certain months is that the historical typhoons only passed the around Korean Peninsula between May and October (NTC, 2016). Figure 2.2 shows the status of observed tidal data for each station used in this study. The temporal extent of the observed tidal data varies among regions. The rate of the acquired tidal data are 34 %, 64 % and 72 % in the western area, the southern area and the eastern area of the KP, respectively.

Figure 2.2 Temporal availability of observed tidal data at each tidal stations. Each line corresponds to a different station, while colors correspond to the 3 different region along the KP. (Green : the western area, Yellow : the southern area, and blue : the eastern area)

2.2 Identification of the storm surge-prone in Korea

The observed SSH is in general obtained by subtracting astronomical tide from observed tidal data. We calculated the astronomical tide at each tidal station by performing a harmonic analysis on the observed tidal data during that period. The T_TIDE package (Pawlowicz *et al.*, 2002) was used for harmonic analysis. T_Tide is a MATLAB package based on a FORTRAN harmony analysis program written by Foreman and Neufeld (1991) and Godin (1991). It can perform classical harmonic analysis for tidal periods of about 1 year or shorter with nodal corrections, inference, and other user-specified options by simply entering a command line, ñt_tideò in a Matlab code. In this study, the 35 constituents chosen from the automated constituent selection algorithm were considered for the harmonic analysis. Only those constituents with a SNR (which is the abbreviation of signal to noise ratio) greater than 1 were regarded as significant constituents for computation of the astronomical tide. Nodal corrections are performed. A linear trend is included in the analysis. As additional user-specified options, linearized error analysis that assumes an uncorrelated bivariate coloured noise model were applied for calculation of confidence limits and a value of resolution criterions for least-squares fit was applied to 0.9.

As a result of calculating the storm surge height at each tidal station during the target period, high storm surge heights of over 1 m were observed 73 times along the coast. Note that the number of 73 events included the same typhoon induced surge and it was needed to figure out the actual number and events. Only 14 events out of the 73 events were caused by different typhoons and all of them occurred since 2000 (refer to Table 2.1). The highest SSH resulted from typhoon is 1.62 m which was caused by Typhoon Maemi observed at Tongyeong tidal station. However, this value is smaller than the value reported in the literature of storm surge disaster survey caused by Typhoon Maemi (2.5 m at Masan tidal station, Takayama *et al.*, 2004). They calculated the SSH using observed raw tidal data. The observed tidal data with one hour interval used in this study were provided after being subject to various levels of data quality control by KHOA. It is assumed that this discrepancy result from that the raw observed data value was modified in the data quality control process and a difference in prediction method of the astronomical tide.

Thus, the SSH at each tidal station were recalculated using the raw observed tidal data with one minute interval. The results are shown in Table 2.2. High SSH of over 1 m induced by abnormal weather conditions were observed 209 times throughout the coast. Only 18 events with SSH higher than 1 m out of the 209 events resulted from each different typhoon. The SSH higher than 1 m were observed at 10 tidal stations in the southern coastal area and at 3 tidal stations in the western coastal area; Tidal stations in the southern coast area are named Yeosu (3 occurrences), Masan, Goheung, Ulsan, Gadeokdo (twice occurrence), Yeonggwang, Jindo, Wando (twice occurrence), Jeju, and Seogwipo (twice occurrence) and the tidal stations in the western coastal area are named Inchoen, Boryeong, and Ansan. Nine out of eighteen occurrences were observed in the southeastern coastal area of the Korean Peninsula. In the analysis of data with one minute interval, storm surge heights higher than 2 m, which were absent in the analysis of the data with one hour interval were measured twice. The values of these storm surge heights are 2.61 m at Yeosu tidal station and 2.34 m at Masan tidal station. It turned out that all observed SSHs higher than 2.0 m and half of the observed SSHs higher than 1.0 m occurred in the southeastern coast of the KP. Six typhoons produced the storm surge heights of over 1.0 m around the KP. These six typhoons were named Maemi (2003), Rusa (2002), Bolaven (2012), Nari (2007), Megi (2004) and Sanba (2012). Tracks, intensity and the characteristics of each typhoon are shown in Figure 2.3 and Table 2.3. The information of the typhoons is given by the best track data of Digital Typhoon Data Base (2014).

Based on above discussion, we selected these six typhoons as the target typhoons for the detail of analysis in the southeastern coast of the KP. A series of hindcasting of storm surge for the target area by the target typhoons is conducted. Then, the reproducibility of numerical model is evaluated according to typhoon characteristics and the different terrain characteristics.

Table 2. 1 Maximum storm surge heights by typhoons estimated using the observed tidal data with one hour interval from 1979 to 2013 between May and October

No	Observation Time [yyyy mm dd]			Maximum Surge Height [m]	Name of Tidal station	Typhoon
1	2003	09	12	1.62	Tongyeong	Maemi (0314)
2	2012	08	29	1.36	Ganghwa Bridge	Bolaven (1215)
3	2000	09	16	1.32	Tongyeong	Saomai (0014)
4	2012	08	28	1.32	Youngjong Bridge	Bolaven (1215)
5	2010	09	2	1.29	Boryeong	Kompasu(1007)
6	2012	08	28	1.29	Inchoen	Bolaven (1215)
7	2003	09	12	1.29	Yeosu	Maemi (0314)
8	2012	08	28	1.25	Boryeong	Bolaven (1215)
9	2012	08	28	1.22	Ansan	Bolaven (1215)
10	2002	08	31	1.21	Yeosu	Rusa (0215)
11	2012	08	28	1.21	Jindo	Bolaven (1215)
12	2012	08	31	1.10	Goheung	Tembin (1214)
13	2000	08	31	1.01	Wido	Prapipoon (0012)
14	2000	08	31	1.00	Inchoen	Prapipoon (0012)

Table 2.2 Maximum storm surge heights by typhoons estimated using the observed tidal data with one minute interval from 1979 to 2013 between May and October

No	Observation Time [yyyy mm dd]			Maximum Surge Height [m]	Name of Tidal station	Typhoon
1	2003	9	12	2.61	Yeosu	Maemi (0314)
2	2003	9	12	2.34	Masan	Maemi (0314)
3	2002	8	31	1.83	Yeosu	Rusa (0215)
4	2012	8	28	1.61	Goheung	Bolaven (1215)
5	2012	8	28	1.48	Jindo	Bolaven (1215)
6	2012	8	28	1.33	Incheon	Bolaven (1215)
7	2012	8	28	1.30	Wando	Bolaven (1215)
8	2012	8	28	1.28	Boryung	Bolaven (1215)
9	2012	8	28	1.24	Ansan	Bolaven (1215)
10	2007	9	16	1.20	Yeosu	Nari (0711)
11	2012	8	28	1.13	Seogwipo	Bolaven (1215)
12	2004	8	19	1.13	Ulsan	Megi (0415)
13	2002	8	31	1.12	Jeju	Rusa (0215)
14	2012	8	28	1.07	Yeonggwang	Bolaven (1215)
15	2002	8	31	1.07	Seogwipo	Rusa (0215)
16	2002	8	31	1.03	Wando	Rusa (0215)
17	2012	9	17	1.02	Gadeokdo	Sanba (1216)
18	2004	8	19	1.02	Gadeokdo	Megi (0415)

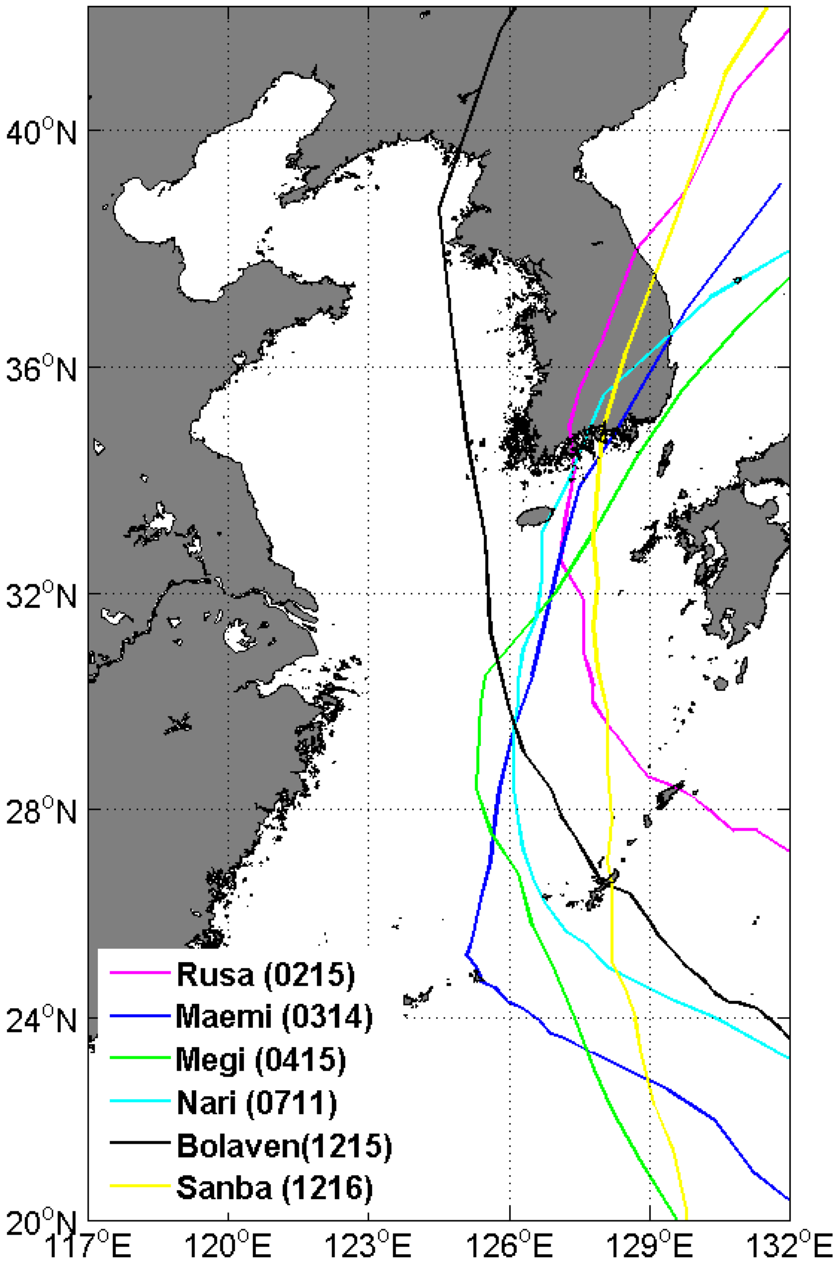

Figure 2.3 The tracks of six target typhoons which resulted in high storm surge height more than 1 m around the Korean Peninsula

Table 2.3 Characteristics of target typhoons and storm surge heights for the target typhoons

No	Typhoon Name	Observation Time [yyyy-mm-dd]	Maximum wind speed [m/s]	Minimum pressure [hPa]	Maximum Surge Height [m]	Observation Station
1	Maemi	2003-09-12	54.02	910	2.61	Yeosu
2	Rusa	2002-08-31	41.16	950	1.83	Yeosu
3	Bolaven	2012-08-28	51.44	910	1.61	Goheung
4	Nari	2007-09-16	51.44	935	1.20	Yeosu
5	Megi	2004-08-19	33.44	970	1.13	Ulsan
6	Sanba	2012-09-17	56.59	900	1.02	Gadeokdo

2.3 Numerical model description

The simulated SSHs by the target typhoons were calculated using a coupled surge, wave and tide model (SuWAT) developed by Kim *et al.* (2008). The SuWAT model is composed of a surge model based on the depth-integrated non-linear shallow water equations (NSWE), a third-generation spectral wave model (SWAN version 40.41) and a regional astronomical tide model around Japan (Matsumoto, 2000). The SuWAT model can contain an arbitrary number of nested domains to calculate the high resolution storm surge levels by the message passing interface (MPI). As the target area in this study has complex topography but gentle bathymetry gradient. Thus wave setup effects were neglected and we performed the simulations considering only the surge module to reduce the computational cost.

In the SuWAT model, there are two options to generate external force fields of wind and pressure. One is to use meteorological data computed from the Weather Research and Forecasting (WRF) model and the other is to use an empirical typhoon model embedded in the SuWAT model. Among the empirical typhoon models, there are two models for the pressure field based on Fujita's formula and Mayer's formula and three models for the wind field based on Mitsuyasu and Fujii's formula, Fujita's formula and Mayer's formula. Takayama (2002) explained the typhoon models of Fujita, Myers and Mitsuyasu-Fujii in detail. He described that the difference of the wind distribution calculated form three models is very small under the same condition resulting in similar wind distribution and wind speed. For this reason, Fujita model for pressure distribution and Mitsuyasu-Fujii for wind distribution are employed to produce the atmospheric pressure fields and the wind fields of the typhoons in the study. The parameters of the target typhoons used to generate the pressure and wind fields were obtained from the Digital Typhoon Data Base (2014), except R_{max} which is given by an empirical formula based on observed data (Yasuda *et al.*, 2010). In the following, the surge model and the typhoon model applied in this study are explained briefly. More detailed information about the SuWAT model can be found in Kim *et al.* (2008).

2.3.1 Surge model

The governing equations of the surge model in SuWAT are the depth integrated nonlinear shallow water equations (Goto and Sato, 1993)

$$\frac{\partial \eta}{\partial t}+\frac{\partial M}{\partial x}+\frac{\partial N}{\partial y}=0 \tag{2.1}$$

$$\frac{\partial M}{\partial t}+\frac{\partial}{\partial x}\left(\frac{M^2}{d}\right)+\frac{\partial}{\partial y}\left(\frac{MN}{d}\right)+gd\frac{\partial \eta}{\partial y}=fN-\frac{1}{\rho_w}d\frac{\partial P}{\partial x}+\frac{1}{\rho_w}\left(\tau_s^x-\tau_b^x+F_x\right)+A_h\left(\frac{\partial^2 M}{\partial x^2}+\frac{\partial^2 M}{\partial y^2}\right) \tag{2.2}$$

$$\frac{\partial N}{\partial t}+\frac{\partial}{\partial x}\left(\frac{NM}{d}\right)+\frac{\partial}{\partial y}\left(\frac{N^2}{d}\right)+gd\frac{\partial \eta}{\partial x}=-fM-\frac{1}{\rho_w}d\frac{\partial P}{\partial y}+\frac{1}{\rho_w}\left(\tau_s^y-\tau_b^y+F_y\right)+A_h\left(\frac{\partial^2 N}{\partial x^2}+\frac{\partial^2 N}{\partial y^2}\right) \tag{2.3}$$

where η is the sea surface elevation, M and N are the depth-integrated velocity components in the x and y directions, P is the atmospheric pressure, f is the Coriolis parameter, g is the gravitational acceleration, d is the total water depth, A_h is the horizontal eddy diffusion coefficient, ρ_w is the density of water, and F_x and F_y represent the components of wave-induced radiation stress (but they are neglected). A set of equations are discretized by using the staggered Arakawa C grid in space and the leap-frog method in time. The finite difference scheme is explicit and uses the upwind method. If the interaction between surge and wave is considered, the wave module and surge module exchange information at a regular interval about the sea surface level, current, radiation stress and sea surface drag coefficient.

The bottom stress is computed by

$$\tau_b=\rho_w g n^2\frac{\vec{Q}\left|\vec{Q}\right|}{d^{7/3}} \tag{2.4}$$

where $\vec{Q}$ is the depth-integrated velocity vector and n is the Manning coefficient: the value of n is 0.025 for all calculation regions of ocean bottom were employed in the present nested scheme.

The water surface stress is usually represented by the following form:

$$\tau_s = \rho_a C_D \overrightarrow{w_{10}} \left| \overrightarrow{w_{10}} \right| \tag{2.5}$$

in which ρ_a is the density of air, C_D is the drag coefficient and $\overrightarrow{W_{10}}$ is the wind speed measured at 10 m above the sea surface. Check fonts in the equations and related sentences.

The boundary condition was given by no flow normal to a solid boundary. The Sommerfeld explicit method for the radiation condition was applied to the open boundaries. The water surface elevation on open boundaries is given by

$$\eta = \eta_{tide} + \eta_{storm\,surge} = \eta_{tide} + \frac{\left(P_\infty - P_{ob}\right)}{g\rho_w} \tag{2.6}$$

where $P_{\text{Đ}}$ is the environmental pressure far from the typhoon, here given as 1,013 hPa; P_{ob} is the atmospheric pressure of the typhoon at the open boundary; and η_{tide} is the tidal elevation obtained from the ocean tide model. A wet-dry scheme for tidal flat ground was taken into account in the model. For the nesting scheme, open boundary values were linearly interpolated to fine from coarse grids. The nesting was one way from coarse grids to fine grids.

2.3.2 Typhoon model

As mentioned before, among the empirical typhoon models included in SuWAT, Fujita model for pressure distribution and Mitsuyasu-Fujii model for wind distribution are employed to produce the atmospheric pressure fields and the wind fields of the typhoons in the study. Accoding to Fujita (1952), the pressure field from the center of typhoon is determined by

$$p = P_\infty - \frac{\Delta p}{\sqrt{1 + \left(\frac{r}{r_0}\right)^2}} \tag{2.7}$$

where P_∞ and Δp represent the environmental pressure far from its center and the pressure gradient in space, and r and r_0 denote the radial distance at a station and the radius of the maximum wind speed from the typhoon center, respectively. Using Eq.(2.7), the gradient of the pressure, $\frac{\partial p}{\partial r}$ is obtained by

$$\frac{\partial p}{\partial r} = \frac{r \Delta p}{r_0^2} \left\{ 1 + \left(\frac{r}{r_0} \right)^2 \right\}^{-3/2} \tag{2.8}$$

The wind speed at a point far from the center of typhoon is given by

$$\frac{V_{gr}^2}{r_t} + f V_{gr} = \frac{1}{\rho_a} \frac{\partial p}{\partial r} \tag{2.9}$$

where

$$\frac{1}{r_t} = \frac{1}{r} \left(1 + \frac{V}{V_{gr}} \sin \beta \right) \tag{2.10}$$

Using Eq.(2.9) the gradient wind is obtained by

$$V_{gr} = r \left[\sqrt{\frac{f^2}{4} + \frac{r_0 \Delta p}{\rho_a r^2 r_t} \exp\left(-\frac{r_0}{r} \right)} - \frac{f}{2} \right] \tag{2.11}$$

Based on the result of measurements, it was obtained that the ratio of the wind at 10 m to the gradient wind becomes larger near the only center of the typhoon. This ratio is represented by

$$\frac{W}{V_{gr}} = G(\xi) = G(\infty) + \left\{ G(\xi_p) - G(\infty) \right\} \left(\frac{\xi}{\xi_p} \right)^{k-1} \exp\left[\left(1 - \frac{1}{k} \right) \left\{ 1 - \frac{\xi^k}{\xi_p} \right\} \right] \tag{2.12}$$

The ratio of the wind $G(\xi)$ is parameterized by Mitsuyasu-Fujii as follows:

$$K = 2.5, \xi_p = 0.5, G(\xi_p) = 1.2, G(\infty) = 2/3$$

where G(Ð) is the reduction coefficient. The wind speed at 10 m above the sea surface, which blows to the center of typhoon with 30 degrees of the gradient wind, is represented by

$$W_x = -G(\xi)V_{gr}\frac{X + \sqrt{3}Y}{2r} \tag{2.13}$$

$$W_y = -G(\xi)V_{gr}\frac{\sqrt{3}X + Y}{2r} \tag{2.14}$$

2.4 Numerical conditions

We carried out a series of storm surge simulations, one for each target typhoon. Each simulation was carried out with 48 hours spin-up prior to the calculation of the typhoon event to bring stability to the sea surface level over the entire computational domain.

Four-domain nesting was used with a 1:3 ratio of spatial grid size from coarse grid to fine grid (shown by the dashed rectangles in Figure 2.4). The outermost domain (D1) is set in the region of 20°-42°N, 117°-132°E that almost covers the formation and dissipation of typhoons approaching to the KP. The innermost domain (D4) is the region 33.5°-35.75°N, 127°-130°E which we define as the southeastern area of the KP and has a spatial resolution of 0.008333° (about 760 m). Table 2.4 shows the information for each calculation domain.

The bathymetry data in D1 were given from the General Bathymetric Chart of the Oceans (GEBCO, 2003). For the remaining nested domains, the bathymetry data were derived from the Digital 30 s Gridded Bathymetric Data of the Korea Marginal Seas dataset (Seo, 2008). The time step of storm surge computation was 300 s. The inundation was not considered in this study.

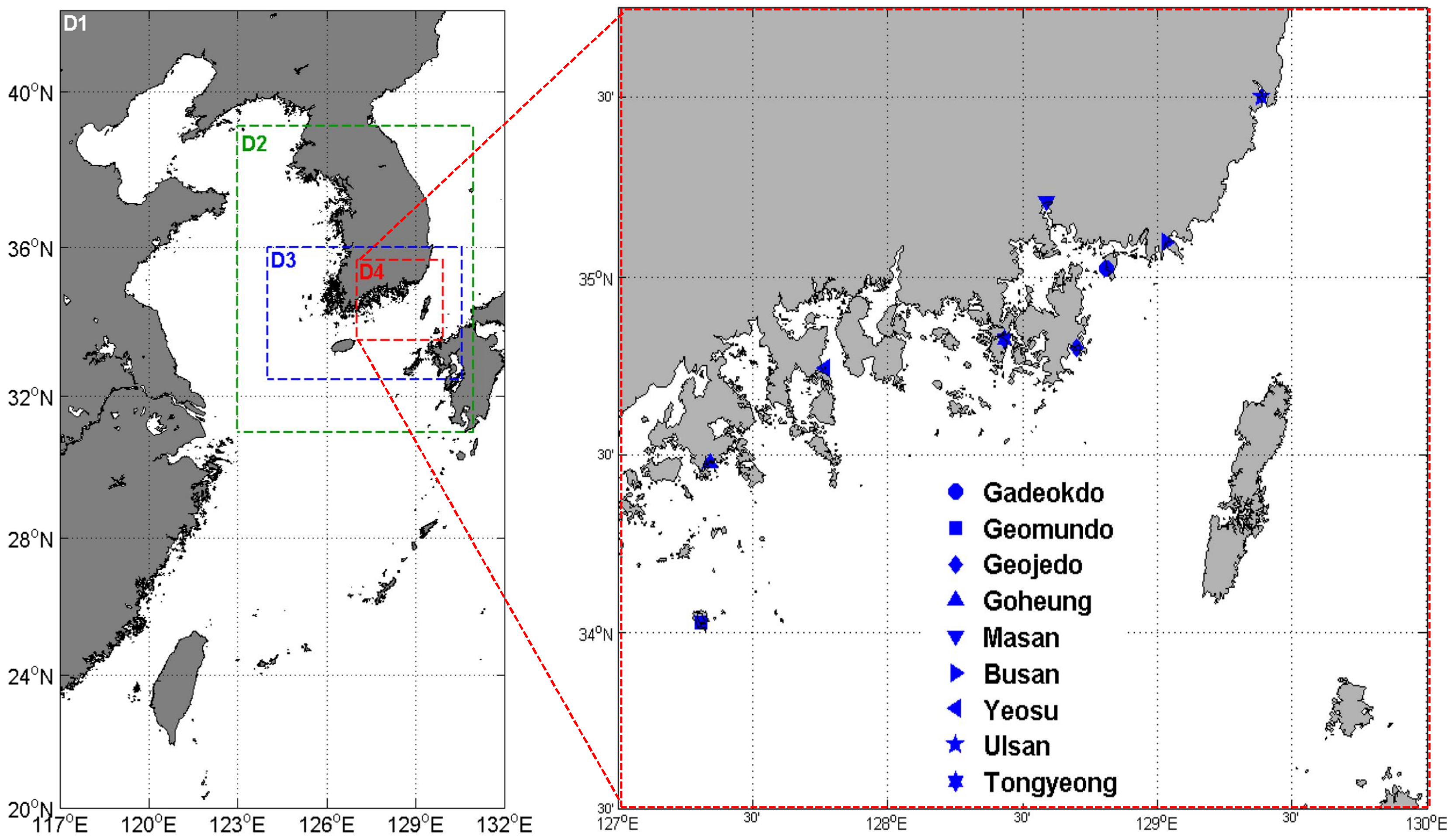

Figure 2.4 Calculation domains of storm surge hindcasting (left. abbreviated as ñD#ò, # is the number of domain) and locations of tidal observation stations in the D4 (right. marks indicate each location)

Table 2.4 Information of each calculation domain

# of Domain	The range of domain	The grid size	# of grids
1	117°E ~ 132°, 20°N ~ 42°N	φx = 9,059.8m, φy = 11,560.5 m	151 x 211
2	123°E ~ 131°, 31°N ~ 39°N	φx = 4,563.2m, φy = 5,547.1m	160 x 160
3	124°E ~ 130.5°, 32.5°N ~ 36°N	φx = 2,281.8m, φy = 2,773.2m	260 x 140
4	127°E ~ 130°, 33.5°N ~ 35.75°N	φx = 760.7m, φy = 924.5 m	360 x 270

2.5 Results and discussion

To evaluate the reproducibility of numerical model, the results of the storm surge simulations were validated against observed surge data available. Figures 2.5 to 2.10 present time series of simulated and observed SSHs at 9 tidal stations in the target area for each target typhoon, respectively. The numerical model clearly reproduces changes in storm surge pattern over time and times of occurrence of the maximum SSH at each tidal station associated with each target typhoon. On the other hand, reproducibility of values of the maximum SSH varies depending on the target area and the target typhoon. For example, the reproducibility for Masan tidal station tends to be overestimated but generally satisfactory. It is less influenced by typhoons with different properties. Difference between the simulated and the observed maximum SSHs at Masan tidal station for Typhoons Maemi, Megi and Nari is - 0.20 m, - 0.09 m and - 0.06 m, respectively. Error rate for each typhoon event is - 8 %, - 12 % and - 9 %, respectively. Meanwhile, regarding the Yeosu tidal station, the reproducibility varies depending on the typhoon. The difference of the maximum SSHs at Yeosu tidal station for Typhoons Rusa, Maemi, Megi and Nari is - 0.24 m, 0.57 m, 0.35 m and - 0.60 m, respectively. Error rate for each typhoon event is - 13 %, 22 %, 47 % and - 50 %, respectively. The difference and the error rate for the other cases are summarized in Table 2.5. For this reason, it is necessary to examine the cause of bias of the maximum SSH which is one of the important factors in the design of the disaster prevention structure installed in the coastal area.

The simulated maximum SSHs are compared with observed maximum SSHs available from nine tidal stations for all target typhoons as shown in Figure 2.11. It is seen that magnitude of bias between

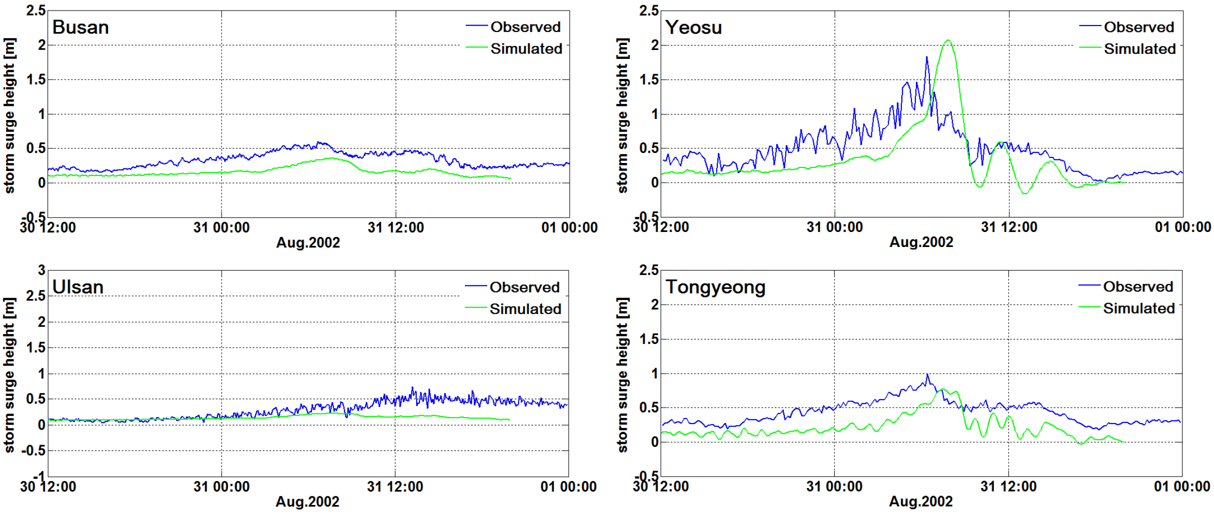

Figure 2.5 Simulated and observed maximum storm surge heights (SSHs, unit : m) at four tidal stations in the target area for Typhoon Rusa. Blue and green lines indicate observed and simulated maximum SSHs, respectively. Place names at the top left in each panel correspond to locations of each tidal station.

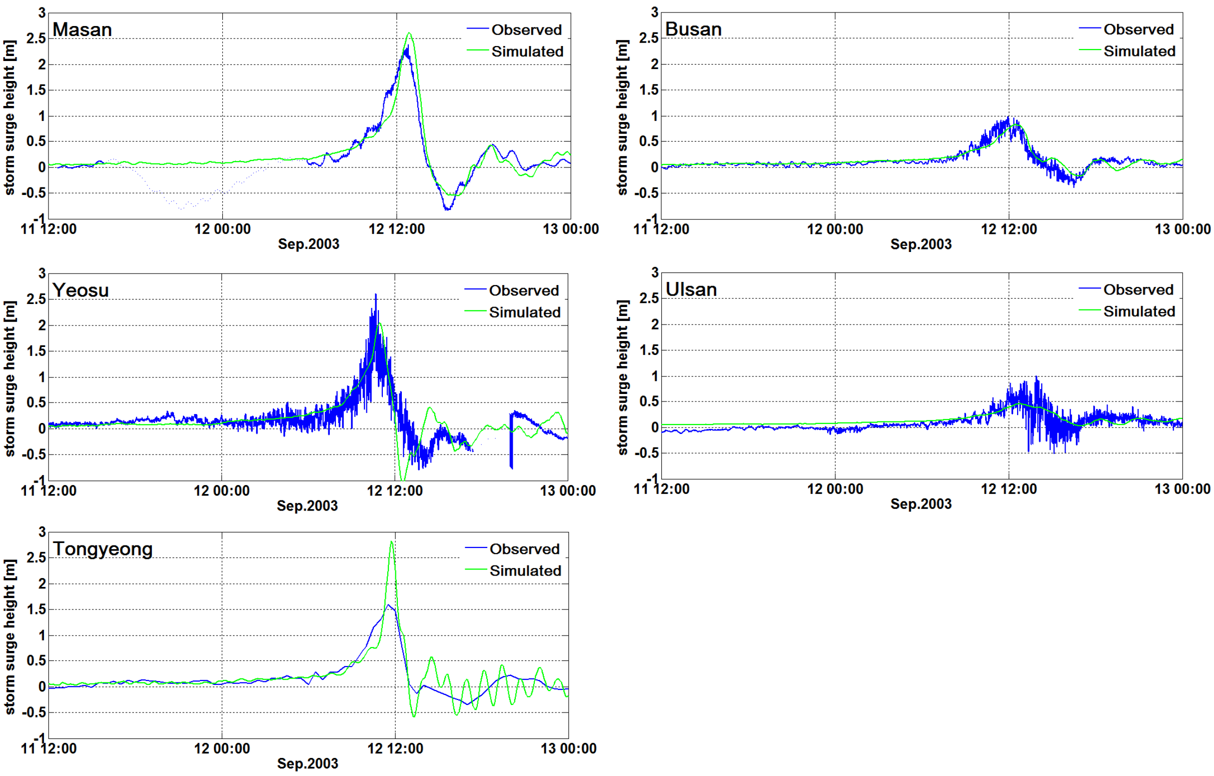

Figure 2.6 Simulated and observed maximum storm surge heights (SSHs, unit : m) at five tidal stations in the target area for Typhoon Maemi. Blue and green lines indicate observed and simulated maximum SSHs, respectively. Place names at the top left in each panel correspond to locations of each tidal station.

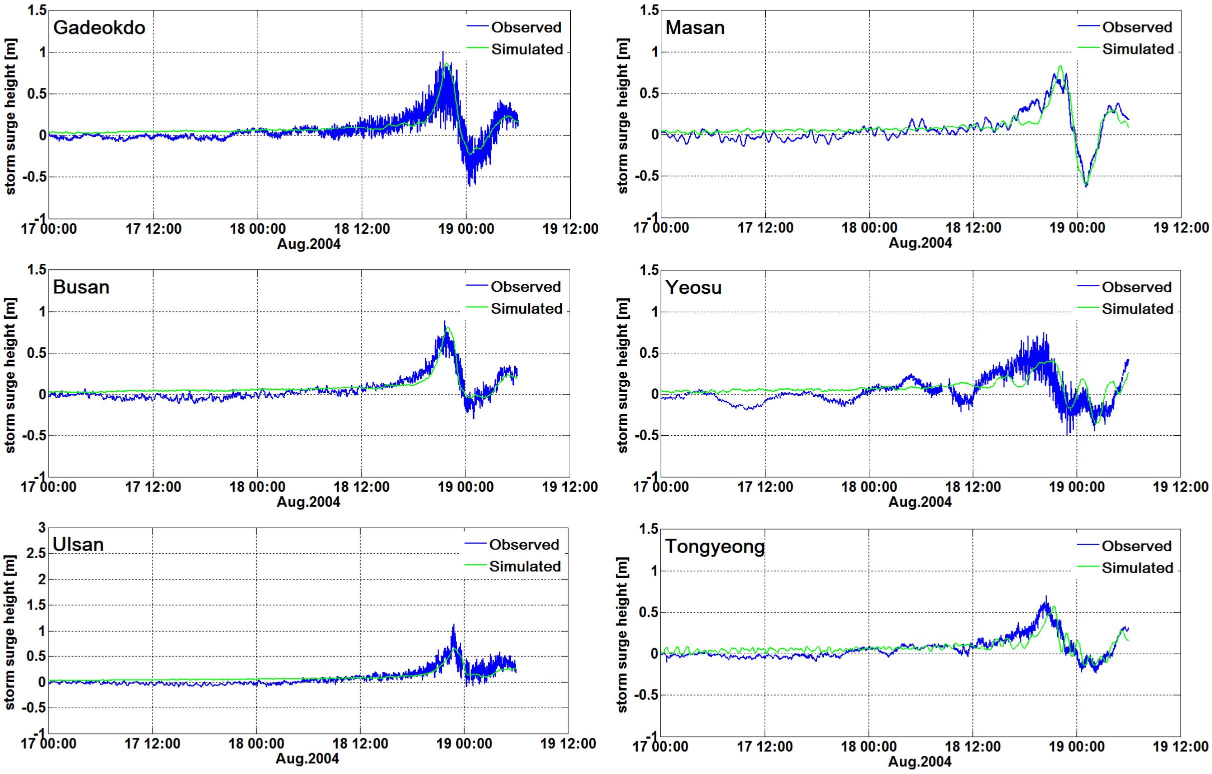

Figure 2.7 Simulated and observed maximum storm surge heights (SSHs, unit : m) at six tidal stations in the target area for Typhoon Megi. Blue and green lines indicate observed and simulated maximum SSHs, respectively. Place names at the top left in each panel correspond to locations of each tidal station.

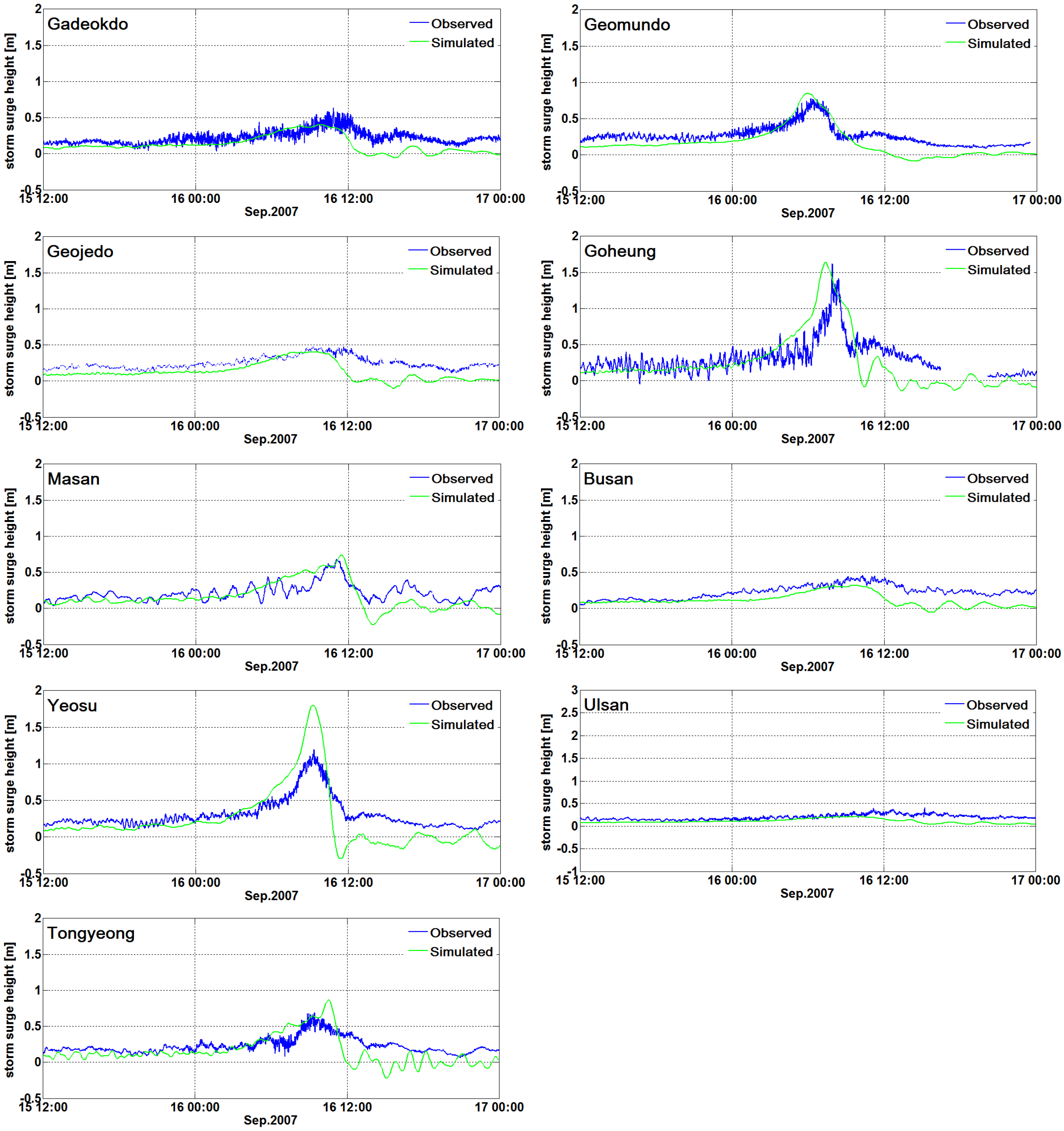

Figure 2.8 Simulated and observed maximum storm surge heights (SSHs, unit : m) at nine tidal stations in the target area for Typhoon Nari. Blue and green lines indicate observed and simulated maximum SSHs, respectively. Place names at the top left in each panel correspond to locations of each tidal station.

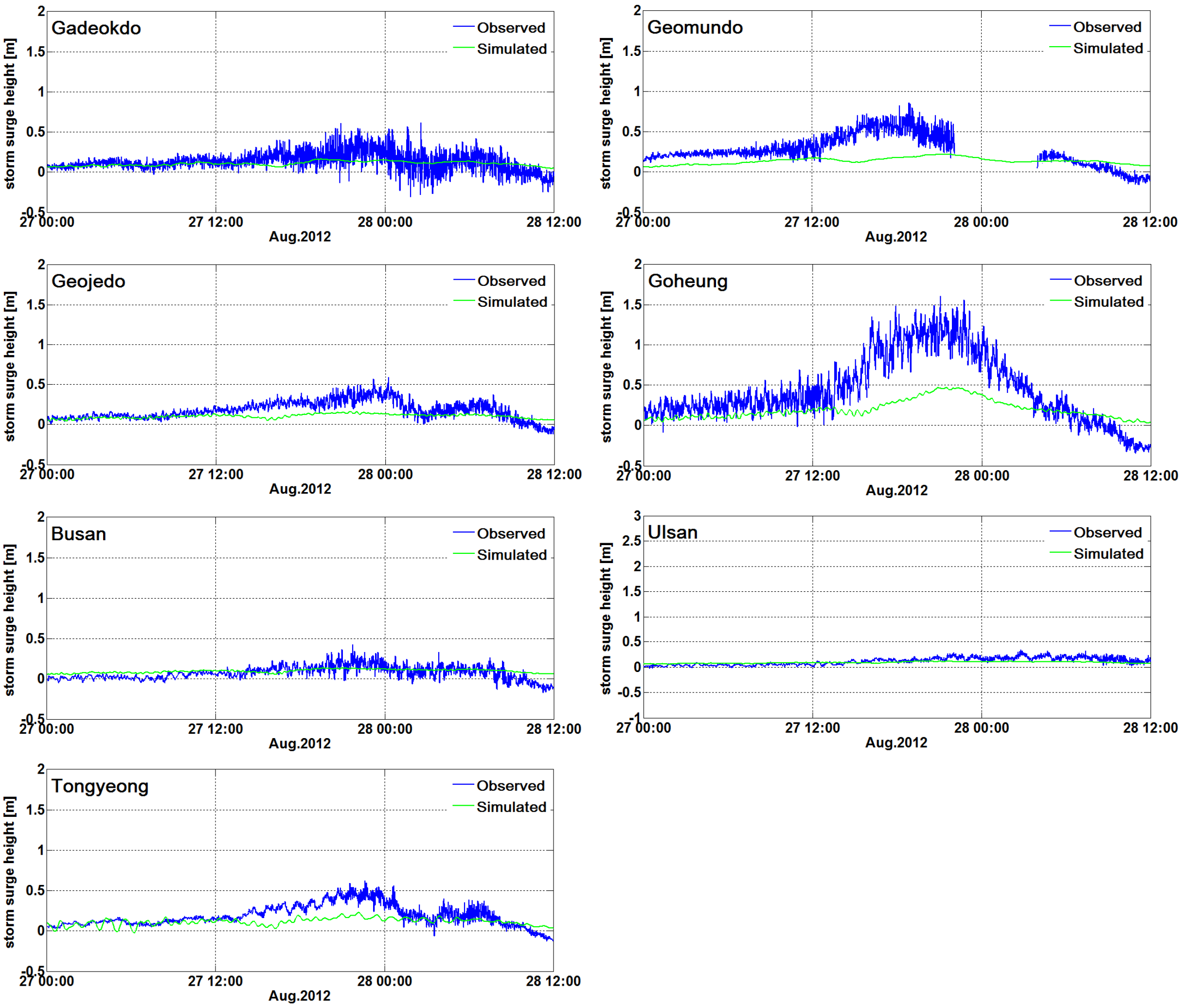

Figure 2.9 Simulated and observed maximum storm surge heights (SSHs, unit : m) at seven tidal stations in the target area for Typhoon Bolaven. Blue and green lines indicate observed and simulated maximum SSHs, respectively. Place names at the top left in each panel correspond to locations of each tidal station.

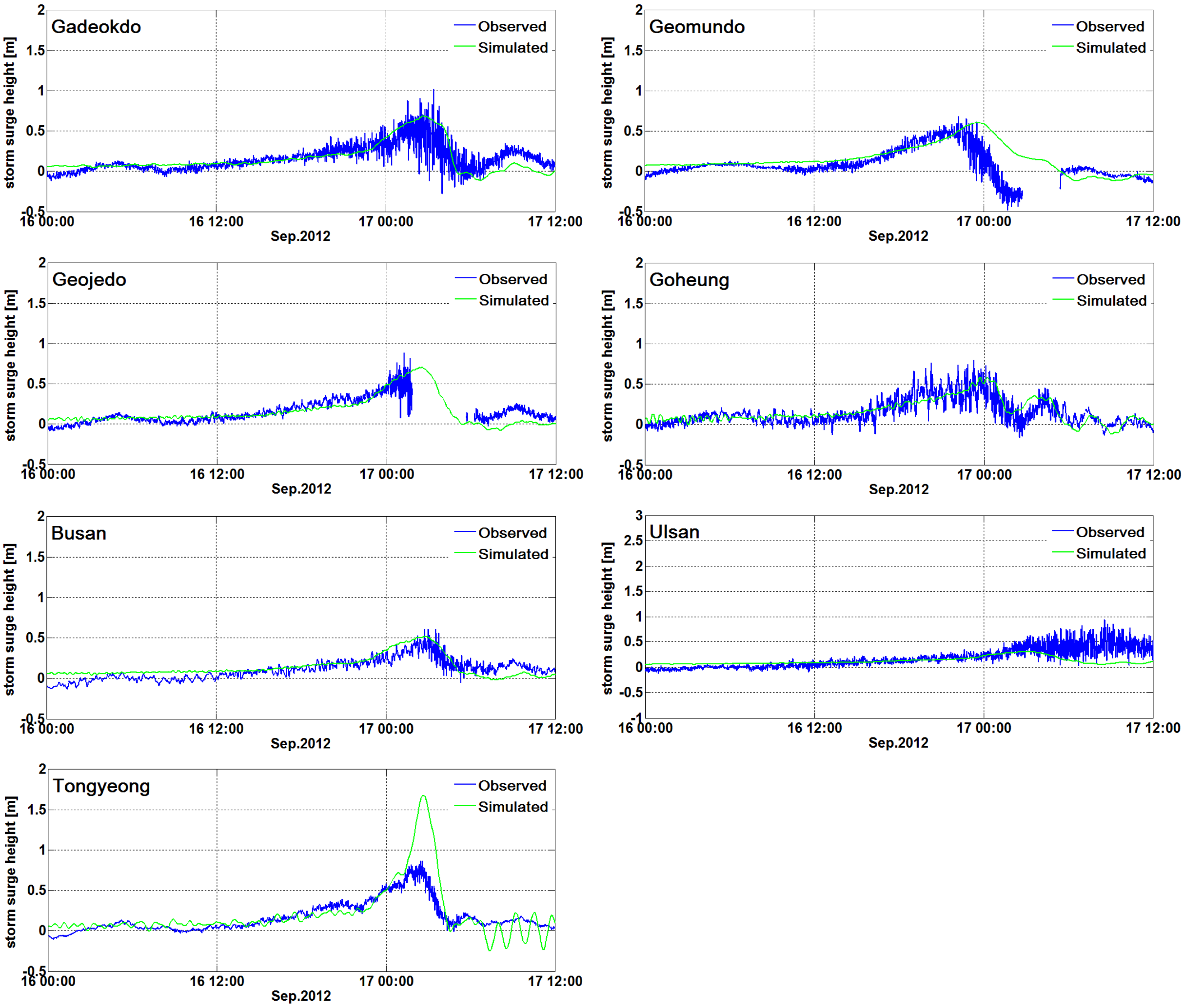

Figure 2.10 Simulated and observed maximum storm surge heights (SSHs, unit : m) at seven tidal stations in the target area for Typhoon Sanba. Blue and green lines indicate observed and simulated maximum SSHs, respectively. Place names at the top left in each panel correspond to locations of each tidal station.

Table 2.5 Absolute error (unit : m) and error rate (unit : %) between simulated and observed maximum storm surge heights at different tidal station for target typhoons

Location of tidal station \ Typhoon name	Rusa	Maemi	Megi	Nari	Bolaven	Sanba
Gadeokdo	-	-	0.15 m 15 %	0.24 m 38 %	0.45 m 73 %	0.33 m 32 %
Geomundo	-	-	-	- 0.07 m -9 %	0.65 m 76 %	0.07 m 10 %
Geojedo	-	-	-	0.06 m 13 %	0.43 m 74 %	0.18 m 20 %
Goheung	-	-	-	- 0.02 m - 1 %	1.23 m 76 %	0.21 m 26 %
Masan	-	- 0.20 m - 8 %	- 0.09 m - 12 %	- 0.06 m - 9 %	-	-
Busan	0.24 m 41 %	0.16 m 16 %	0.08 m 9 %	0.14 m 30 %	0.28 m 67 %	0.10 m 16 %
Yeosu	- 0.24 m - 13 %	0.57 m 22 %	0.35 m 47 %	- 0.60 m - 50 %	-	-
Ulsan	0.53 m 71 %	0.55 m 55 %	0.49 m 43 %	0.20 m 49 %	0.20 m 59 %	0.64 m 68 %
Tongyeong	0.23 m 23 %	- 1.23 m - 77 %	0.12 m 17 %	- 0.18 m - 26 %	0.47 m 75 %	- 0.81 m - 93 %

the simulated and the observed SSHs depends on properties of typhoons and tidal stations. Furthermore, the overestimation (underestimation) appeared to be related to values of SSH higher (lower) than 1.0 m. Figure 2.12 shows relation between the bias and other variables: distance from typhoon center and tidal station and coastline complexity of tidal station. When the distance from the center of the typhoon to the tidal station is small and the tidal station is located to the right side of the typhoon track, the SSHs tend to be overestimated (Figure 2.12 (left)). This is especially pronounced among tidal stations that have complex coastlines (The method of evaluating the coastline complexity of each station is described in Chapter 3 in detail). In contrast, when the distance between them is large, the SSHs tend to be underestimated regardless of relative position between them. It is also found that the complex coastline tend to have the large bias range (Figure 2.12 (right)).

The model performance at each tidal station was evaluated using the root mean square error (RMSE) as described by Eq. (2.15):

$$RMSE = \sqrt{\frac{\sum_{i}^{n}\left(\eta_{s,observed}^{i} - \eta_{s,calculated}^{i}\right)^{2}}{m}} \tag{2.15}$$

where m is the number of observational data in the storm surge time series at a given location.

The lowest value for RMSE appeared at Masan station with 0.13 m. The highest one appeared at Tongyeong with 0.64 m. The RMSE values tend to be larger for tidal stations located along more complex coastlines. So, it is necessary to consider topographical features to correct the bias. The RMSE for overall model performance is 0.43 m. The reason why the RMSE is large may be because we calculated the storm surge heights for each target typhoon using the same values for all physical parameters in the numerical model.

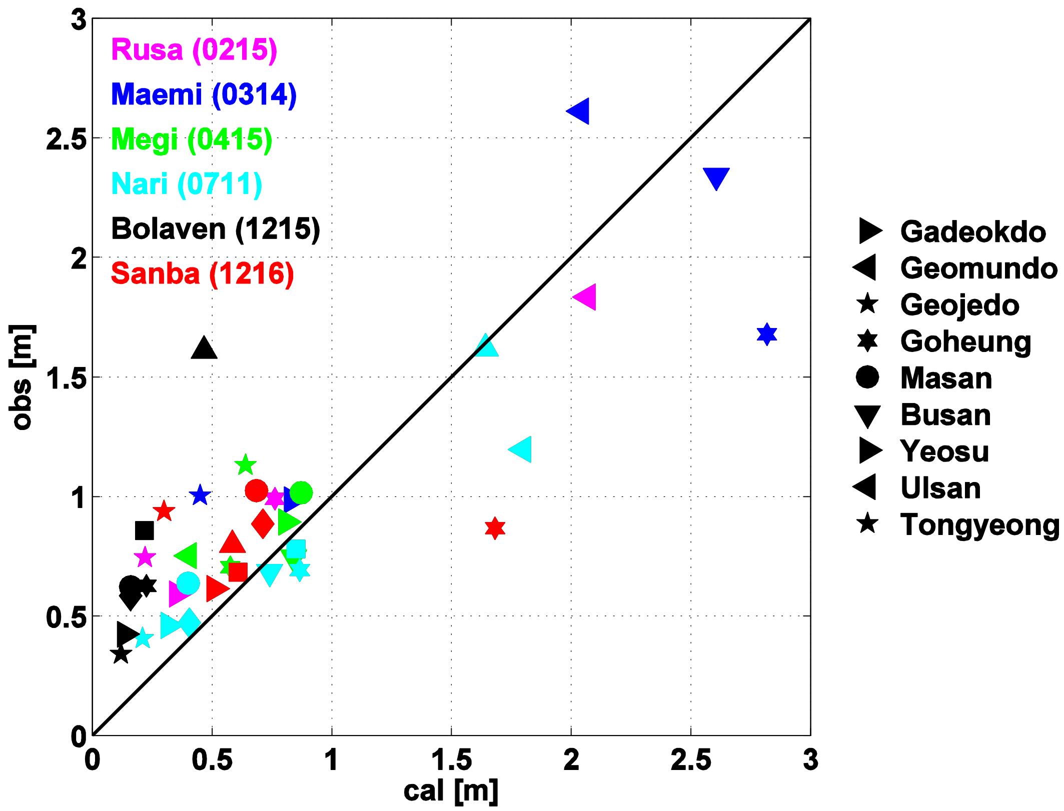

Figure 2.11 Comparison of observed and simulated storm surge heights for target typhoons at nine tidal observation stations (colors correspond to individual typhoons shown in Figure 2.3 and marks indicate location of observation)

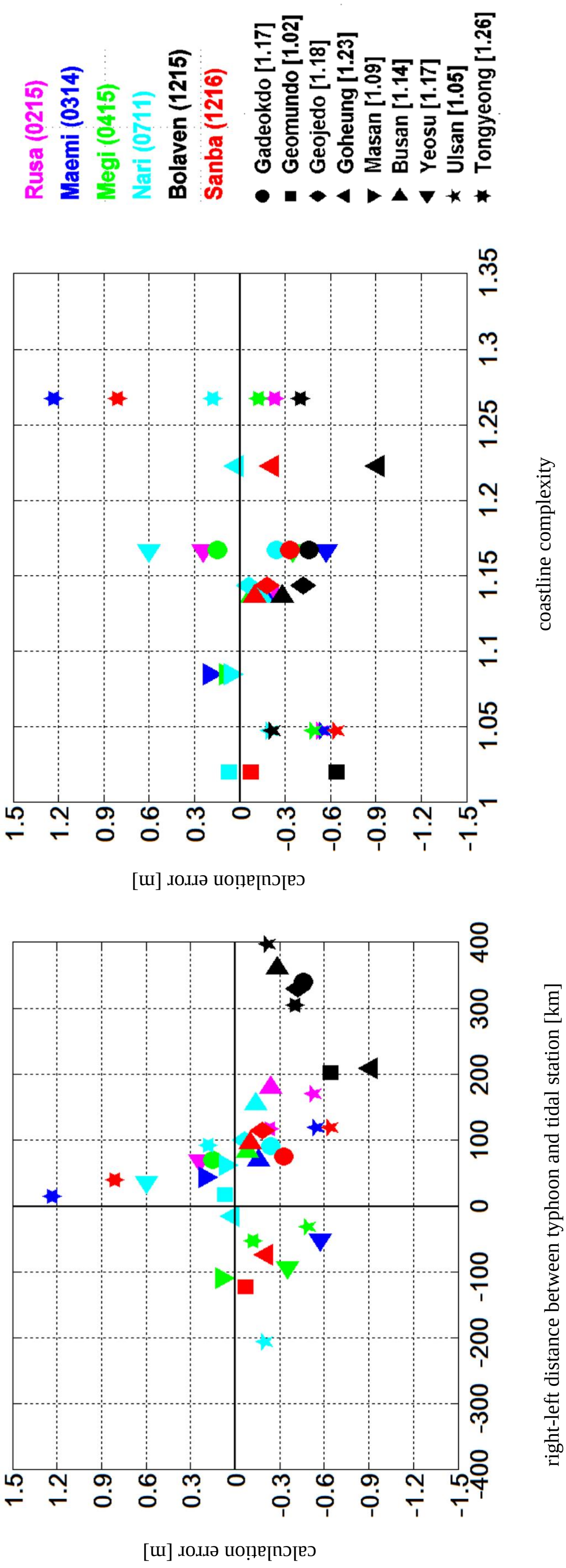

Figure 2.12 Relation between bias and other variables: (left) distance between typhoon center and target location and (right) coastline complexity

So far, many researchers have conducted validations of numerical models by hindcating historical SSHs using historical typhoon data and observed surge height data. However, the most of these studies verified the numerical models not by correcting calculation errors but by adjusting values of physical parameters to obtain SSH close to the observed value. For example, Shibutani *et al.* (2015) verified the numerical model by hindcasting SSH at Ise Bay, Japan, during the Typhoons Vera event in 1959. In their study, they adjusted the value of reduction factors for wind speed at 10 m relative to the typhoonօs movement and gradient wind speed. This parameter is used to reduce the influence of the wind velocity on the right side of the typhoon path when calculating the wind field using the parametrical wind model. Therefore, as the path of the typhoon changes even for the same region, the proper value of that parameter can vary. In addition, when estimating SSHs at multiple points by a single typhoon, the optimum value of that parameter can be different at each point. In another case, Nakajo *et al.* (2015) modified the value of the radius of maximum wind ($R_{\max}$) to confirm the reproducibility of the numerical model by hindcasting SSH that occurred in Tokyo Bay, Japan, during the Typhoon Roke event in 2011. The parameter R_{max} is an indicator of the size of a typhoon and has a different value for each typhoon. Thus, previous approaches to model validation are suited for the estimation of SSH at a particular point for a particular typhoon, but are not appropriate for the estimation of SSH at multiple points for various typhoons.

A new approach is required to evaluate numerical models that can be applied projections of possible future change in SSHs on regional scales.

2.6 Summary

The observed tidal data was analyzed to identify the storm surge-prone area where high storm surge heights occurred and the properties of typhoons that resulted in the high storm surge heights. The storm surge heights higher than 1 m were observed at 10 tidal stations in the southern coastal area and at 3 tidal stations in the western coastal area since 2000. Value of the highest storm surge height became 2.61 m which was observed at Yeosu tidal station in the southern coastal area. Six typhoons produced the storm surge heights of over 1.0 m around the Korean Peninsula. These six typhoons were named Maemi (2003, year of occurrence), Rusa (2002), Bolaven (2012), Nari (2007), Megi (2004) and Sanba (2012).

In addition, a series of hindcasting of storm surge for the southeastern coastal area by the six typhoons was conducted to evaluate the reproducibility of numerical model according to typhoon characteristics and the different terrain characteristics. The simulated maximum storm surge heights for historical events were compared with the observed maximum storm surge heights available from nine tidal stations in the southeastern area. It was found that when the distance between the center of the typhoon and the tidal station is small and the tidal station is located to the right side of the typhoon track, the storm surge heights tend to be overestimated. This is especially pronounced among tidal stations that have complex coastlines (The method of evaluating the coastline complexity of each station is described in Chapter 3 in detail). On the contrary, when the distance between them is large, the storm surge heights tend to be underestimated regardless of relative position between them. It is also found that the complex coastline tend to have the large range of bias between the simulated and the observed storm surge heights. The model performance at each tidal station was evaluated using the root mean square error (RMSE). The lowest value for RMSE appeared at Masan station with 0.13 m. The highest one appeared at Tongyeong with 0.64 m. The RMSE values tend to be larger for tidal stations located along more complex coastlines. So, it is necessary to consider topographical features to correct the bias.

The RMSE for overall model performance is 0.43 m. The reason why the RMSE is large may be because we calculated the storm surge heights for each target typhoon using the same values for all physical parameters in the numerical model.

Chapter 3.
Bias Correction of Simulated Storm Surge Height considering Coastline Complexity

In Chapter 2, it was found that bias between simulated and observed storm surge heights (hereafter, SSHs) is related to topographical features of the area of interest. This chapter proposes a formula for the bias correction of the calculated SSHs by using a geographic parameter representing the coastline complexity factor to improve the reproducibility of the numerical model against observed data. First, the degree of coastline complexity along the coast is discussed using the concept of fractal dimension. Second, a relation between the model bias and a coastline complexity factor is discussed and then the bias correction method is proposed as a function of coastline complexity. Third, the verification of bias correction method is carried out. Finally the proposed bias correction is applied to the projection of potential maximum SSHs considered TC intensity change.

3.1 Estimation of coastline complexity around each tidal station

The outline of a fractal dimension is introduced first. The fractal dimension is a way of defining the geometric irregularity of an object with non-integer dimensions, which is different from Euclidean dimension. The fractal dimension was introduced by Mandelbrot (1967) and has been used as a measure of the complexity of objects for many fields: geology (e.g., Okubo, 1987; Choi and Chang, 1999), river engineering (e.g., Hjelmfelt,1988; Tarboton *et al.*, 1988; Rosso *et al.*, 1991; Marani *et al.*, 1991; Cha and Kwon, 2001), and coastal engineering (e.g., Philip, 1994; Carr and Benzer, 1991; Zhu *et al.*, 2004). In the field of coastal engineering, many researchers have applied the fractal dimension to assess complexities of coastlines in different countries: Britain (e.g., Philip, 1994), USA (e.g., Carr and Benzer, 1991) and China (e.g., Zhu *et al.*, 2004).

Two methods are commonly used to estimate the fractal dimension: divider method (Mandelbrot, 1982; Klinkenberg, 1992, 1994) and box-counting method (Grassberger, 1983). The divider method is the original method of fractal theory and suitable to use on vector linear features represented by coordinate pairs. On the other hand, the box-counting method is more widely used method because of its convenience for applications; it can be applied to discontinuous curves and image files. In this study, the box-counting method was adopted to calculate the fractal dimension of coastlines. As base data of coastline profiles, images of coastline maps based on the version 2.3.2 of the Global Self-consistent, Hierarchical, High-resolution Geography Database (GSHHG) by Wessel and Smith (1996) are used for analysis.

The box-counting is a way of determining the fractal dimension by breaking an object into smaller components, typically box-shaped, and counting how many boxes are required to cover the object at each smaller scale. Suppose that r is a length of one side of a box and N(r) is the number of boxes with the length, r, needed to cover the object. The fractal dimension is defined as:

$$F_D = \lim_{r \to 0} \frac{\log N(r)}{\log\left(\frac{1}{r}\right)} \tag{3.16}$$

The flow of calculating the fractal dimension of coastline using the box-counting method from an image file is as follows (fractalfoundation, 2016; refer to Figure 3.1):

1. To cover the coastline in the image file with grids with a size of r and then count the number of the grids, (N(r)) covering the coastline (Figure 3.1 (a)).
2. To do the repeat same procedure as reducing the size of the grid repeatedly (Figures 3.1 (b)-(c)).

3. To plot the value of log $N(r)$ on the Y-axis against the value of log $(1/r)$ on the X-axis.

4. To calculate of the slope of the line which is the fractal dimension of coastline (Figure 3.1 (d)).

Range of the fractal dimension is between 1 and 2 for analysis of complexity of coastline.

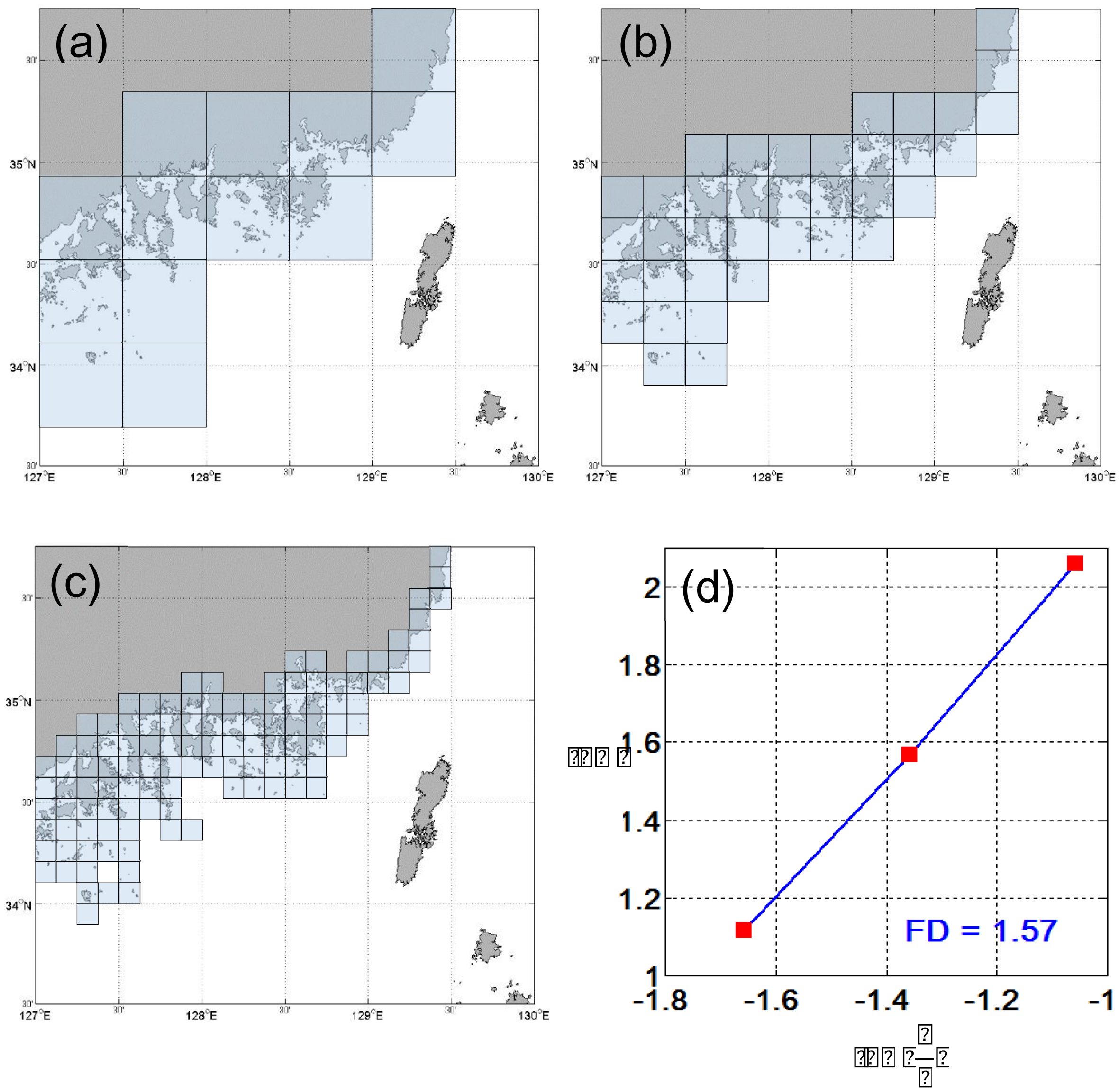

Figure 3.1 Flow of calculating fractal dimension of a coastline using a box-counting method from an image file: (a) cover the coastline with grids with a size of r_a and then count the number of the grids, (N(r_a)) covering the coastline), (b) and (c) repeat same procedures as (a) by reducing the size of grid repeatedly. It means $r_c < r_b < r_a$. and (d) plot the value of log N(r) on the Y-axis against the value of log (1/r) on the X-axix and calculate of the slope of the line which is the fractal dimension of coastline

To evaluate the relation between the bias and the coastline complexity quantitatively, the fractal dimensions (F_D) of the coastline around each tidal station are calculated based on above described box counting method. Figure 3.2 shows the locations of the nine tidal stations in the target domain as well as the coastline within a radius of 12.5 km of each tidal station. Figure 3.3 presents the F_D at the nine tidal stations. It ranges from 1.020 to 1.268. The F_D increase in order of Geomundo, Ulsan, Masan, Busan, Geojedo, Yeosu, Gadeokdo, Goheung and Tongyoung tidal stations; this order is the similar to the eye-sighted order. It can be seen that the F_D of the tidal stations with a number of small islands become large. Since larger values of F_D signify more complex coastlines, among the nine tidal stations the Tongyoung stations has the highest coastline complexity.

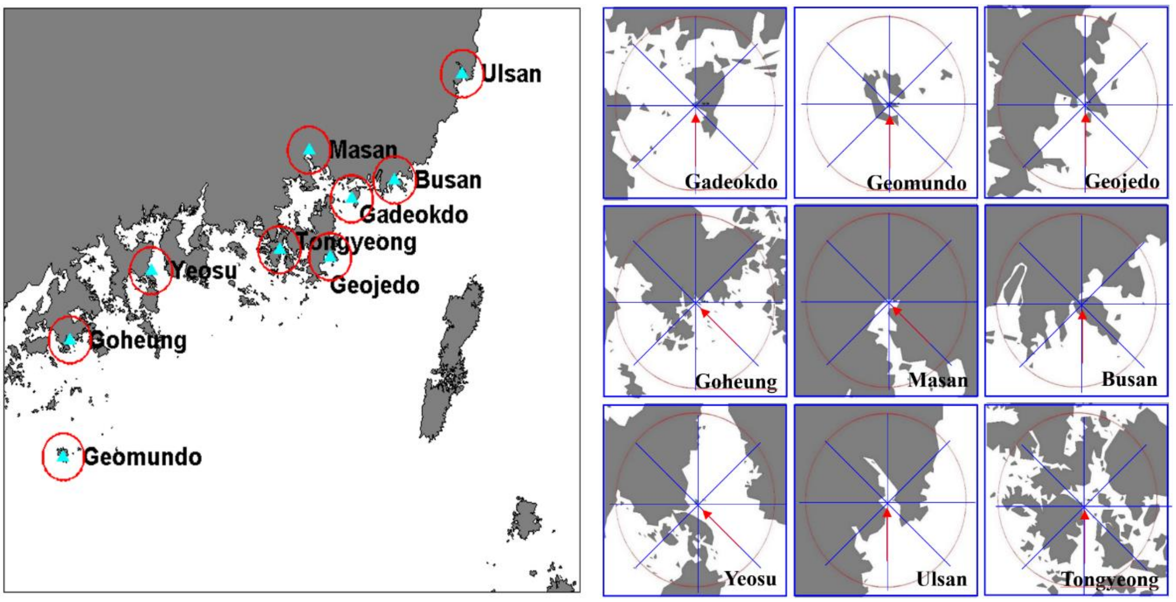

Figure 3.2 (Left) locations of tidal stations in the target domain and (right) coastlines within a radius of 12.5 km of each tidal station whose names are written on the bottom right corner in each panel. The red arrow on each panel means predominant wind directions that would cause the highest SSH at location.

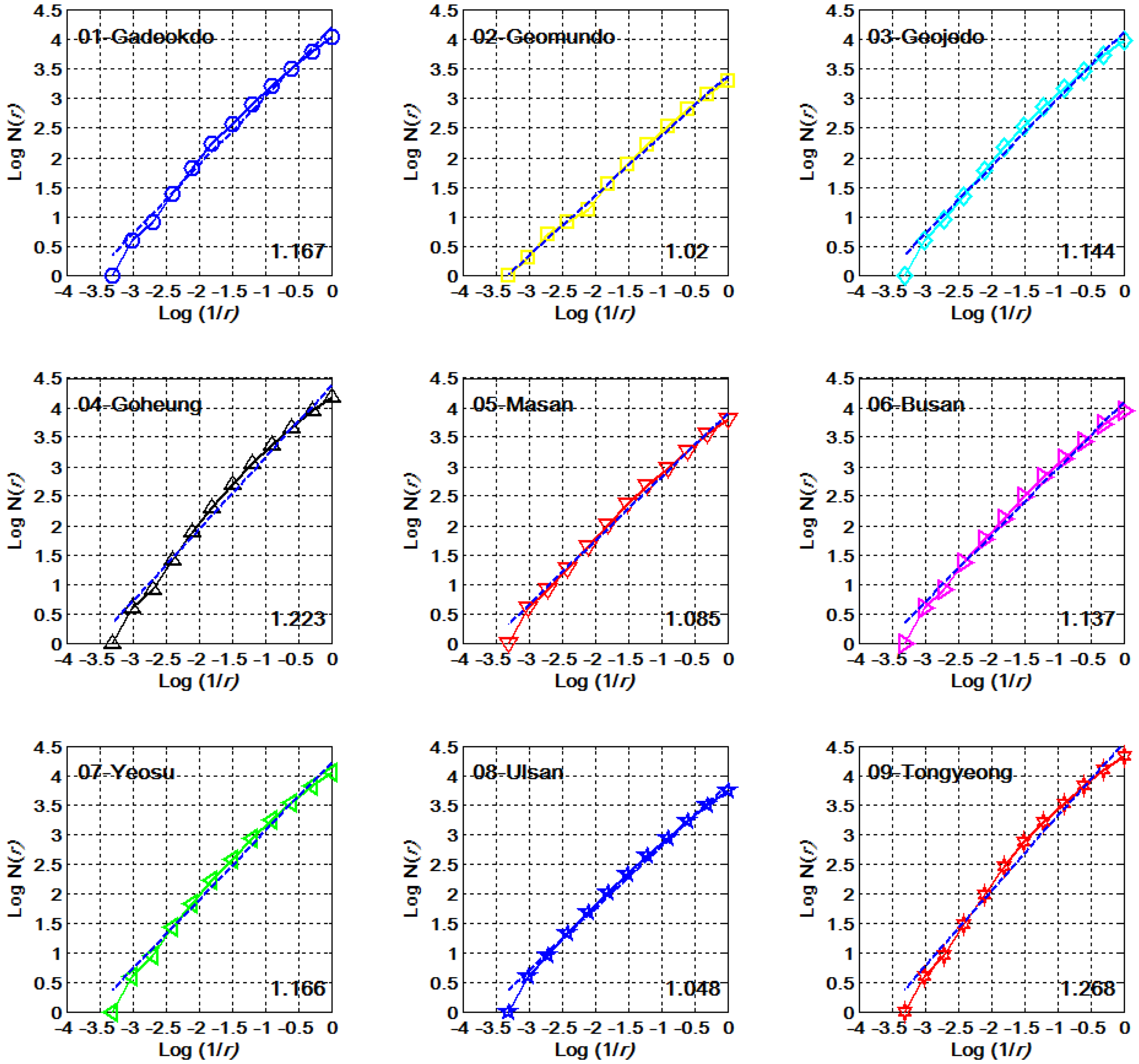

Figure 3.3 Fractal dimension for the each tidal station. In each panel, place name at the top left and value at the bottom right correspond to the location and the fractal dimension of each tidal station, respectively. *r* in the X-axis is a size of grids covering the coastline and N(*r*) in the Y-axis is the number of the grids with the size *r*.

3.2 Bias correction of storm surge heights considering coastline complexity

In this section, the relational expression between bias and coastline complexity factors is discussed and then bias is parametrized as a function of the degree of coastline complexity by deriving regression equations between them. The bias is defined the error of calculated SSHs to the observed ones hereafter.

3.2.1 Drawing a relational expression between bias and a coastline complexity factor

The calculated SSH (abbreviated as ζ_{cal}) contains an error $\Delta\zeta$ against the observed SSH (presented as ζ_{obs}) at tidal station. The revised calculated SSH, that is, ζ_{cal}^{rev} s given by

$$\zeta_{cal}^{rev} = \zeta_{cal} + \Delta\zeta = \zeta_{obs}. \quad (3.2)$$

To express $\Delta\zeta$ as an equation, we introduce an empirical model for SSHs. The Japan Meteorological Agency used the following simple empirical formula for predicting storm surge height before a numerical model was developed (Unoki and Isozaki, 1966):

$$\zeta_{predict} = a \times \Delta p + b \times U^2 \cos\theta. \quad (3.3)$$

where $\zeta_{predict}$ [m] is the predicted SSH from the empirical model, Δp [hPa] is the difference between environmental atmospheric pressure (1,010 hPa) and lowest atmospheric pressure at the typhoon location, U [m/s] is the maximum wind speed, θ [°] is the angle between predominant wind direction that would cause the highest SSH at location and the wind direction at the time of maximum SSH during a typhoon, and a [m/hPa] and b [s^2/m] are the tuning coefficients determined for this location based on historical observation data. Generally, regardless of location, 0.0099 is used as the value of the coefficient a, but the coefficient b strongly depends on regional features such as characteristics of the coastline, the shape of a bay and local bathymetry. That is, the coefficient b in the empirical formula is an inherent factor reflecting the characteristic of terrain and can be expressed as follows:

$$b = \frac{\{\zeta_{predict} - a \times \Delta p\}}{U^2 \cos\theta} = \frac{\{\zeta_{predict} - 0.0099 \times (1010 - p_{mn})\}}{U^2 \cos\theta} = \frac{\{\zeta_{predict} - \zeta_{pressure}\}}{\zeta_{wind}} \tag{3.4}$$

where $\zeta_{pressure}$ [m] and ζ_{wind} [m] are sea level rise by atmospheric pressure drop and by wind, respectively. For regional correction of the empirical model, the geographical parameter b should be replaced with (b+φb).

$$\zeta_{predict}^{rev} = a \times \Delta p + (b + \Delta b) \times U^2 \cos\theta = \zeta_{predict} + \Delta b \times U^2 \cos\theta \tag{3.5}$$

We assume $\zeta_{predict}$ is comparable to ζ_{cal}:

$$\zeta_{predict} \approx \zeta_{cal} \tag{3.6}$$

If we can apply the above method to the numerical result, we can express the calculation error (bias) as following equation

$$\zeta_{cal}^{rev} \approx \zeta_{cal} + \Delta b \times U^2 \cos\theta \tag{3.7}$$

Here, we call φb a terrain correction factor and assume φb is the difference between b_{obs} and b_{cal}, calculated by substituting the ζ_{obs} and ζ_{cal} to $\zeta_{predict}$ in Equation. (3.4), respectively:

$$\Delta b = b_{obs} - b_{cal} = \frac{\zeta_{obs} - \zeta_{pressure}}{\zeta_{wind}} - \frac{\zeta_{cal} - \zeta_{pressure}}{\zeta_{wind}} \tag{3.8}$$

However, Equation (3.8) cannot be directly used to project the future SSH, because it needs the observed SSH to estimate φb. The numerical error can be caused by atmospheric forcing, numerical model itself and ill posed bathymetry. Here, we roughly assumed that the bias error mainly occurs due to limitation of terrain reproducibility based on spatial resolution of bathymetry excluding two other factors. Based on the assumptions, we parameterized φb as a function of the coastline complexity factor F_D,

$$\zeta_{cal}^{rev} = \zeta_{cal} + f(F_D) \times U^2 \cos\theta \tag{3.9}$$

where $f(F_D)$ [s^2/m] is a tuning function of the F_D which is a dimensionless parameter.

3.2.2 Suggestion of bias correction formulas considering the coastline complexity factor

For bias correction considering the coastline complexity based on Equation (3.9), a relational expression between F_D and φb of a coastline of interest should be obtained. Here, F_D of nine tidal stations which was calculated in Section 3.1 and φb of nine tidal stations for six typhoons which was simulated in Section 2.5 were used to obtain the relational expression. We derived regression formulas between F_D and φb of nine tidal stations through regression analysis using φb for four typhoons of six typhoons. Then the regression formulas were validated using the results of calculated SSHs for remaining two typhoon events. First, the regression formulas between F_D and φb were derived using φb for four Typhoons Meami, Megi, Nari, and Sanba. In Figure 2.5, the number of observation data above 1.0 m is very limited. In that range, the relative error range tends to also be large. These four typhoons were chosen to estimate the regression equation because they have high SSHs and large errors, and the resulting bias correction performs well. A linear regression equation (Equation (3.10), abbreviated as LRE) and a cubic regression equation (Equation (3.11), abbreviated as CRE) were drawn as follow:

$$\Delta b = 10^{-3} \times \begin{cases} -1.05 \times F_D + 1.51 \left(\zeta_{cal} < 1\right) \\ -0.56 \times F_D - 0.32 \left(\zeta_{cal} \geq 1\right) \end{cases} \tag{3.10}$$

$$\Delta b = \begin{cases} -0.1010 \times \left(F_D\right)^3 + 0.3386 \times \left(F_D\right)^2 - 0.3782 \times F_D + 0.1410 \left(\zeta_{cal} < 1\right) \\ -0.5743 \times \left(F_D\right)^3 + 1.9545 \times \left(F_D\right)^2 - 2.2093 \times F_D + 0.8291 \left(\zeta_{cal} \geq 1\right) \end{cases} \tag{3.11}$$

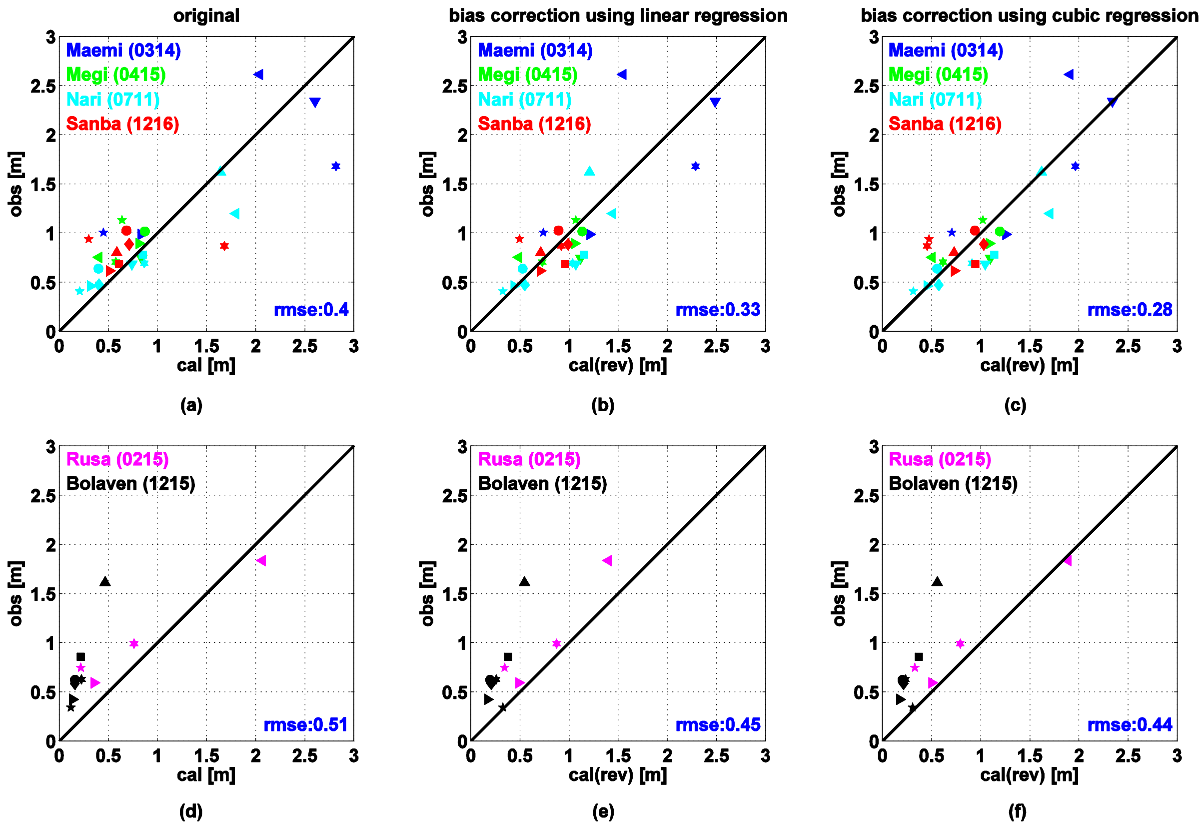

Figure 3.4 Application of bias correction based on coastline complexity parameters (top: application to four typhoons used in calibration, bottom: validation to two remaining typhoons, first column indicates no bias correction, second column indicates linear bias correction and third column indicate cubic bias correction)

In this subsection, the cosθ term in Equation (3.7) and Equation (3.9) is assumed to be one because we are concerned only the maximum wind-induced surge (i.e. where wind direction is parallel to bay direction). By conducting the bias correction based on LRE and CRE, the RMSE of the original results apparently decreases from 0.40 m to 0.33 m and to 0.28 m, respectively (Figures 3.4 (a)-(c)). The bias correction by LRE and CRE improves the modelôs performance by 18 % and 30 % in comparison without bias correction, respectively.

Next, these regression formulas were validated for Rusa and Bolaven events which are excluded for estimation of bias correction coefficients. The RMSE of results without bias correction was reduced from 0.51 m to 0.45 m (11 %) and 0.44 m (14 %) by applying the LRE and CRE for bias correction, respectively (Figures 3.4 (d)-(f)). However, the influence of the higher order regression equations on model performance is not large. For tidal stations except Yeosu the RMSE of results modified by LRE (CRE) decreased by -0.04 m to -0.16 m (by -0.01 m to -0.18 m) and the amount of decrease tended to be larger at tidal stations with simple coastlines. At Yeosu station, the RMSE value was increased (decreased) by 0.20 m (-0.18 m) when LRE (CRE) was applied for bias correction.

In general, the RMSE of results with bias correction was reduced from 0.43 m to 0.37 m (14 %) and 0.33 m (23 %) by applying the LRE and CRE for bias correction, respectively. The CRE is more effective than LRE. It is thought that CRE reproduces the relationship between F_D and φb better than LRE. It can be seen that the bias correction method considering the coastline complexity can improve model's accuracy.

To confirm the importance of considering terrain complexity for bias correction, we compared results with bias correction for different bias correction methods: (1) a proposed method using cubic regression equation, (2) conventional methods using the average bias difference and (3) the average bias ratio between observed and simulated SSHs. Figure 3.5 shows bias correction effects according each method. The RMSE of results using methods (1) and (2) is 0.33 m and 0.32 m, respectively (refer to Figures 3.5 (b) and (c)). The small surge magnitude mainly occurred due to pressure induced surge, therefore, the bias is rather linear. Both bias correction methods, the proposed method and the conventional method using the average bias difference, can give reasonable improvement for the small surge region. The RMSE for the small surge region is 0.28 m and 0.23 m, respectively. However, the significant surges with higher than 1 m mainly occurred due to wind induced surges. In these cases, the relational position between typhoon track and locations of interest, terrain-specific characteristics such as coastline complexity, the angle of wind to target points and bathymetric features result in different characteristics of peak surge as shown in Figures 2.3 and 3.4 in the manuscript. The RMSE for the large surge regions is 0.43 m and 0.49 m, respectively. Additionally, the RMSE of result using method (3) is 0.48 (refer to Figure 3.5(d)). This method is not effective for bias correction because it is bigger than one without bias correction (refer to Figure 3.5(a)). Our proposed bias correction method gives smaller RMSE value in the large surge region which causes storm surge disaster than the two conventional methods. It was clear that considering terrain complexity is important for bias correction.

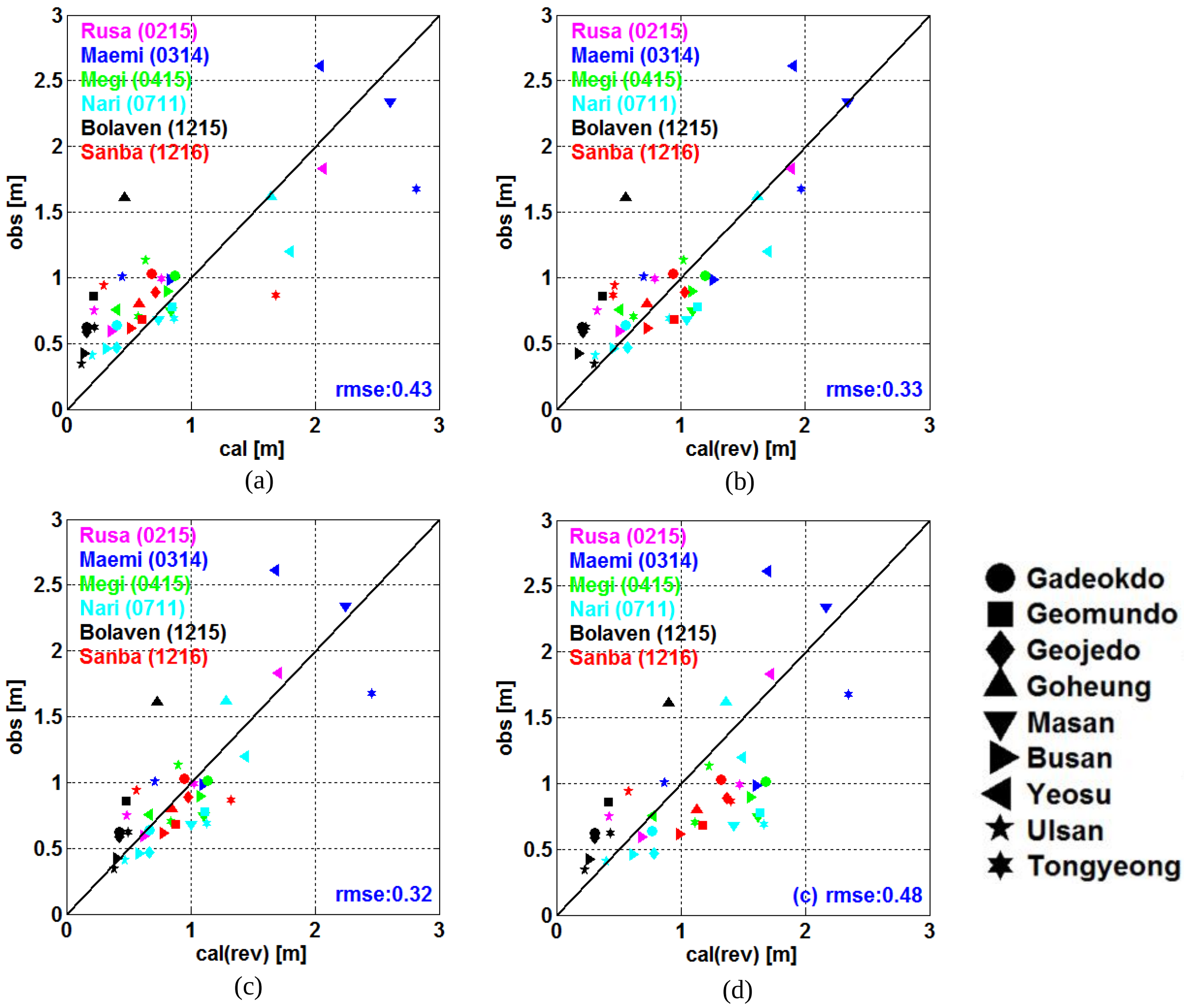

Figure 3.5 Comparisons of bias correction results for different bias correction methods: (a) without bias correction, with bias correction using (b) proposed method based on a cubic regression equation in Equation (3.11), (c) a conventional method using average difference of bias and (d) a conventional method using average ratio of bias

3.2.3 Evaluation of uncertainty of bias correction considering coastline complexity

In the previous sections, the bias correction equation (Equation 3.9) were derived, assuming the bias mainly results from the limitation of terrain reproducibility based on resolution of bathymetry. Then, the relational expressions between F_D and φb was obtained using simulated SSHs based on a bathymetry data with 760 m of horizontal resolution, regarding cosθ in Equations (3.7) and (3.9) as one. Here, application scope of the relational expressions were examined by applying the relational expressions to simulated SSHs which were calculated using bathymetry data with different resolutions: 2,280 m, 760 m and 250 m. Figure 3.6 presents the application results. The degree of bias correction effect according to the different bathymetry resolutions were evaluated by comparing the RMSE values of the respective calculation results. Results of a case with 2,280 m of horizontal resolution get better. RMSE of the results without bias correction decrease from 0.57 m to 0.52 m (9 %) and 0.53 m (7 %) by applying bias correction using the LRE and CRE, respectively (see figures in the first row of Figure 3.6). However, the influence of the higher order regression equations on bias correction effect is not large. For a case with 250 m of horizontal resolution, the RMSE without bias correction was reduced from 0.46 m to 0.40 m (13 %) and 0.39 m (15 %) by applying the LRE and CRE for bias correction, respectively (refer to figures in the third row of Figure 3.6). It is confirmed that results of all cases with different bathymetry resolutions are improved through the bias correction using the suggested relational expressions. In consideration of the computational cost, it is effective to perform the numerical simulations using bathymetry resolution with 760 m.

In additional, bias correction effect was evaluated according to whether or not a true value at each tidal station was applied to the cosθ term in Equation (3.7) and Equation (3.9). In the previous subsection, the cosθ was assumed to be one because the maximum wind-induced surge was only concerned (i.e. where wind direction is parallel to bay direction). As mentioned earlier, θ [°] is the angle between predominant wind direction that would cause the highest SSH at location and the wind direction at the time of maximum wind speed during a typhoon. In fact, the true value of the cosθ at each tidal station has a different value depending on a typhoon of interest. Here, bias correction was re-performed using true value of the cosθ by considering the relationship between the predominant wind direction at each tidal station which is marked with a red arrow in Figure 3.2 (left) and the wind direction during each typhoon. The linear regression equation (Equation (3.12), abbreviated as LRE_{true}) and the cubic regression equation (Equation (3.13), abbreviated as CRE_{true}) were re-drawn as follow:

$$\Delta b = 10^{-3} \times \begin{cases} -0.97 \times F_D + 1.59 \left(\zeta_{cal} < 1\right) \\ -1.52 \times F_D - 1.41 \left(\zeta_{cal} \geq 1\right) \end{cases} \tag{3.12}$$

$$\Delta b = \begin{cases} -0.0228 \times \left(F_D\right)^3 + 0.0543 \times \left(F_D\right)^2 - 0.0358 \times F_D + 0.0046 \ \left(\zeta_{cal} < 1\right) \\ -0.7705 \times \left(F_D\right)^3 + 2.6332 \times \left(F_D\right)^2 - 2.9908 \times F_D + 1.1287 \left(\zeta_{cal} \geq 1\right) \end{cases} \tag{3.13}$$

Figure 3.7 presents results which were corrected by applying the LRE_{true} and CRE_{true} using the true value of the cosθ depending on the bathymetry data with different resolutions: 2,280 m, 760 m and 250 m. RMSE of the results with the bathymetry data of 760 m resolution was reduced from 0.43 m to 0.37 m (14 %) and 0.34 m (21 %), respectively. These values are similar to those obtained by assuming cosθ to be one; RMSE of results after bias correction by applying the LRE and CRE was 0.37 m (14 %) and 0.33 m (23 %), respectively. Similar results were obtained for other bathymetry resolutions. The reason why there is no difference between applying the true value and assuming the maximum value of the cosθ is presumed to be that the wind direction during the typhoons used to derive the regression formulas for bias correction is parallel to the predominant wind direction at each tidal station. In the future, for convenience, the cosθ assumed to be one and LRE (CRE) are used for bias correction.

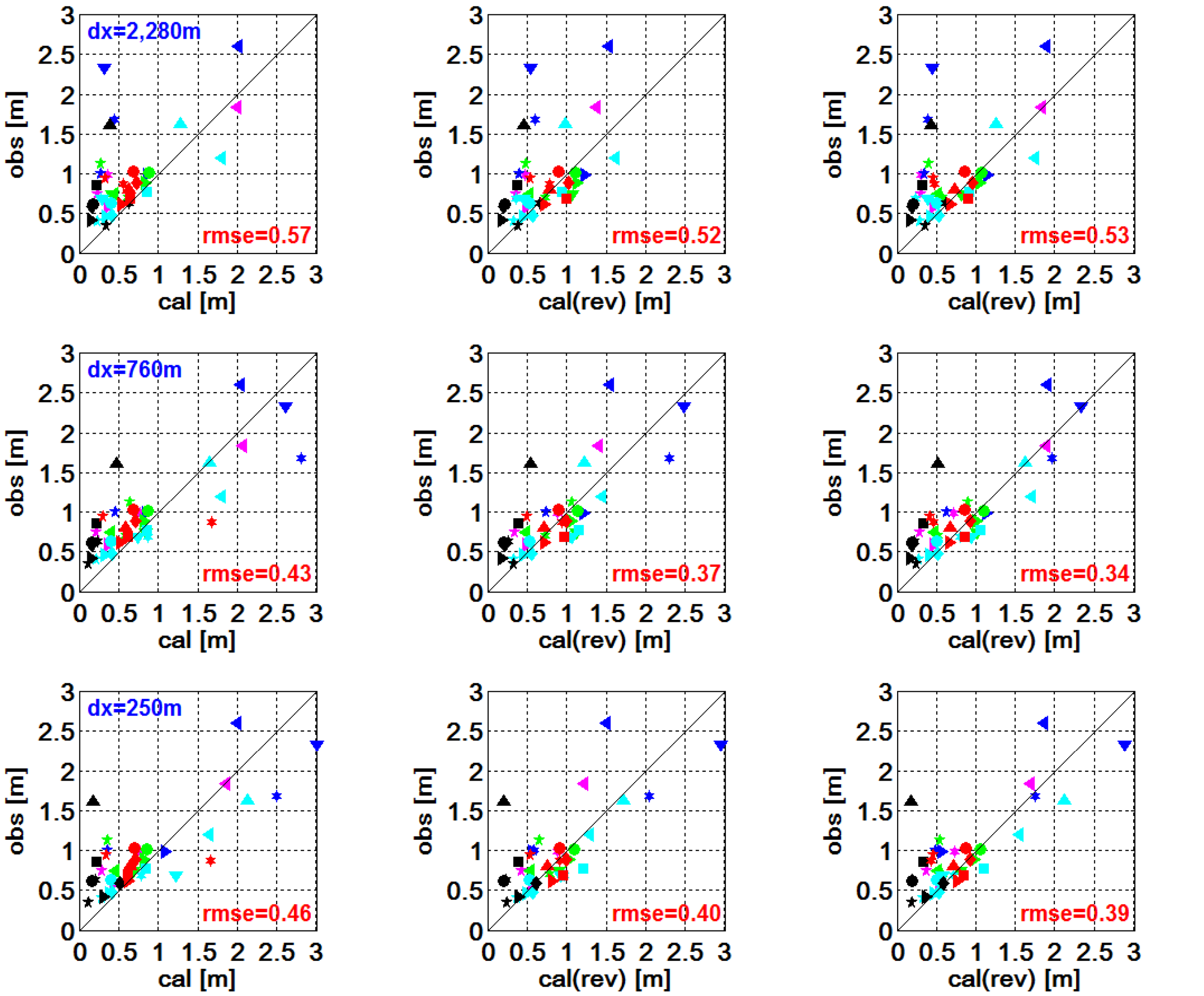

(a) without bias correction (b) with bias correction using the linear regression equation with bias correction using the cubic regression equation

Figure 3.6 Application of bias correction formulas to simulated SSHs calculated using bathymetry data with different resolutions regarding cosď in Equations (3.7) and (3.9) as one. (Each row addresses results using the bathymetry data with different resolutions. Texts at the top left in first panel of each row correspond to the horizontal resolution of bathymetry data. Each column indicates bias correction effect: (a) without bias correction, (b) with bias correction using the linear regression equation and (c) with bias correction using the cubic regression equation. Values at the bottom right in each panel correspond to RMSE values)

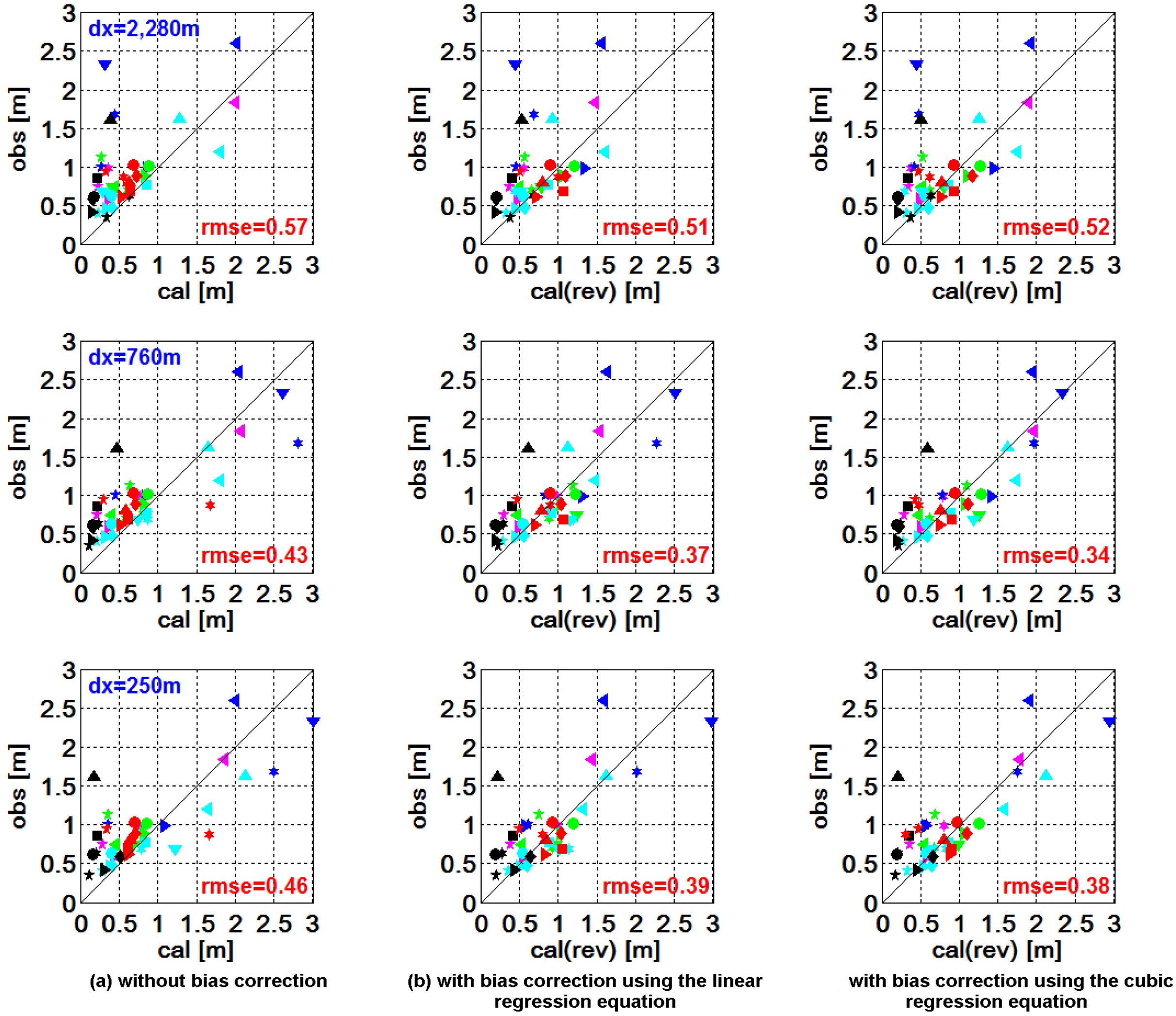

Figure 3.6 Application of bias correction formulas to simulated SSHs calculated using bathymetry data with different resolutions regarding cosθ in Equations (3.7) and (3.9) as real value. (Each row addresses results using the bathymetry data with different resolutions. Texts at the top left in first panel of each row correspond to the horizontal resolution of bathymetry data. Each column indicates bias correction effect: (a) without bias correction, (b) with bias correction using the linear regression equation and (c) with bias correction using the cubic regression equation. Values at the bottom right in each panel correspond to RMSE values)

3.3 Evaluation of the effect of the proposed bias correction on projection of future storm surge heights under simple scenarios

Based on the calibration of fractal dimension based bias correction method, we apply the proposed bias correction along the southeastern coast. The coastline complexity along the southeastern coast of the Korean Peninsula was estimated, shown in Figure 3.8, and was used to correct the results of simple scenario based of the future storm surge heights.

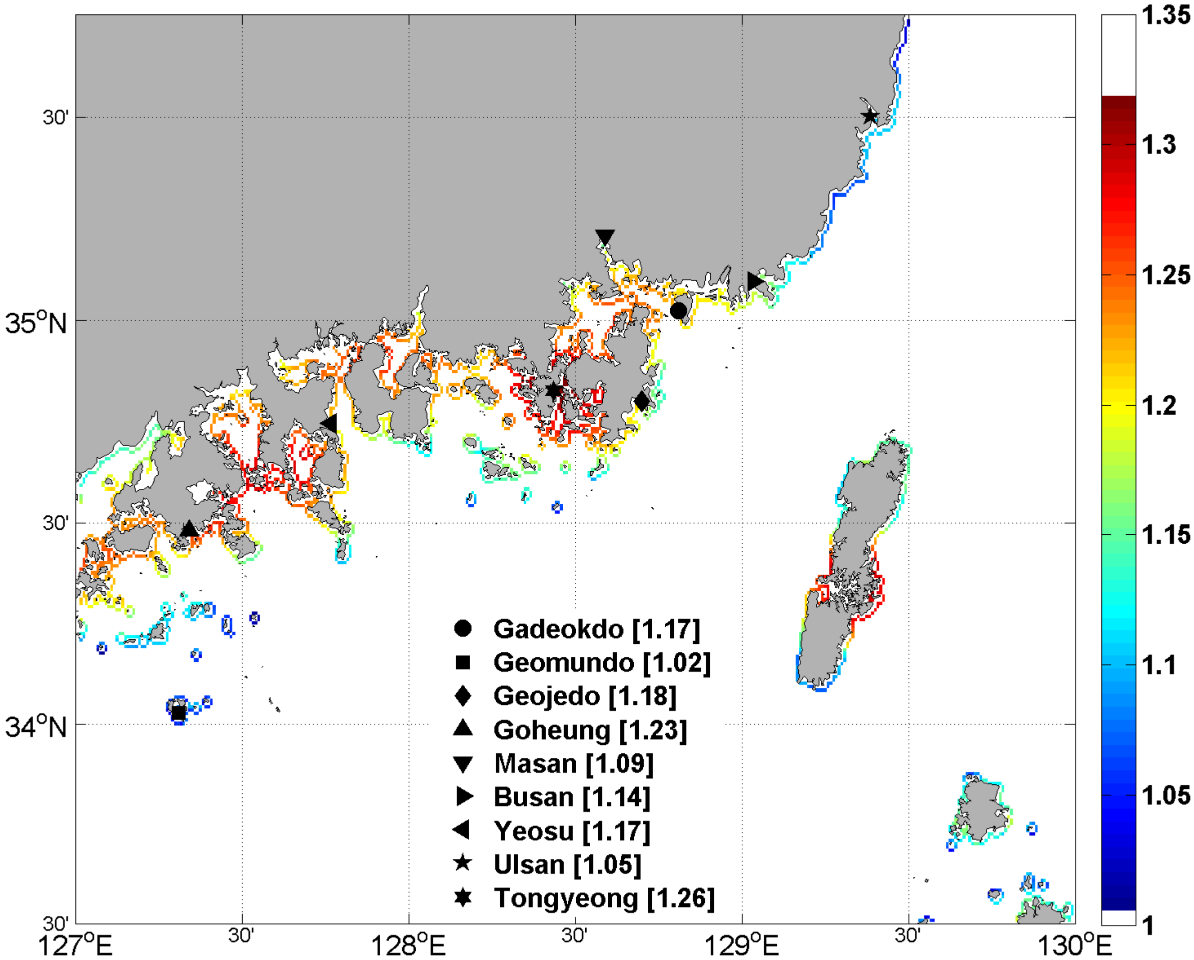

Figure 3.7 Variations of coastline complexity parameters along the southeastern coast of the Korean Peninsula (values in parentheses are fractal dimension of the coastline at corresponding station)

To assess the impact of climate change on storm surge, several approaches exist such as a dynamic approach using the output from a general circulation model or regional climate model (e.g., Yasuda *et* *al.,* 2014), statistical approach based on a stochastic typhoon model (e.g., Nakajo *et al.,* 2013) and worst case approach based on extreme scenarios (e.g., Shibutani *et al.*, 2015). But, there is no quantitative consensus or projections of typhoon intensity in the literature (e.g., IPCC Fifth Assessment Report). Here we performed simple sensitivity tests to select arbitrary number for central pressure drops to reflect the impact of climate change. We designed three future scenarios in which the central pressure drops for the target typhoons were assumed to be 10 hPa (future scenario, abbreviated as D_p10), 20 hPa (D_p20) and 30 hPa (D_p30). All other physical parameters are taken to be the same as in the present scenarios.

The simulated maximum SSHs for all target typhoons under these simple future scenarios showed similar trends (refer to Figure 3.9). The result of Rusa case was analyzed as a typical case. It can be seen that as the central pressure drop becomes larger, the potential maximum SSHs along the coast becomes higher as expected. The potential maximum SSHs modified by LRE and CRE were plotted in the first line of Figures 3.9 (center) and (right), respectively. By applying the bias correction by LRE (CRE), the largest potential maximum SSHs decreased about 22 % (12 %) from 2.59 m to 2.01 m (2.27 m) under the present condition, by 21 % (13 %) from 3.21 m to 2.52 m (2.80 m) under the D_p10, by 21 % (13 %) from 3.85 m to 3.04 m (3.34 m) under the D_p20 and by 20 % (13 %) from 4.52 m to 3.61 m (3.92 m) under the D_p30. Tables 3.1, 3.2 and 3.3 summary the simulate maximum SSHs for each target typhoon event under present and simple future scenarios without bias correction, with bias correction using LRE and CRE, respectively. From these results, we conclude that the bias correction considering the coastline complexity could prevent overestimation of the potential maximum SSHs on the southeastern coast of the Korean Peninsula.

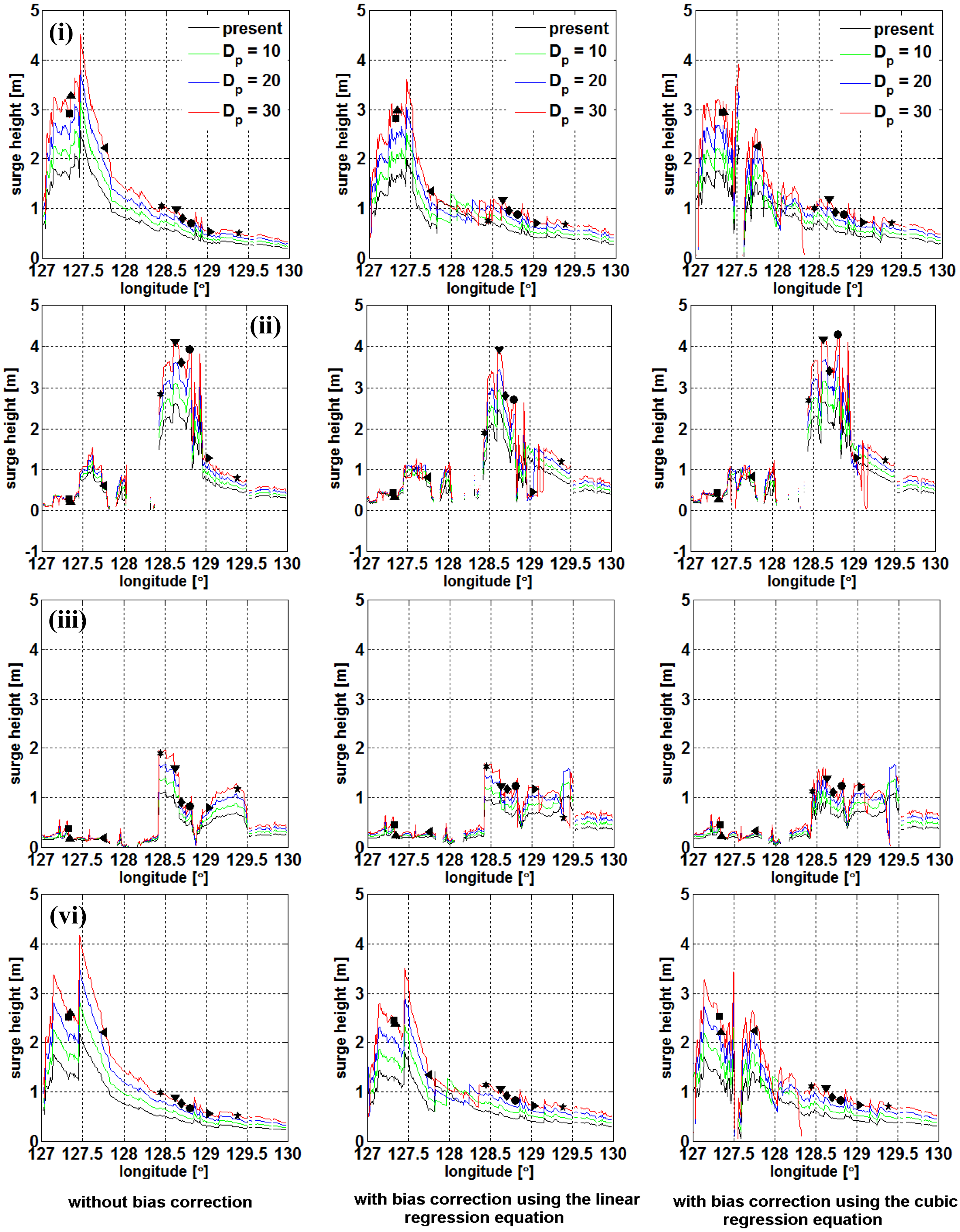

Figure 3.8 Projected future storm surge heights based on historical tracks with modified central pressure. (Each row addresses results by different typhoon events: (i) Rusa, (ii) Maemi, (iii) Megi, (iv) Nari, (v) Bolaven and (vi) Sanba. Each column indicates bias correction effect: (left) without bias correction, (center) with bias correction using the linear regression equation and (right) with bias correction using the cubic regression equation) (continued)

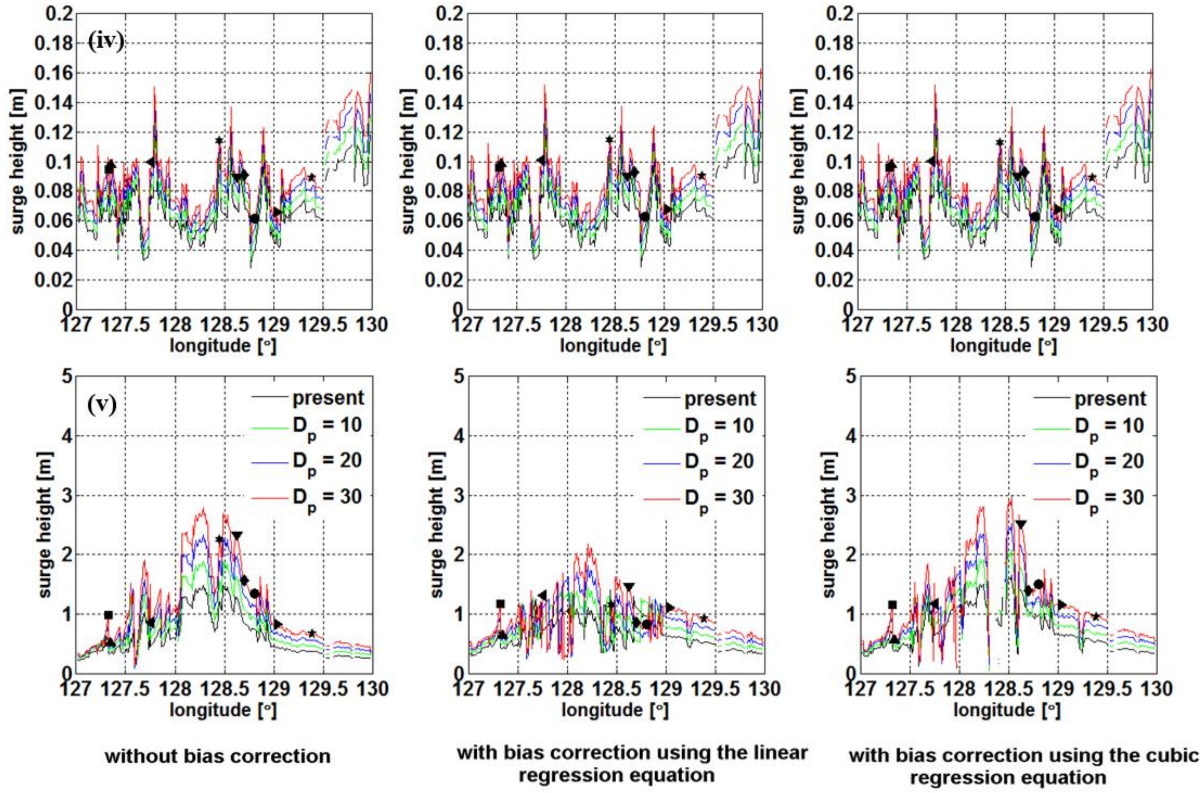

Figure 3.9 Projected future storm surge heights based on historical tracks with modified central pressure. (Each row addresses results by different typhoon events: (i) Rusa, (ii) Maemi, (iii) Megi, (iv) Nari, (v) Bolaven and (vi) Sanba. Each column indicates bias correction effect: (left) without bias correction, (center) with bias correction using the linear regression equation and (right) with bias correction using the cubic regression equation)

Table 3.1 Simulated maximum storm surge heights for each target typhoon event under present and simple future scenarios without bias correction (Dp# means that central pressure for the target typhoons is assumed to be reduced by # hPa in the future)

Future scenario \ Typhoon event		Rusa	Maemi	Megi	Nari	Bolaven	Sanba
present		2.59	2.62	1.11	2.19	0.12	1.48
future	D_p10	3.21	3.11	1.39	2.84	0.13	1.90
	D_p20	3.85	3.62	1.67	3.50	0.15	2.33
	D_p30	4.52	4.13	1.96	4.18	0.16	2.79

Table 3.2 Simulated maximum storm surge heights for each target typhoon event under present and simple future scenarios with bias correction using a linear regression equation (Dp# means that central pressure for the target typhoons is assumed to be reduced by # hPa in the future)

Future scenario \ Typhoon event		Rusa	Maemi	Megi	Nari	Bolaven	Sanba
present		2.01	2.47	1.04	1.80	0.12	1.40
future	D_p10	2.52	2.96	1.31	2.36	0.13	1.46
	D_p20	3.04	3.45	1.60	2.93	0.15	1.81
	D_p30	3.61	3.95	1.69	3.51	0.16	2.18

Table 3.3 Simulated maximum storm surge heights for each target typhoon event under present and simple future scenario with bias correction using a cubic regression equation (Dp# means that central pressure for the target typhoons is assumed to be reduced by # hPa in the future)

Future scenario \ Typhoon event		Rusa	Maemi	Megi	Nari	Bolaven	Sanba
present		2.27	2.82	1.09	1.77	0.12	1.66
future	D_p10	2.80	3.27	1.38	2.31	0.13	2.09
	D_p20	3.34	3.79	1.67	2.87	0.15	2.53
	D_p30	3.92	4.31	1.61	3.44	0.16	2.98

3.4 Summary

The formulas for the model bias correction using the coastline complexity factors were drawn and validated. The simulated results for four of the six typhoons were used to derive the bias correction formulas. The proposed bias correction formulas improved the modelὸs performance by 18 % to 30 %. In validation, the simulated results of the remaining two were used. The RMSE of results without bias correction was reduced by 11 % to 14 % by applying the bias correction method. In general, the root mean square error of results with bias correction decreased by 14 % to 23 % by applying the bias correction. It can be seen that the bias correction method considering the coastline complexity can improve modelὸs accuracy.

In addition, the effect of the proposed bias correction on projection of future storm surge heights was examined by performing simple sensitivity tests to consider only central pressure drops to reflect the impact of climate change. By applying the bias correction, the largest potential maximum storm surge heights decreased by 20 % from 4.52 m to 3.61 m under the future scenario 3. From these results, it can be seen that the proposed bias correction method can improve modelós accuracy and prevent potential overestimation of the potential maximum SSHs on the southeastern coast of the KP.

The bias correction method proposed in the study is able to be applied to other storm surge modeling or the other type of model which results depend on coastal topography. However, further refinements of the proposed bias correction method considering not only coastal complexity but also other characteristic such as depth and sea bottom slope remain the next challenge.

Chapter 4.

Assessment of Uncertainties of Projection of Typhoons and Storm Surge Heights under Future Climate based on Ensemble Experiments with Multi-SST and Multi-Global Warming Scenario using Single Atmospheric Global Climate Model

4.1 Introduction

There are many possibility and uncertainty to make an impact assessment of climate change on storm surge. Thus, to assess the impact of climate change on storm surge, several approaches exist such as 1) dynamic approach using the output from a global climate model (hereafter, GCM) or regional climate model (e.g., Yasuda *et al.*, 2014), 2) statistical approach based on a stochastic typhoon model (e.g., Nakajo *et al.*, 2013) and 3) worst case approach based on extreme scenarios (e.g., Shibutani *et al.*, 2015;). However, each approach has advantages and disadvantages. For example, as to approach #1), uncertainty of future typhoon projection depending on the GCMôs ability and accuracy and input conditions may cause uncertainty in future storm surge projection. Additionally the period of projection and ensemble member are limited. However, this approach makes it possible to project storm surge heights on regional scales and to identify the factors which can contribute to future storm surge. Approach #2) can produce a large number of samples to estimate the return period which is necessary for coastal structure design. However, the approach is limited to a specific location. Also there is uncertainty depending on the assumptions for future climate change. Finally, approach #3) can estimate the possible maximum values of future storm surge, but it is limited to a specific location and its return period is unclear. In addition, it is unknown whether the result has meteorological consistency. The objective of this chapter is to identify vulnerable areas by projecting possible future SSH on a regional scale. In this study, future SSHs along the southeastern region in the Korean Peninsula is projected by approach #1) using typhoon information based on a single-model GCM developed by the Japanese Meteorological Research Institute, denoted as MRI-AGCM3.2H (Mizuta *et al.*, 2012).

Nevertheless, as mentioned above, when projecting future changes in a tropical cyclone (hereafter, TC) including typhoons by using GCM, there are several uncertainties due to a number of factors: differences in model physics parameterization (e.g. Yokoi and Takayabu 2009; Yokoi *et al.*, 2009; Walsh *et al.* 2010; Murakami *et al.* 2011), model resolution (e.g. Bengtsson *et al.*, 2007; Murakami and Sugi 2010), chosen global warming scenario (e.g. Stowasser *et al.*, 2007), given spatial pattern of sea surface temperature (hereafter, SST) under future climate condition for the case of AGCM (Emanuel, 2005; Sugi *et al.*, 2009; Zhao *et al.*, 2009; Murakami *et al.*, *et al.*,2011) and methods used to detect TCs (Walsh *et al.*, 2007). The ranges of uncertainties are different for each source.

Of the several uncertainties, regarding uncertainty by physical parameterization and resolution of MRI-AGCM3.2H, some recommendations have been proposed by reviewing model accuracy in the basin scale. First, for the model physical parameterization, Kitoh *et al.* (2016) found that a factor of the uncertainty lies in the cumulus convection scheme among physical processes, as the TC consists of convective systems in which individual cumulus convection gathers together. Mizuta *et al.* (2012) conducted the multi-physics ensemble simulations with three cumulus convection schemes: a prognostic Arakawaï Schubert (AS) cumulus convection scheme (Arakawa and Schubert 1974; Randall and Pan 1993); a new cumulus convection scheme, called the óóYoshimura scheme (YS)ôô after a model developer at the MRI (Yukimoto *et al.*, 2011); and the Kainï Fritsch (KF) convection scheme (Kain and Fritsch 1990, 1993). They reached the conclusion that the use of the YS scheme in the MRI-AGCM yields a more realistic simulation of tropical precipitation than the use of the AS scheme. Next, for model resolution, Murakami and Sugi (2010) investigated effects of model resolution on climatological features of the TCs by comparing four resolution versions (180, 120, 60, and 20-km mesh). The finest resolution (20-km) showed the best outputs in terms of TC intensity and inter-annual and seasonal variations in TC genesis number. Resolutions of 60-km mesh and finer showed a significant future increase in the frequency of intense TCs, whereas the lower resolution versions coarser than 60-km showed no such change, suggesting that 60-km mesh is the critical resolution in projecting future change in the frequency of intense TCs. On the other hand, a few studies have assessed uncertainty by global warming scenarios and spatial pattern of future SST. Beside uncertainties in physics and numerical modeling of GCMs, the effects of the global warming scenario and spatial pattern of future SST on projection of future TCs are also quite important for climate projection and related impact assessment. The uncertainties resulting from physics and numerical modeling can be reduced by developing the GCMs while the ones resulting from the global warming scenario and spatial pattern of SST cannot reduced. It is reported that the different global warming scenarios give quite different future climate change characteristics and the given future SST pattern with the same scenario also gives different climate impacts in the regional scale (e.g. Murakami *et al.*, 2012b; Mizuta *et al.*, 2014; Kitoh and Endo, 2016).

Thus, this chapter assesses the uncertainties of global warming scenarios and spatial pattern of SSTs on the projection of typhoons and SSHs affecting the KP under future climate condition based on typhoon data extracted from the output of ensemble experiments using MRI-AGCM3.2H. First, the reproducibility of the typhoon data from each ensemble experiment is estimated by comparison with observed typhoon data, and future changes and uncertainty of typhoon properties such as track, genesis number and intensity are discussed. Furthermore, a series of storm surge simulations targeting the southeastern coast in the KP are conducted by using the typhoon data from each ensemble experiment. For the maximum SSH during the future climate, uncertainty in the choice of global warming scenario and the assumption of a specific spatial pattern of SST are estimated. The remainder of this chapter is organized as follows. Section 4.2 briefly introduces the ensemble experiments, a TC detection method and storm surge simulation setup. Section 4.3 discusses the results of the TC characteristics affecting the KP under the present and future climates. Section 4.4 examines the future SSH around the southeastern coast of the KP. Section 4.5 provides a summary of conclusions in this chapter.

4.2 Methodology

4.2.1 Outline of ensemble experiments with multi-SST and multi-global warming scenario using single AGCM

The GCM model used for the ensemble experiments is the Meteorological Research Institute Atmospheric General Circulation Model version 3.2 (MRI-AGCM3.2; Mizuta *et al.*, 2012). MRI-AGCM3.2 is based on a global forecast model developed by the JMA and is tuned for climate projection by MRI (Mizuta *et al.*, 2006). MRI-AGCM3.2 is revised version (MRI-AGCM3.1) used for the CMIP3 experiments. Many parameterization schemes for various physical processes are newly developed and were introduced into the model (Kitoh *et al.*, 2009). The projections by MRI-AGCM3.2 were conducted using two different resolutions with 60 km resolution and 20 km resolution. The models with each resolution are referred to as MRI-AGCM3.2H and MRI-AGCM3.2S (where óHômeans high resolution and óSômeans super-high resolution), respectively.

A series of ensemble experiments using MRI-AGCM3.2 were conducted by different research groups (Kitoh *et al.*, 2016). Among them, two ensemble experiments are introduced here briefly and detailed description of the ensemble simulations is given by Kitoh *et al.* (2016). The first experiment introduced here is performed under the SOUSEI Program which was a 5-year (FY2012-2016) project named as ñProgram for Risk Information on Climate Changeò. Time-slice experiments were performed for 25 years in the present climate (1979-2003) and in the future climate (2075-2099). The present climate projection was conducted using observed monthly mean SSTs and sea ice concentrations according to the Hadley Centre Global Sea Ice and Sea Surface Temperature dataset (HadISST1; Rayner *et al.*, 2003). Future climate projections were conducted using three SST patterns obtained by a cluster analysis of SSTs from 28 model in the Coupled Model Inter-comparison Project phase 5 (CMIP5) under the Representative Concentration Pathway (RCP) 8.5 scenario (Mizuta *et al.*, 2014) as well as mean SST pattern of 28 models in CMIP5 under same scenario. The second one was carried out by the Ministry of the Environment Climate Projections for Adaptation. Time-slice experiments were performed for the 20 years in the present climate (1984-2004) and in the future climate (2080-2100). For the present condition, three simulations with different cumulus schemes, the Yoshimura (YS; Yukimoto *et al.*, 2011), Kain-Fritch (KF; Kain and Fritsch 1990) and Arakawa-Schubert (AS; Randall and Pan 1993) schemes, are performed. For the future condition, eighteen simulations are conducted. Twelve experiments among them are conducted under the YS scheme using three SST clusters with four global scenarios which are RCP2.6, RCP4.5, RCP6.0 and RCP8.5. The remaining six experiments are performed under the RCP8.5 scenario using additionally two cumulus schemes with three different SST pattern.

In this study, to evaluate the effects of global warming scenarios and spatial pattern of SSTs on future SSHs, the output of seven ensemble experiments with the YS scheme were used: one experiment under the present climate condition, three experiments with different spatial pattern of SSTs under the RCP8.5 scenario, and three experiments with a different global warming scenario using mean SST pattern of 28 models in CMIP5 under the same scenario. However, since the simulation periods between the two groups is different, this study used only the output data from 1984 to 2003 for the present climate and the output data from 2080 to 2099 for the future climate. The experiments used in this study are shown in Table 4.1 and each experiment is abbreviated for convenience. Typhoon data extracted from the output of seven ensemble experiments using the TC detection method by Murakami *et al.* (2012a) are used to project the future SSHs around the KP.

Table 4.1 Conditions of ensemble experiments by MRI-AGCM

abbreviation	SST	scenario	period	cumulus scheme	Source program
HPA_S	HadISST1.1	Present	1979-2003	YS	SOUSEI
	HadISST1.1	Present	1979-2003	KF	
	HadISST1.1	Present	1979-2003	AS	
HFA_rcp26_c0	CMIP5 mean	RCP 2.6	2075-2099	YS	
HFA_rcp45_c0	CMIP5 mean	RCP 4.5	2075-2099	YS	
	CMIP5 mean	RCP 6.0	2075-2099	YS	
HFA_rcp85_c0	CMIP5 mean	RCP 8.5	2075-2099	YS	
	CMIP5 mean	RCP 8.5	2075-2099	KF	
	CMIP5 mean	RCP 8.5	2075-2099	AS	
HPA_M	HadISST1.1	Present	1984-2004	YS	MoE
	HadISST1.1	Present	1984-2004	KF	
	HadISST1.1	Present	1984-2004	AS	
HFA_rcp85_c1	CMIP5 cluster 1	RCP 8.5	2080-2100	YS	
HFA_rcp85_c2	CMIP5 cluster 2	RCP 8.5	2080-2100	YS	
HFA_rcp85_c3	CMIP5 cluster 3	RCP 8.5	2080-2100	YS	
	CMIP5 cluster 1	RCP 8.5	2080-2100	KF	
	CMIP5 cluster 2	RCP 8.5	2080-2100	KF	
	CMIP5 cluster 3	RCP 8.5	2080-2100	KF	
	CMIP5 cluster 1	RCP 8.5	2080-2100	AS	
	CMIP5 cluster 2	RCP 8.5	2080-2100	AS	
	CMIP5 cluster 3	RCP 8.5	2080-2100	AS	
	CMIP5 cluster 1	RCP 6.0	2080-2100	YS	
	CMIP5 cluster 2	RCP 6.0	2080-2100	YS	
	CMIP5 cluster 3	RCP 6.0	2080-2100	YS	
	CMIP5 cluster 1	RCP 4.5	2080-2100	YS	
	CMIP5 cluster 2	RCP 4.5	2080-2100	YS	
	CMIP5 cluster 3	RCP 4.5	2080-2100	YS	
	CMIP5 cluster 1	RCP 2.6	2080-2100	YS	
	CMIP5 cluster 2	RCP 2.6	2080-2100	YS	
	CMIP5 cluster 3	RCP 2.6	2080-2100	YS	

4.2.2 TC detection method

This subsection briefly describes the TC detection method by Murakami et al. (2012a). It detects TCs in the model by using six globally uniform criteria for 6-hourly model outputs. These criteria are based on those by Oouchi *et al.* (2006) with some modifications (Murakami *et al.* 2011). Some criteria are optimized for a given model configuration to ensure that the global annual mean TC number under the present climate condition matches that observed (84 per year for the period 1979ï 2003). The values listed after each of the following criteria show the model-dependent values used for the optimization (here, value for MRI-AGCM3.2H using YS scheme is only presented in bold):

1) The maximum relative vorticity at 850 hPa exceeds 8.0×10^{-5} s^{-1}.

2) The maximum wind speed at 850 hPa exceeds 13.0 m/s.

3) There is an evident warm core aloft, namely, the sum of the temperature deviations at 300, 500, and 700 hPa exceeds 0.8 K. The temperature deviation for each level is computed by subtracting the maximum temperature from the mean temperature over the 10°×10° grid box centered nearest to the location of maximum vorticity at 850 hPa.

4) The maximum wind speed at 850 hPa is greater than the maximum wind speed at 300 hPa.

5) To remove tropical monsoon depressions in the North Indian Ocean (NIO), the radius of maximum mean wind speed must be less than 200 km from the detected storm center. This condition is applied in the NIO only.

6) The duration of each detected storm must exceed 36 h. When a single TC satisfies all the criteria only intermittently, it is considered as multiple TC generation events. To prevent multiple counts of a single TC, a single time step failure is allowed.

4.2.3 Simulation setup of storm surge

A series of storm surge projections corresponding to the typhoon events extracted from ensemble experiments using MRI-AGCM3.2H was conducted using a coupled surge, wave and tide model (SuWAT) developed by Kim *et al.* (2008). The SuWAT model is composed of a surge model based on the depth-integrated non-linear shallow water equations, a third-generation spectral wave model (SWAN version 40.41) and a regional astronomical tide model around Japan (Matsumoto, 2000). The SuWAT model can contain an arbitrary number of nested domains to calculate the high resolution storm surge levels by the message passing interface. In this study, only the surge module was used.

Each simulation was carried out with 48 hours spin-up prior to the calculation of the typhoon event to bring stability to the sea surface level over the entire computational domain. To produce the atmospheric fields of each typhoon event, the Fujita model and the Mitsuyasu-Fujii mode are employed for pressure distribution and wind distribution, respectively. The maximum wind radius (R_{max}) of each typhoons was calculated by an empirical formula based on observed data (Yasuda *et al.*, 2010).

Four-domain nesting was used with a 1:3 ratio of spatial grid size from coarse grid to fine grid (shown by the dashed rectangles in Figure 4.1). The outermost domain (D1) is set in the region of 20°~42°N, 117°~132°E that almost covers the formation and dissipation of typhoons approaching to the KP. The innermost domain (D4) is the region 33.5°~35.75°N, 127°~130°E which we define as the southeastern area of the KP and has a spatial resolution of 0.008333° (about 760 m). Table 4.2 shows the information for each calculation domain.

The bathymetry data in D1 were given from the General Bathymetric Chart of the Oceans (GEBCO, 2003). For the remaining nested domains, the bathymetry data were derived from the Digital 30 s Gridded Bathymetric Data of the Korea Marginal Seas dataset (Seo, 2008). The time step of storm surge computation was 300 s. The inundation was not considered.

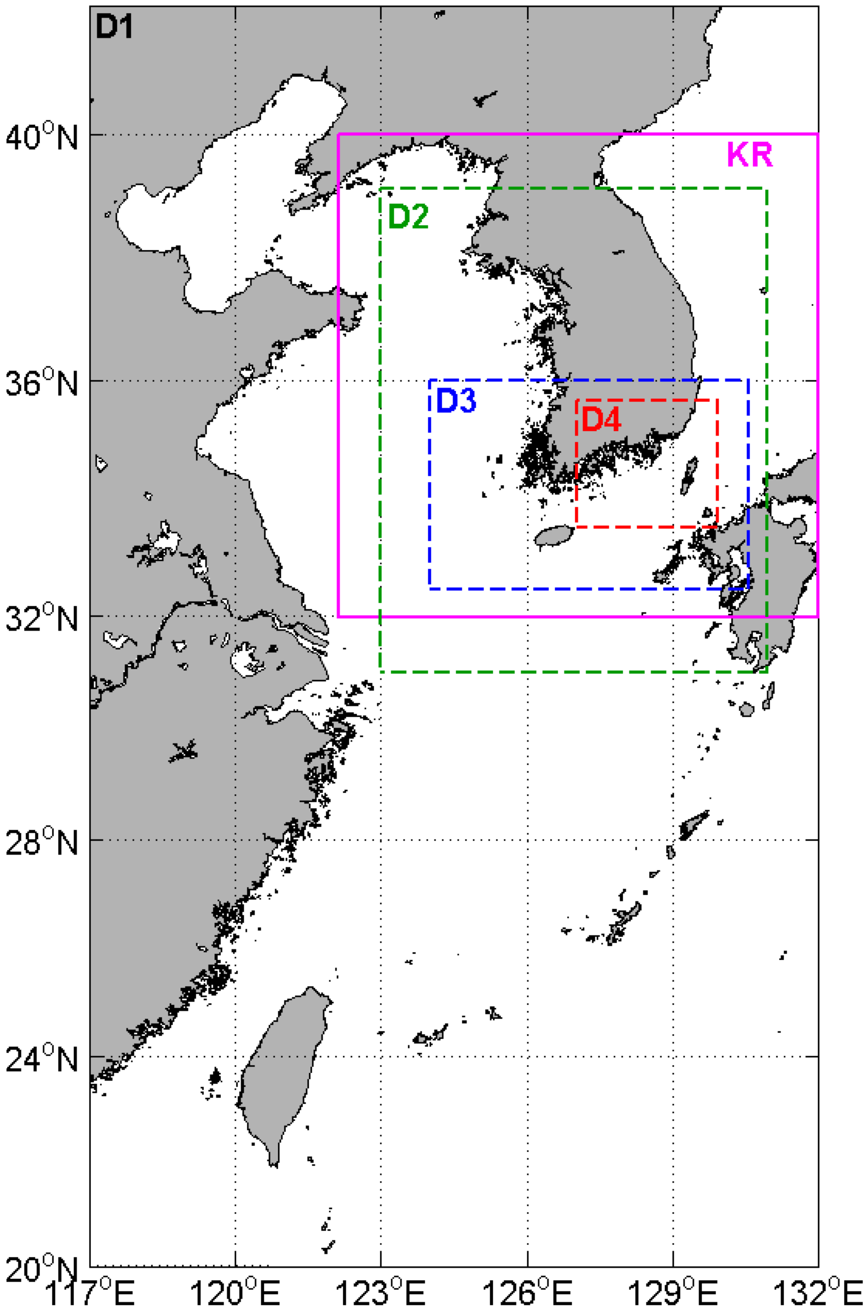

Figure 4.1 Definition area for typhoons affecting the Korean Peninsula (abbreviated as ñKRò written in purple color on the upper right corner) and computation domains of storm surge projections (abbreviated as ñD#ò,   # is the number of domain)

Table 4.2 Information of each calculation domain

# of Domain	The range of domain	The grid size	# of grids
1	117°E ~ 132°, 20°N ~ 42°N	qx = 9,059.8m, qy = 11,560.5 m	151 x 211
2	123°E ~ 131°, 31°N ~ 39°N	qx = 4,563.2m, qy = 5,547.1m	160 x 160
3	124°E ~ 130.5°, 32.5°N ~ 36°N	qx = 2,281.8m, qy = 2,773.2m	260 x 140
4	127°E ~ 130°, 33.5°N ~ 35.75°N	qx = 760.7m, qy = 924.5 m	360 x 270

4.3 Validation of the simulated typhoon characteristics affecting the Korean Peninsula and projection of their future changes

The projected typhoons by the GCMs have biases both number, tracks and intensity due to limitation of physics and numerical modeling. Therefore understanding and correction of biases of projected typhoons by the GCMs is important before to conduct impact assessment. Typhoon properties such as the number, track and central pressure detected from output of an experiments using MRI-AGCM3.2H under the present climate condition were verified by comparing with those of the observed typhoon dataset from the International Best Track Archive for Climate Stewardship (IBTrACS; Knapp *et al.*, 2010). This dataset consists of information on TC track, intensity, and other related parameters at 6-hour intervals based on observations. In addition, future changes of typhoons properties were discussed by comparing typhoon data detected from output of the ensemble experiments. Here, we focused on typhoons affecting the Korean Peninsula (hereafter, typhoons around KP) which pass through the region of 32°-40°N and 122°-132°E. The properties of all typhoons in global and ocean-basin scale detected from the output were examined in Murakami *et al.* (2012b).

4.3.1 The number

First, the reproducibility and characteristics of future change of the number of typhoons around KP were estimated. Figure 4.2 shows probability of the annual number of the typhoons under the present and the future climate conditions. The total number of the typhoons under present climate conditions are 74 (3.7 per year) and 26 (1.3 per year) for IBTrACS and HPA, respectively. Results for the simulation underestimate the actual number of the typhoons. Note that the TC detection method applied in this study is set to match the observed annual cyclogenesis global number. Although the annual number of cyclogenesis is similar in the global zone including the Western North Pacific basin (Murakami et al, 2012b), the annual number of the typhoons can vary. It is presumed that the typhoon generated by MRI-AGCM3.2H will disappear before reaching the KP.

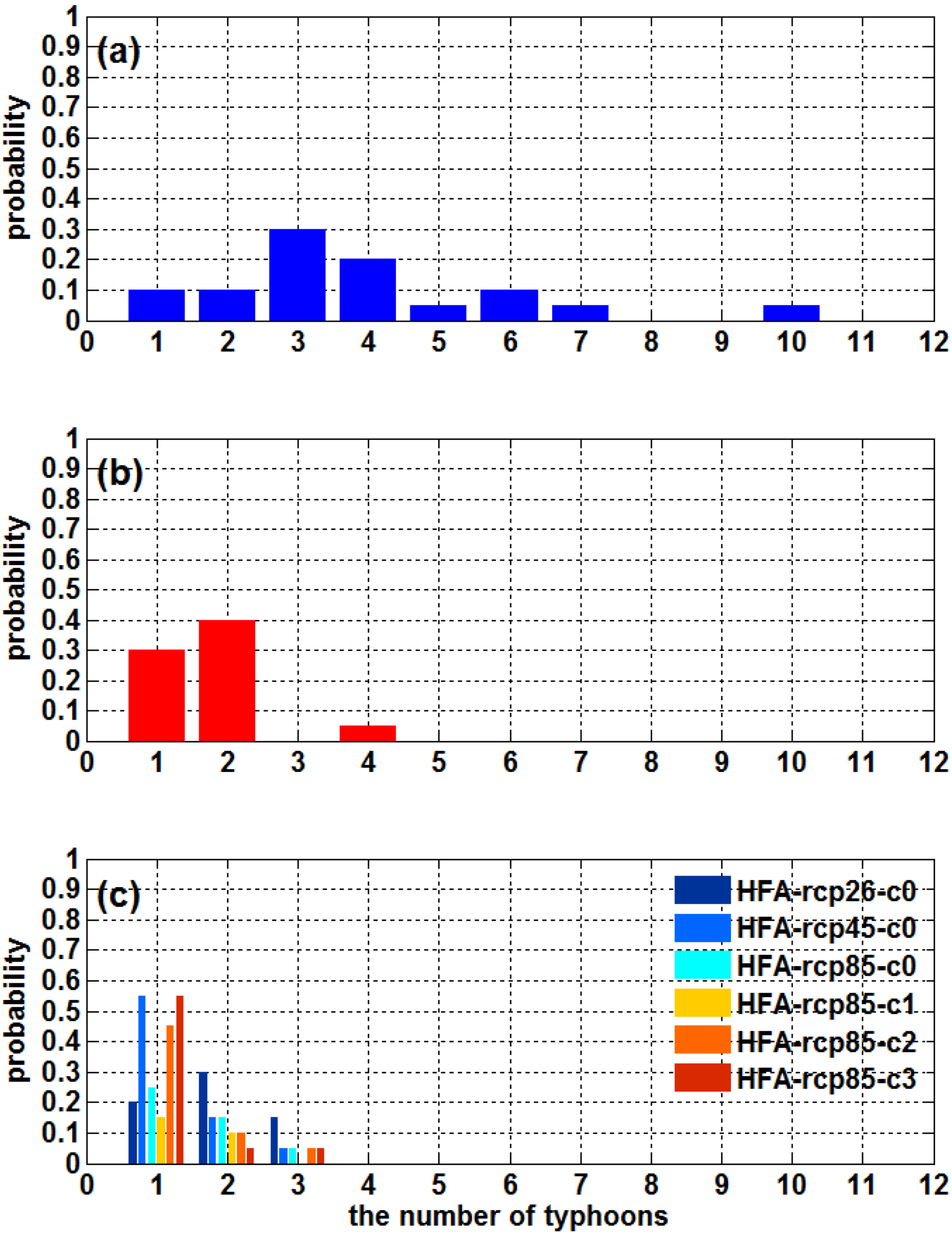

Figure 4.2 Probability of annual number of typhoons passing around the Korean Peninsula for (a) observations (IBTrACS) from 1984 to 2003, (b) simulation using MRI-AGCM3.2H under present climate condition from 1984 to 2003 and (c) projection using MRI-AGCM3.2H

The total numbers of the typhoons in each experiment under the future climate condition are 25 in HFA-rcp26-c0, 20 in HFA-rcp45-c0, 14 in HFA-rcp85-c0, 7 in HFA-rcp85-c1, 16 in HFA-rcp85-c2 and 16 in HFA-rcp26-c3, respectively, while it is 26 under the present climate condition. Future change rate of the number of the typhoons ($N_{furue\ change}$, %) is calculated as

$$N_{future\ change} = \frac{N_{future} - N_{present}}{N_{present}} \times 100 \qquad (4.17)$$

Where $N_{present}$ and N_{future} are the numbers of the typhoons in the present climate and the future climate, respectively. It is found that the number of the typhoons is significantly reduced for each ensemble experiment in the future climate condition, ranging from 4 % to 73 %. In terms of general impacts of climate scenarios, the total number of the typhoons tends to decrease as greenhouse gas concentrations increase. As to SST pattern, the HFA-rcp85-c1 experiment shows the smallest typhoon number of the typhoons than the other SST experiments. The numbers of the typhoons in other conditions are similar. These results indicate that future changes of the number of the typhoons depends on the chosen global scenario and the assumed spatial pattern of SST changes. A summary of the characteristics of the number of the typhoons for each ensemble experiment is given in Table 4.3.

4.3.2 Tracks

Next, the characteristic of tracks of typhoons around KP were assessed. Figure 4.3 shows tracks of the typhoons under the present and future climate conditions. Although the projection by HPA generates fewer typhoons compared to observations, the general trend of typhoon tracks is in good agreement with observations. For example, after typhoons are generated in the area of 10°-20°N and 120°-140°E, they go west in the South China Sea. Then the typhoons change their trajectory to the northeast toward the KP near Taiwan and approach the western and southern coasts of the KP.

Figures 4.3 (b), (c), (d) and (h) compare ensemble experiments using different spatial pattern of SST under same global scenario, RCP8.5. In all experiments, the locations of typhoon genesis and typhoon lysis are projected to shift to the northwest while the paths are changed depending on the spatial pattern of SST during each typhoon developing period. In HFA-rcp85-c2 and HFA-rcp85-c0,

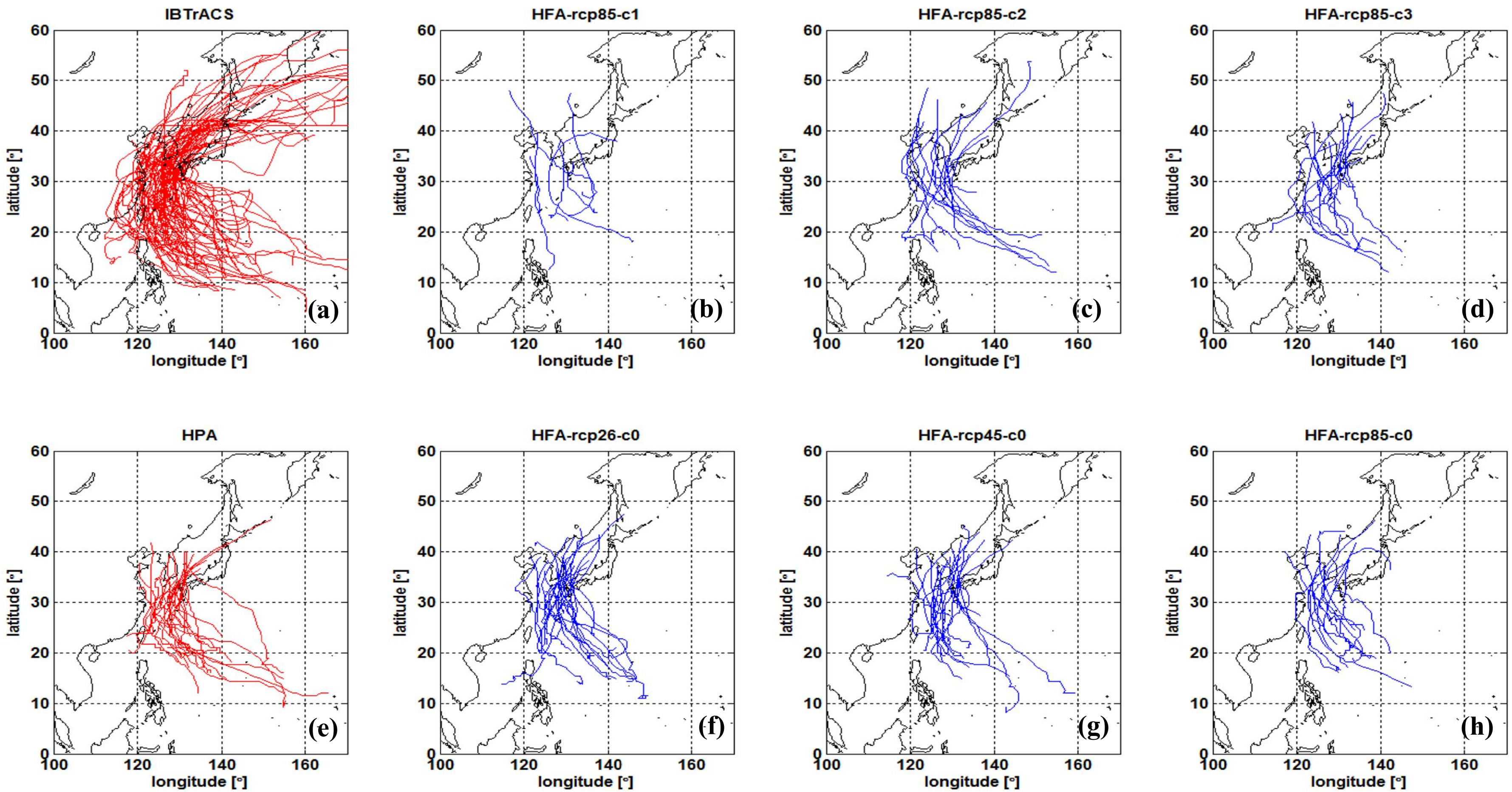

Figure 4.3 Tracks of selected typhoons passing around the Korean Peninsula of (a) observations (IBTrACS) under the present climate condition, (b) projection under the rcp8.5 scenario using Cluster 1 of CMIP5 SST (abbreviated as ñHFA-rcp85-c1ò), (c) HFA -rcp85-c2, (d) HFA-rcp85-c3, (e) simulation under the present climate condition (abbreviated as ñHPAò), (f) projection under the rcp2.6 scenario using ensemble mean of CMIP5 SST experiments (abbreviated as ñHFA-rcp26-c0ò), (g) HFA-rcp45-c0 and (h) HFA-rcp85-c0

the typhoons change their track to the northeast near Shanghai which is north of Taiwan. As a result, the number of typhoons passing the west sea of the KP is projected to increase. In HFA-rcp85-c3, the typhoons change their track to the northeast near Taiwan like the present climate condition then some of them recurve to the north in the vicinity of the Korea/Tsushima Strait. As a result, the number of typhoons approaching the east coast of the KP is projected to increase. In HFA-rcp85-c1, the number of typhoons is too small, only 7 typhoons, to distinguish significant features.

Figure 4.3 (f), (g) and (h) compare ensemble experiments under different global warming scenario using the same spatial pattern of SST, the ensemble mean of CMIP5 SST, denoted c0. Locations of typhoon genesis and typhoon lysis are expected to shift to the northwest for all experiments. This tendency becomes more pronounced as the greenhouse gas emissions increase. As to typhoon tracks, after generating the typhoons move to the west in the South China Sea which is same as under the present climate condition. However, the typhoons change their trajectory to the north in the vicinity of 30°N. According to the analysis of the future Typhoons around KP tracks, locations of typhoon genesis and typhoon lysis are projected to shift to the northwest. As the typhoon movements are changed unlike the present, it is projected that the number of typhoons approaching the West and South coast of the KP increase. The degree of change in typhoon tracks will vary depending on the spatial pattern of SST and global warming scenario.

4.3.3 Minimum central pressures

Finally, the feature of minimum central pressures of typhoons around KP were estimated. Figure 4.4 shows probability histogram and probability density functions of minimum central pressure of the typhoons under the present climate condition. Mean values of the minimum central pressure of the typhoons are 981.6 hPa and 972.8 hPa for IBTrACS and HPA, respectively. The mean value for HPA is smaller than IBTrACS by 8.8 hPa. Mori and Takemi (2016) indicated MRI-AGCM3.2H tends to have a lower central air pressure due to the weak representation of wall cloud. However, since this difference cannot be ignored, the values of minimum central pressure from all ensemble experiments using MRI-AGCM3.2H were linearly calibrated. As a result calibration, the probability distribution for HPA corresponds well to one of IBTrACS.

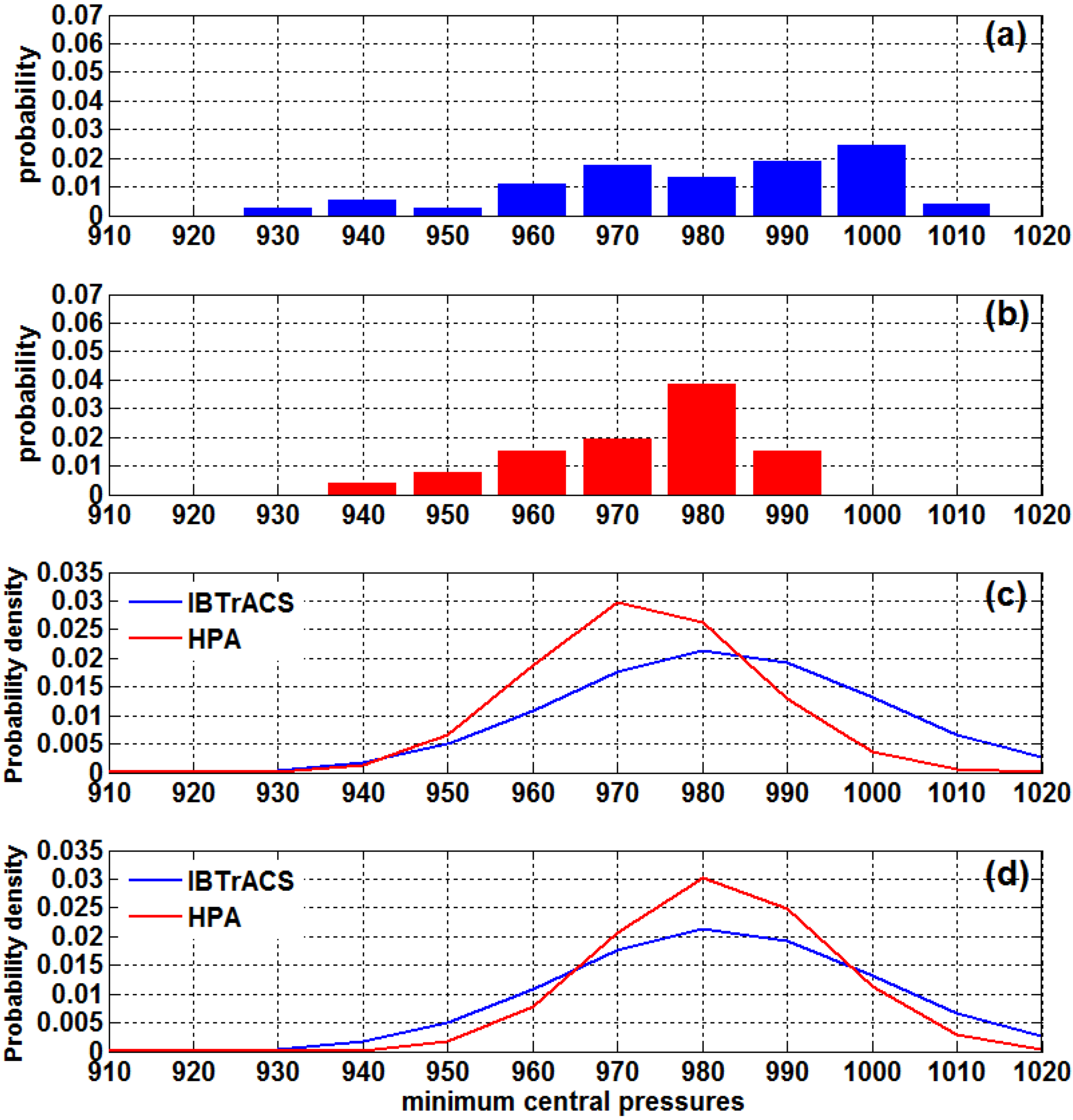

Figure 4.4 Probability of minimum central pressure of typhoons passing around the Korean Peninsula for (a) observations (IBTrACS) and (b) simulation using MRI-AGCM3.2H (HPA) and probability density functions of the minimum central pressure of the typhoons for IBTrACS and HPA (c) without correction of bias of the minimum central pressures and (d) with correction of the bias under present climate condition from 1984 to 2003

Figure 4.5 (a) shows probability of minimum central pressure of the typhoons under the present and future climate condition. Mean of the minimum central pressure will varies with the spatial pattern of SST and global warming scenario. Moreover, it is indicated that frequency of intense typhoons is forecast to increase. Figure 4.5 (b) presents probability density functions of the minimum central pressure for the present and future ensemble experiments using the different global warming scenarios under same SST pattern, c0. The mean values of the minimum central pressure in each experiment are 981.6 hPa in HPA, 974.0 hPa in HFA-rcp26-c0, 970.7 hPa in HFA-rcp45-c0, 968.6 hPa in HFA-rcp85-c0, respectively. The rate of change for those in the future climate declines in the range of 0.8 % to 1.4 %. The magnitude of the rate of change grows as the greenhouse gas emissions increase. Figure 4.5 (c) illustrates the probability density functions for different spatial pattern of SST under same global scenario, RCP8.5. The mean values of the minimum central pressure in each SST pattern experiment are 968.6 hPa in HFA-rcp85-c0, 968.1 hPa in HFA-rcp85-c1, 969.1 hPa in HFA-rcp85-c2, 969.1 hPa in HFA-rcp85-c3, respectively. The rate of change for those in the future climate decreases from 1.3 % to 1.4 %. The degree of the rate of change by SST patterns is smaller than the one by the global warming scenarios. A summary of the characteristics of the minimum central pressure of the typhoons for each ensemble experiment is given in Table 4.3.

From the above discussions, under present climate condition, the number of typhoons around KP based on the output of the ensemble experiments using MRI-AGCM3.2H underestimated comparing to the observations, while the general trend of the tracks of them corresponded with the observations. Also the mean value of the minimum central pressure of them is smaller than observations by 8.8 hPa. Since this difference cannot be ignored in projecting future storm surge heights, the values of minimum central pressure from all ensemble experiments were linearly calibrated. The corrected values were used to project future storm surges. Under future climate condition, the number and intensity of the typhoons around KP are expected to decrease and the locations of typhoon genesis and typhoon lysis are projected to shift to the northwest for all ensemble experiment. However, the extent of each change is anticipated to vary depending on the conditions of SST pattern and global warming scenario. Subsection 4.4 assesses the uncertainties of SST patterns and global warming scenarios on the projection of SSHs around the KP using the typhoons around KP.

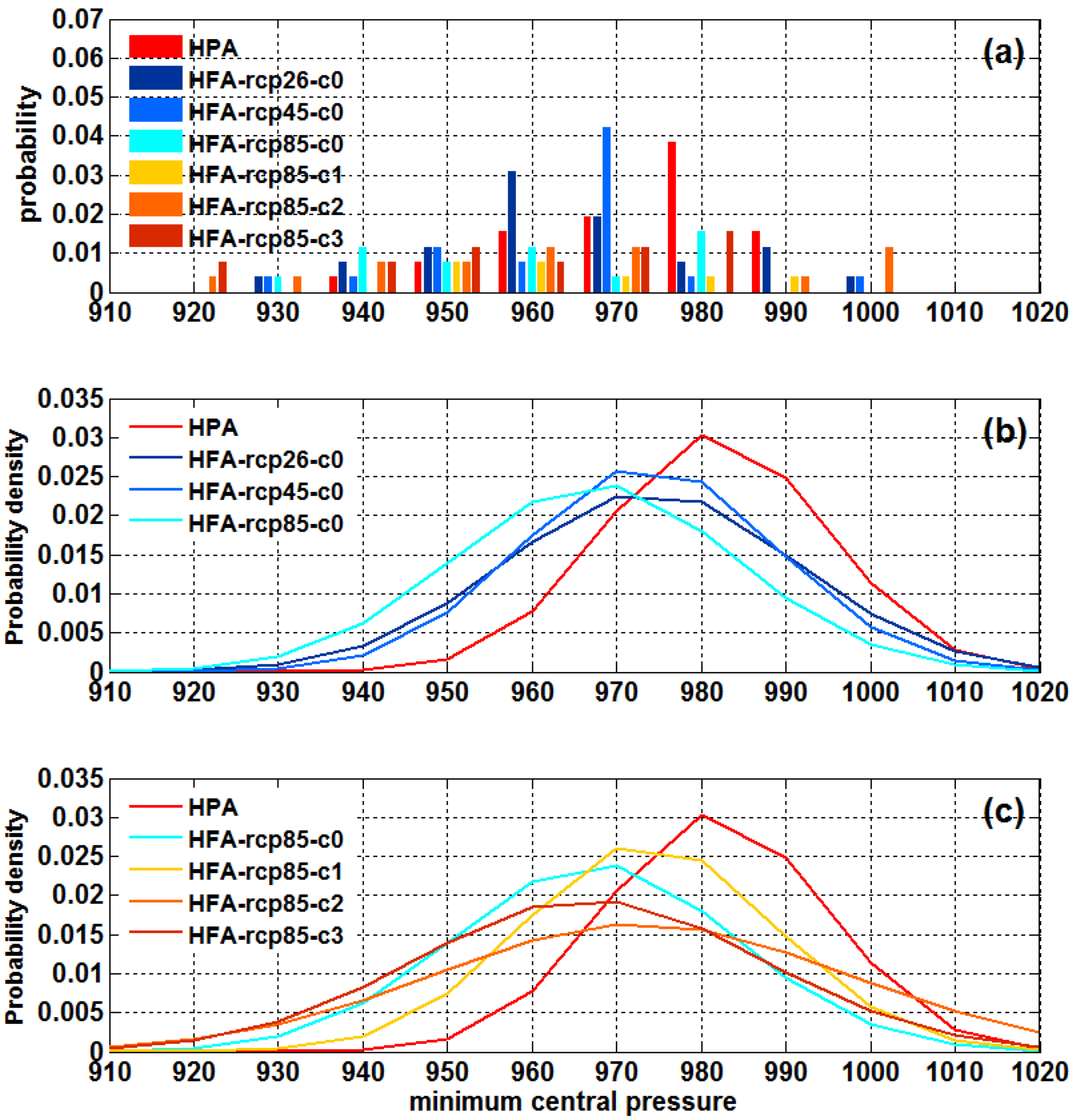

Figure 4.5 Probability of minimum central pressure of typhoons passing around the Korean Peninsula for (a) present and all future ensemble experiments and probability density functions of minimum central pressure of the typhoons for present and future ensemble experiments (b) with different global scenarios and (c) with different spatial pattern of SST using MRI-AGCM3.2H under present climate condition from 1984 to 2003 and under future climate condition from 2080 to 2099, respectively

Table 4.3 Characteristic values of observed and modeled typhoon properties by IBTrACS and MRI-AGCM3.2H

Climate condition	Abbreviation for source of typhoon data	The number of typhoons	Decreasing rate of the number of typhoons in the future climate [%]	Mean values of minimum central pressures [hPa]	Decreasing rate of the mean value of minimum central pressures in the future climate [%]
Present climate	Observation	74	-	981.6	-
Future climate	HPA	26	-	981.6	-
	HFA-rcp26-c0	25	4	974.0	0.8
	HFA-rcp45-c0	20	23	970.7	1.1
	HFA-rcp85-c0	14	46	968.6	1.3
	HFA-rcp85-c1	7	73	968.1	1.4
	HFA-rcp85-c2	16	38	969.1	1.3
	HFA-rcp85-c3	16	38	969.1	1.3

4.4 Assessment of uncertainties of projection of future storm surge heights around the Korean Peninsula

A series of storm surge simulations targeting the whole coast (D2) and southeastern coast (D4) in the KP were carried out using the typhoons around KP with the bias corrected values of the minimum central pressure from each ensemble experiment. For the maximum SSHs during the present and future climate, uncertainty caused by the choice of global warming scenario and spatial SST pattern were estimated.

Figure 4.6 shows the spatial distributions of projected maximum SSHs at each grid in D2 during present climate from 1979 to 2003 and future climate from 2075 to 2099, while Figure 4.7 presents future changes of the maximum SSH for each ensemble experiment. Under present climate, the maximum SSHs more than 2 m occur in the some areas of the west and south coast. On the other hand under future climate, the values of the maximum SSHs increase up to 7 m. Areas where SSHs the higher than 2 m occur and the extent of the areas vary substantially among the ensemble experiments. Amount of future change of SSHs ranges from -2.03 m to 5.52 m depending on the experiment condition. Figures 4.6 (b)-(d) and (g) compare the results from ensemble experiments using four SST patterns; named as HFA-rcp85-c1, HFA-rcp85-c2, HFA-rcp85-c3 and HFA-rcp85-c0. Vulnerable area to storm surge in future climate vary depending on selected SST patterns. The high SSHs more than 2 m are shown for the west part of south coast in HFA-rcp85-c1, with 2.6 m of the highest SSH. Most coast is exposed to the high SSHs in HFA-rcp85-c2 with 4.4 m of the highest SSH at the center part of west coast. The upper part and the most of the west coast are vulnerable in HFA-rcp85-c3 and HFA-rcp85-c0, respectively. The highest SSH for the two experiments are 3.26 m and 6.94 m, respectively. The spatial variations of the future change in maximum SSHs for ensemble experiments using different SST patterns are indicated in Figures 4.7 (a)-(c) and (f). In general, increasing tendencies appear at areas with the high SSHs, but decreasing tendencies appear at areas that did not for all the ensemble experiments. HFA-rcp85-c1 shows relatively smaller amount of increase and larger amount of decrease than the other experiments. Figure 4.3 shows that there are few typhoons that pass around the vulnerable areas in each experiment. In other words, SSH is more affected by the intensity and pathway than the frequency of the typhoons. These results indicate that the vulnerable area to future storm surge and the extent of future SSHs depend on the considered spatial pattern of SST.

Figures 4.6 (e)-(g) indicate the maximum SSHs from ensemble experiments using three global warming scenario; named as HFA-rcp26-c0, HFA-rcp45-c0 and HFA-rcp85-c0. The vulnerable area to future storm surge do not vary significantly depending on the selected global warming scenario, whereas the extent of SSHs differ. The results for all experiments showed that the west coast and some parts of the south coast are vulnerable. The highest SSHs in each experiments are 3.62m, 4.64m and 6.94m, respectively. The spatial variations of the future change of maximum SSHs are indicated in Figures 4.7 (d)-(f). They seem to be similar patterns but the scale of variation is different according to the global warming scenario. It is thought as the gas emission increases, the change of typhoon track is small but the typhoon intensity rise significantly (refer to Figure 4.5).

Figure 4.8 and Figure 4.9 indicate the spatial distributions of projected maximum SSHs at each grid in D4 for each ensemble experiment over present climate and future climate and the future changes of the maximum SSH, respectively. The higher SSHs more than 2 m only occur in the west part of the areas and the value of highest SSH is 2.83 m under present climate. On the other hand, the values of the potential highest SSHs increase up to 5.46 m under future climate. These values are larger than the values which get from the results of D2. This is thought to be obtain more accurate values because the spatial grid resolution of D4 with 760 m is clearer than one of D2 with 4,500 m. The location and the size of the areas where the higher SSHs than 2 m vary considerably depending on the experiment condition. The extent of future change of SSHs is from -2.25 m to 5.02 m for all experiments.

Figures 4.8 (b)-(d) and (g) and Figures 4.9 (a)-(c) and (f) shows the spatial distribution of maximum SSHs and the differences of the maximum SSHs between the present and future climate for each ensemble experiment using different SST patterns, respectively, indicating that vulnerable areas and the magnitude of SSHs to future storm surge are dependent of the chosen SST patterns. In HFA-rcp85-c1 and HFA-rcp85-c0, the west parts of southeastern coast are storm surge-prone areas, but the magnitude of highest SSH is different; 5.20 m and 3.16m, respectively. In HFA-rcp85-c2, some of west part and the center of southeastern coast are prone with 5.46 m as highest SSHs. In HFA-rcp85-c3, there is little change between areas. They indicate that the future changes of the maximum SSHs have a strong regional dependency. The worst SST pattern on the southeastern coast is HFA-rcp85-c2.

Figures 4.8 (e)-(g) and Figures 4.9 (d)-(f) present the spatial distribution of maximum SSHs and their future change for ensemble experiments using different global warming scenario, respectively. It can be seen that high impact hazard areas move to the western part of the southeastern coast. This tendency is similar to the trend of the future typhoon pathway (see Figure 4.5). On the other hand, the greatest amount of increase for each experiment are 2.22 m, 3.21 m and 2.14m. The worst global warming scenario is HFA-rcp45-c0.

Kim *et al.* (2014) conducted the projection of future SSHs around KP based on the output of single climate exchange experiment using MRI-AGCM3.2S. They suggested difference of the SSHs between present and future climate is more than 1 m along the southwest coast, while the difference is less than 0.5 m along the west coast. These results disagree with our findings, because the assumptions of future climate are not consistent between both; they used the output based on ensemble mean SSTs from the CMIP3 (Coupled Model Intercomparison Project phase 3, 2007) under

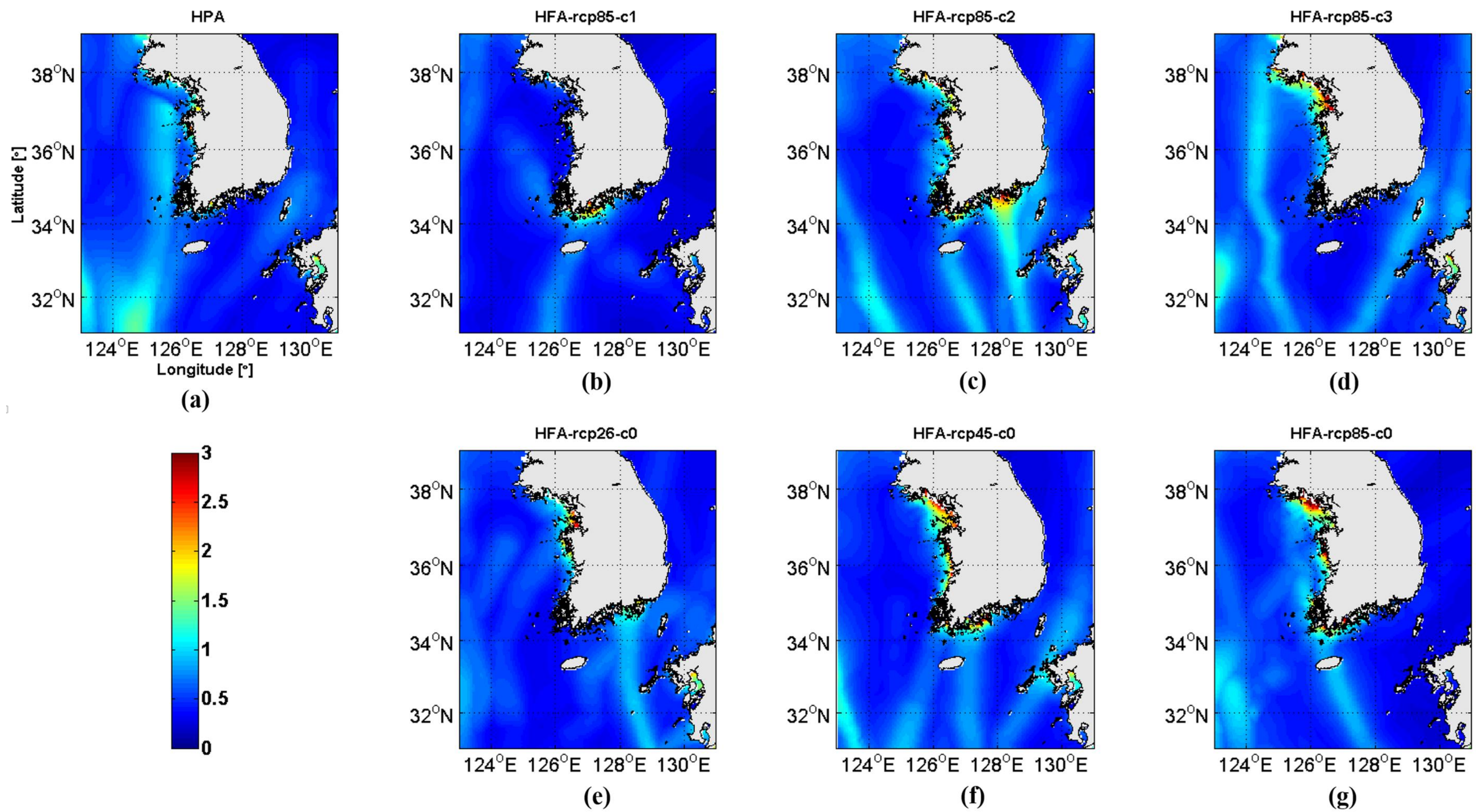

Figure 4.6 Projected maximum storm surge heights [unit : m] around the Korean Peninsula for ensemble experiments using MRI -AGCM3.2H (a) under the present climate condition (abbreviated as ñHPAò), (b) under the rcp8.5 scenario with Cluster 1 of CMIP5 SST (abbreviated as ñHFA-rcp85-c1ò), (c) HFA-rcp85-c2, (d) HFA-rcp85-c3, (e) under the rcp2.6 scenario with ensemble mean of CMIP5 SST experiments (abbreviatedas ñHFA-rcp26-c0ò), (f) HFA-rcp45-c0 and (g) HFA-rcp85-c0

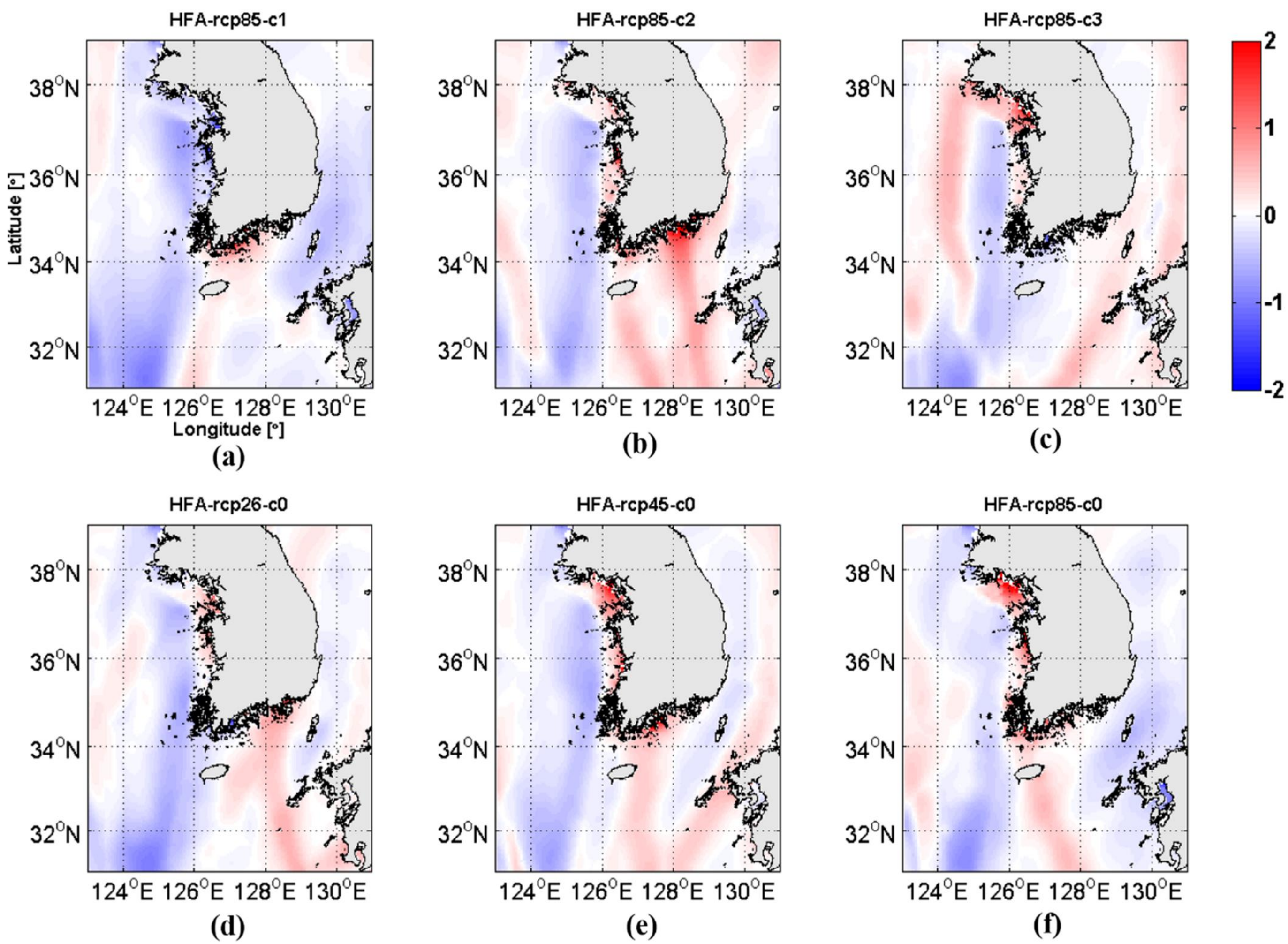

Figure 4.7 Differences of projected maximum storm surge heights [unit : m] around the Korean Peninsula between an experiment under the pr esent climate condition (abbreviated as ñHPAò) and an experiment (a) under the rcp8.5 scenario with Cluster 1 of CMIP5 SST (abbreviated as ñHFA-rcp85-c1ò), (b) HFA-rcp85-c2, (c) HFA-rcp85-c3, (d) under the rcp2.6 scenario with ensemble mean of CMIP5 SST experiments (abbreviated as ñHFA-rcp26-c0ò), (e) HFA-rcp45-c0 and (f) HFA-rcp85-c0. Warm/cold colors indicate increase/decrease in the future climate, respectively

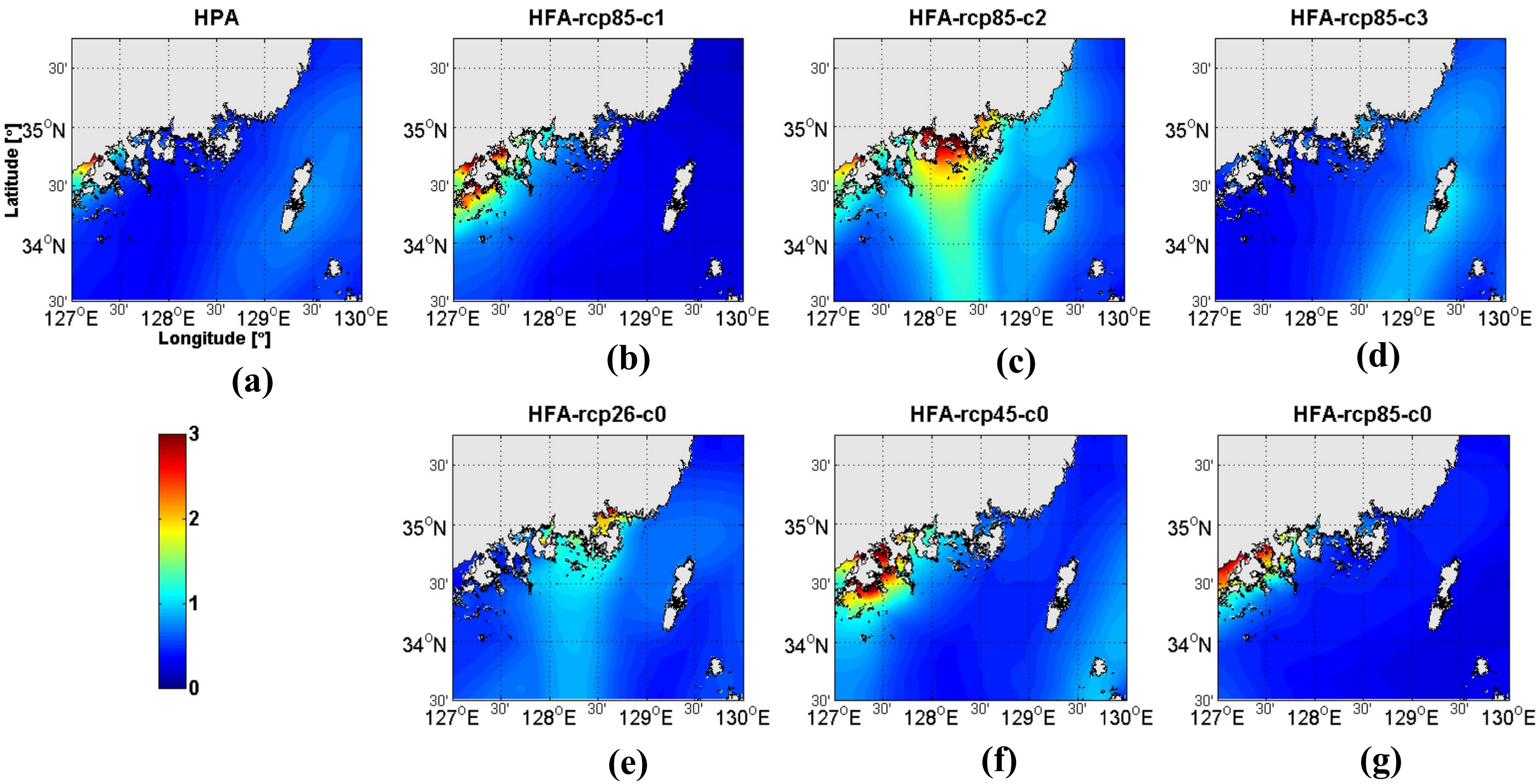

Figure 4.8 Projected spatial distributions of maximum storm surge heights [unit : m] around the southeastern coast of the Korean Peninsula for ensemble experiments using MRI -AGCM3.2H (a) under the present climate condition (abbreviated as ñHPAò), (b) under the rcp8.5 scenario with Cluster 1 of CMIP5 SST (abbreviated as ñHFA-rcp85-c1ò), (c) HFA-rcp85-c2, (d) HFA-rcp85-c3, (e) under the rcp2.6 scenario with ensemble mean of CMIP5 SST experiments (abbreviated as ñHFA-rcp26-c0ò), (f) HFA-rcp45-c0 and (g) HFA-rcp85-c0

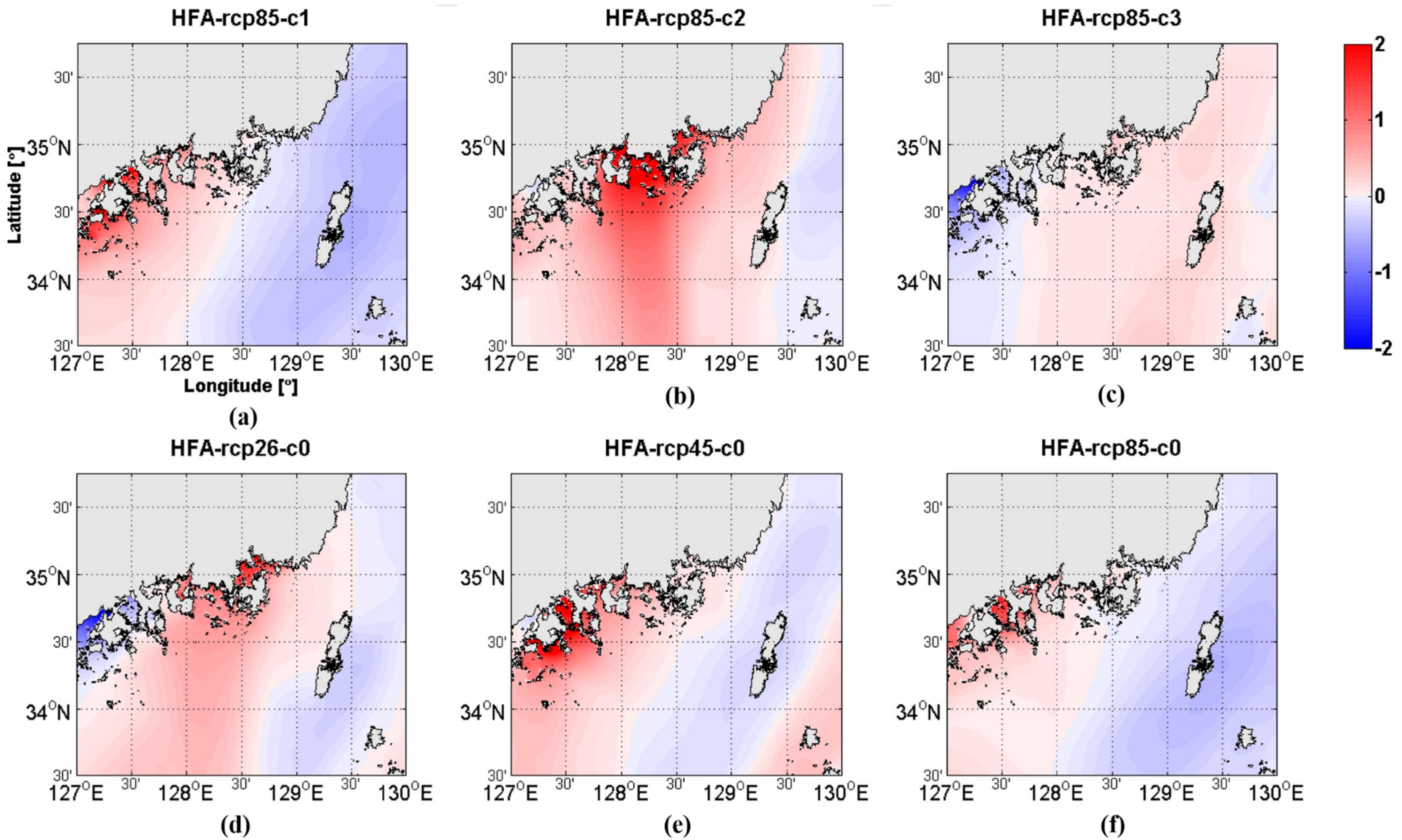

Figure 4.9 Differences of maximum storm surge heights [unit : m] around the southeastern coast of the Korean Peninsula between an experiment under the present climate condition (abbreviated as ñHPAò) and an experiment (a) under the rcp8.5 scenario with Cluster 1 of CMIP5 SST (abbreviated as ñHFA-rcp8-c1ò), (c) HFA-rcp85-c2, (d) HFA-rcp85-c3, (e) under the rcp2.6 scenario with ensemble mean of CMIP5 SST experiments (abbreviated as ñHFA-rcp26-c0ò), (f) HFA-rcp45-c0 and (g) HFA-rcp85-c0. Warm/cold colors indicate increase/decrease in the future climate, respectively

SRES A1B. From these results, it is indicate that the vulnerable area to future storm surge and the extent of future SSHs highly depend on the spatial pattern of SST (i.e. ocean climate) and the global warming scenarios. Moreover, SSH is more affected by the intensity and pathway than the frequency of the typhoons.

4.5 Summary

This chapter discussed the uncertainties of the projection of the typhoon properties such as the number, tracks and intensities and the storm surge heights under present and future climate conditions based on projected typhoons by ensemble experiments with three global warming scenarios and four spatial pattern of sea surface temperatures (SST) using MRI-AGCM3.2H.

The reproducibility of the typhoon data under present climate was estimated by comparison with observed typhoon data were discussed. Here, we focused the typhoons affecting around the Korean Peninsula (hereafter, typhoons around KP) which are pass through the region of 32° ~ 40°N and 122° ~ 132°E. The number of typhoons around KP was underestimated comparing to the observations, while the general trend of the tracks of them corresponded with the observations. Also the mean value of the minimum central pressure of them is smaller than observations by 8.8 hPa. Since this difference cannot be ignored in projecting future storm surge heights, the value of minimum central pressure from all ensemble experiments were linearly calibrated. The typhoons around KP with the corrected values were used to project future storm surges.

Future changes and uncertainties of typhoons properties under future climate were discussed by comparing the typhoon data from each ensemble experiments. The number and intensity of the typhoons around KP were expected to decrease and the locations of typhoon genesis and typhoon lysis were projected to shift to the northwest for all ensemble experiment. However, the extent of each change is anticipated to vary depending on global warming scenario and the conditions of SST pattern.

A series of storm surge simulations for the coast in the KP were conducted by using the corrected the typhoons around KP data from each ensemble experiment. The vulnerable area to future storm surge and the extent of future SSHs depend on the spatial pattern of SST and the global warming scenario. Moreover, SSH is more affected by the intensity and pathway than the frequency of the typhoons. But the present study have uncertainties of projection of future typhoons and SSHs and cannot estimate storm surge values with particular return periods which required in coastal structure design because of the lack of SSH samples. The additional ensemble experiments is needed to obtain a large number of the samples and to reduce the uncertainties.

Chapter 5.
Projection of Future Storm Surges based on Mega Ensemble Experiments using Single Atmospheric Global Climate Model

5.1 Introduction

Severe tropical cyclone characteristics resulting from global climate change are expected to change future storm surge heights (hereafter, SSHs) depending on ocean basins and regions (e.g. Mori and Takemi, 2016). Projection of future SSHs based on results of ensemble climate experiments performed using a general climate model (hereafter, GCM) under future climate conditions is ready to start at the regional scale for disaster prevention against storm surge (e.g. Woth *et al.*, 2006; Wang *et al.*, 2008; Kim *et al.*, 2014; Yasuda *et al.*, 2014; Vousdoukas *et al.*, 2016). However, there are some uncertainties which become larger as the spatial scale of interest becomes small. The uncertainties are mainly caused by differences in pathways of global warming scenarios, climate models and internal variability. Of the three factors, the first two are estimated by the fifth phase of the Coupled Modeling Intercomparison Project (CMIP5) experiments. However, there has been little research on the internal variability such as decadal variations in the ocean, inter-annual variability in the extratropical atmosphere and intra-seasonal variation in the tropics which is considered as one of the important factors for less frequent anomalous climate extreme (Deser *et al.*, 2012; Kay *et al.*, 2015).

In the previous Chapter 4, it was investigated how the multi-global warming scenarios and multi-patterns of sea surface temperature (hereafter, SST) obtained from different GCMs influence on typhoon properties and storm surge height (hereafter, SSH) on regional scale targeting the Korean Peninsula using the outputs of six ensemble experiments by the single GCM. First, it was confirmed that the number of strong typhoons were expected to increase and the locations of typhoon genesis and typhoon lysis were projected to shift to the northwest for all ensemble experiments. However, the extent of each change is anticipated to vary depending on global warming scenarios and the SST patterns. In addition, the vulnerable area to future storm surge and the extent of future SSHs depend on the SST pattern and the global warming scenario. Moreover, the extreme SSH is more affected by the intensity and tracks than the frequency of the typhoons. However, this study cannot estimate SSHs with particular return periods which required in coastal structure design because of the lack of enough samples of storm surge events around the Korean Peninsula.

To evaluate the uncertainty resulting from the internal variability and to obtain a large number of samples in localized rare events, Mizuta *et al.* (2016) carried out an unprecedentedly large ensemble of climate simulations using a high-resolution climate model. From the output of such mega ensemble simulations, probabilistic future changes in extreme events with low-frequency on local scales can be estimated directly without application of statistical models such as the generalized extreme value distributions.

The research methodology in this chapter is similar to that of Chapter 4 but changing forcing of future climate conditions. Projected typhoon activities affecting the Korean Peninsula (hereafter, typhoons around KP) which pass through the region of 32°-40°N and 122°-132°E and SSHs along the KP under future climate are considered. But, in this chapter, typhoon data extracted from the output of the mega ensemble experiments under past and future climate conditions (Mizuta *et al.*, 2016) was used. First, the reproducibility of the typhoon data is estimated by comparison with observed typhoon data, and future changes of properties of the typhoon data such as genesis number, track and intensity are discussed. In addition, a series of storm surge simulations around the KP are conducted by using the typhoon data. Storm surge values with particular return period, namely once every 100-year, 500-

year or 1,000-year, are assessed on regional scale and on specific points. The remainder of this chapter is organized as follows. Section 5.2 briefly introduces mega ensemble experiments used in this study. Section 5.3 discusses characteristics of typhoons around KP under present and future climates. Section 5.4 projects the future SSH with specific return periods around the KP. Section 5.5 provides a summary of this chapter. Typhoon detection method and storm surge simulation conditions are the same as in sections 4.2.2 and 4.2.3, respectively, so no description will be given in this chapter.

5.2 Outline of mega ensemble climate experiments

Mizuta *et al.* (2016) carried out an unprecedentedly large ensemble experiments of climate simulation using a global atmospheric model of the Meteorological Research Institute with a 60 km horizontal resolution (hereafter, MRI-AGCM3.2H; Mizuta *et al.*, 2012) which is the same AGCM in the chapter 4. Three types of experiments were conducted: a historical climate simulation, a future climate simulation and a non-warming climate simulation. For each climate experiment, sea surface temperature (SST), sea-ice concentration (SIC) and sea-ice thickness (SIT) were employed as the lower boundary conditions and concentrations of greenhouse gases (CO_2, CH_4, N_2O, and CFCs), ozone and aerosols were set as the external forcing. Settings for each climate experiment are summarized in Table 5.1.

The historical climate experiment from 1951 to 2010 was simulated with 100 ensemble members for which the lower boundary conditions and those initial conditions were perturbed. The observed monthly-mean SST and SIC (COBE-SST2; Hirahara *et al.*, 2014) and climatological monthly SIT (Bourke and Garrett, 1987) were used as the lower boundary conditions. Small perturbations of the SST (ŭSSTs) based on the SST analysis error were added to the COBE-SST2 to produce different initial conditions. Concentrations of greenhouse gases are set to the observed global-mean values for each experimental year. Three-dimensional distributions of ozone from the Chemistry-Climate Model of MRI (Deushi and Shibata, 2011) and aerosols from the coupled global climate model of MRI-CGCM (Yukimoto *et al.*, 2012) were used.

The future climate experiment from 2051 to 2110 was conducted with 90 ensemble members, assuming the global-mean surface air temperature becomes 4 K warmer than the pre-industrial climate as explained in the following paragraphs. The amplitude of the global warming corresponded to that of the end of the 21th century under the Representative Concentration Pathway 8.5 (RCP 8.5) scenario of CMIP5 and was held constant over the experimental period. By doing this, large samples under the same specified circumstance of global warming can be obtained. As for the boundary conditions, climatological SST warming patterns (ΔSSTs) were added to the observational SST after removing the long-term trend component. The ΔSSTs were selected by a cluster analysis of geographical patterns of SST changes based on six models among CMIP5 models (Mizuta *et al.*, 2014). Each pattern was multiplied by a scaling factor to get a global mean surface air temperature warming of 4 K. The six models and corresponding scale factors were presented in Table 5.2. Adjusted SIC and SIT were taken to match the SST in the future climate condition. To make different initial conditions for each ensemble member, 15-member ensemble experiments using different ǔSSTs of the historical simulation were conducted with each of the six ΔSSTs. The greenhouse gases were assigned the values in the year 2090 of the RCP 8.5 scenario. The ozone and aerosol distributions were chosen to be the average from 2088 to 2092 in the extended experiments with the same models as used in the historical simulation.

The non-warming climate experiments from 1951 to 2010 were carried out with 100 ensemble members, assuming that global warming had not occurred since the pre-industrial climate. By comparing this experiment with the past climate experiment, it is possible to discuss climate change trends resulting from past external forcing factors. In this experiment, the boundary conditions were given with the long-term trends removed, and the boundary and initial perturbations for the ensemble members were the same as those of the historical simulation. For external forcing, the value of greenhouse gases in 1850 was applied. The ozone was fixed to an average value between the years 1960 and 1962 from the historical simulation. The value of aerosols was obtained from an experiment using the values of sulfate, black carbon and organic carbon emissions in the pre-industrial climate and the same value of mineral dust and sea-salt as in the historical simulation.

Outputs of each simulation are available to the public in a database called the ñDatabase for Policy Decision-Making for Future Climate Change (d4PDF)ò. The d4PDF aims to be utilized for impact assessment of hazards and adaptation planning for global warming. This study used the outputs from past and future climate experiments using MRI-AGCM3.2H. Hereafter, each output will be abbreviated as $d4PDF_{past}$ and $d4PDF_{future}$, respectively. Typhoon data extracted from the outputs were employed as external forcing for storm surge simulation around the KP.

Table 5.1 Settings for each climate experiment

		Historical simulation	Future simulation (+4K warming)	Non-warming simulation
Climate experimental period		From 1951 to 2010 (60 years)	From 2051 to 2110 (60 years)	From 1951 to 2010 (60 years)
Ensemble members	AGCM	100	90	100
	NHRCM	50	90	N/A
Low boundary condition	SST	observed	observed SST + climatological SST warming patterns (ΔSSTs)	observed with long-term trends removed
	SIC	COBE-SST2 (Hirahara *et al.*, 2014)	adjusted one to match future SST	adjusted one to match SST
	SIT	climatological monthly SIT (Bourke and Garrett, 1987)	adjusted one to match future SST	adjusted one to match SST
External forcing	Greenhouse gases	observed	values at 2090 under RCP 8.5	values at 1850
	Ozone	monthly output form MRI-CCM (Deushi and Shibata, 2011)	2090 output form MRI-CCM	1961 output from MRI-CCM
	Aerosols	monthly output from MRI-CGCM (Yukimoto *et al.*, 2012)	2090 output from MRI-CGCM	sulfate, black carbon and organic carbon: values at pre-industrial, mineral dust and sea-salt: same as historical

Table 5.2 CMIP5 models used for obtaining climatological SST warming patterns and the corresponding scaling factor for each model

Model	Scaling Factor	Institution	Country
CCSM4	1.10981	National Center for Atmospheric Research	USA
GFDL-CM3	0.75166	NOAA Geophysical Fluid Dynamics Laboratory	USA
HadGEM2-AO	0.90222	Met Office Hadley Centre	UK
MIROC5	1.06162	AORI, NIES, JAMSTEC	Japan
MPI-ESM-MR	1.01852	Max Planck Institute for Meteorology	Germany
MRI-CGCM3	1.13509	Meteorological Research Institute	Japan

5.3 The typhoon characteristics affecting the Korean Peninsula and its validation

Typhoon Characteristics like the number, track and minimum central pressure were examined by comparing the typhoon data from the $d4PDF_{past}$ with those of the observed typhoon dataset (IBTrACS; Knapp *et al.*, 2010). Moreover, its future change were assessed by comparing typhoon data of the $d4PDF_{past}$ and the $d4PDF_{future}$.

5.3.1 The number

The first its reproducibility of typhoons around KP in the past climate and its future change were evaluated. Figure 5.1 shows probability of annual numbers of typhoons around KP under the past and the future climate conditions. The total numbers of typhoons around KP under the past climate conditions are 214 (#3.56/year) and 6,475 (#1.08/year/member) for IBTrACS and $d4PDF_{past}$, respectively. Results for the $d4PDF_{past}$ underestimate the number of typhoons around KP. Note that the TC detection method applied in this study is calibrated to match the observed annual cyclogenesis global number. Although the annual number of cyclogenesis is similar in the global zone including the Western North Pacific basin (Murakami *et al.*, 2012), the annual TC number around typhoons is underestimated due to weaker TCs by MRI-AGCM3.2H. However, we mainly take care of extreme TCs, the weak TCs are not important for analysis.

The total number of typhoons around KP under the future climate condition is 3,632 (#0.67 per year per a member) while under the past climate condition it is 6,475 (#1.08/year/member). It was found that the numbers of typhoons approaching the KP are significantly reduced in the future climate condition by 38%. This value is the same as the results with Cluster 2 and Cluster 3 of CMIP SST under RCP8.5 scenario using the same MRI-AGCM3.2H in section 4.3.2.

The mega-ensemble experiment produced large samples of storm surge event under past and future climates. That makes it possible to evaluate rare SSH event with a return period more than several decades for the design of coastal disaster prevention structure

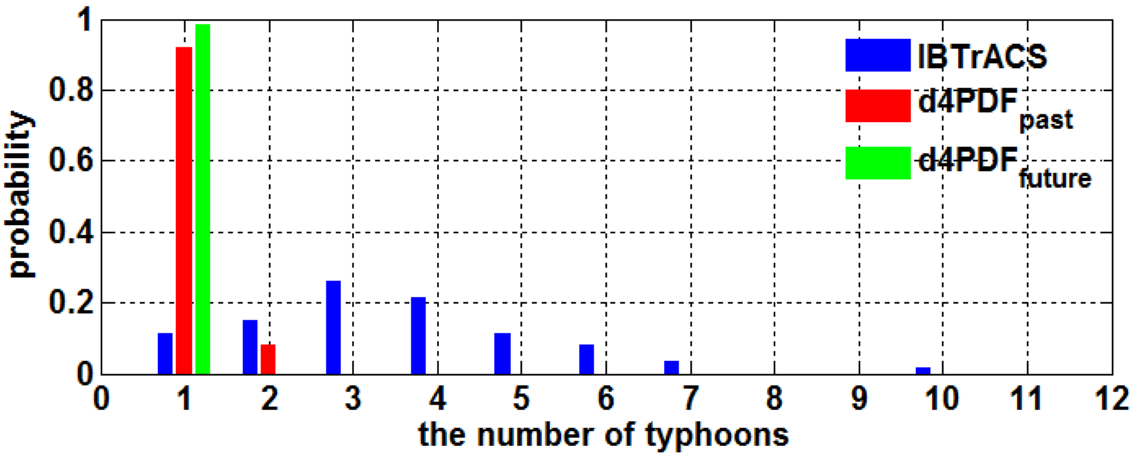

Figure 5.1 Probability of annual number of typhoons passing around the Korean Peninsula. (a) observations (IBTrACS) from 1961 to 2010, (b) ensemble member mean of simulation under past climate condition ($d4PDF_{past}$) from 1961 to 2010 and (c) ensemble member mean of projection under future climate condition ($d4PDF_{future}$) from 2061 to 2110

5.3.2 Tracks

Next, the characteristic of the typhoon tracks was assessed. Figure 5.2 expresses the typhoon tracks as annual mean ratio of the number of typhoons in each grid. The reproducibility of the typhoon tracks from $d4PDF_{past}$ was analyzed based on Figures 5.2 (a) and (b). Typhoons from both which generated in the area of 5°-20°N and 113°-170°E go west in the South China Sea and change their path to the northeast toward the KP near Taiwan. Afterward, they approach the western and southern coasts of the KP. The overall tendency of the typhoons tracks from $d4PDF_{past}$ reproduces one from IBTrACS well. Besides the continuous distribution of typhoon movement by gird was obtained by virtue of abundance of typhoon data of $d4PDF_{past}$.

Future change of typhoon tracks was evaluated based on Figures 5.2 (b) and (c). The general typhoon tracks including the locations of typhoon genesis and lysis are projected to shift to the northwest. The typhoons change their trajectory to the northeast near Shanghai which is north of Taiwan. Figure 5.2 (d) shows the difference in the number of typhoon passing through each grid. Under the future climate the number of typhoons around KP is expected to decrease while the number of typhoons which pass through the regions above 40°N and the left of 120°E is anticipated to decrease. These characteristics of future TC track shift is similar to Mori and Takemi (2016), although

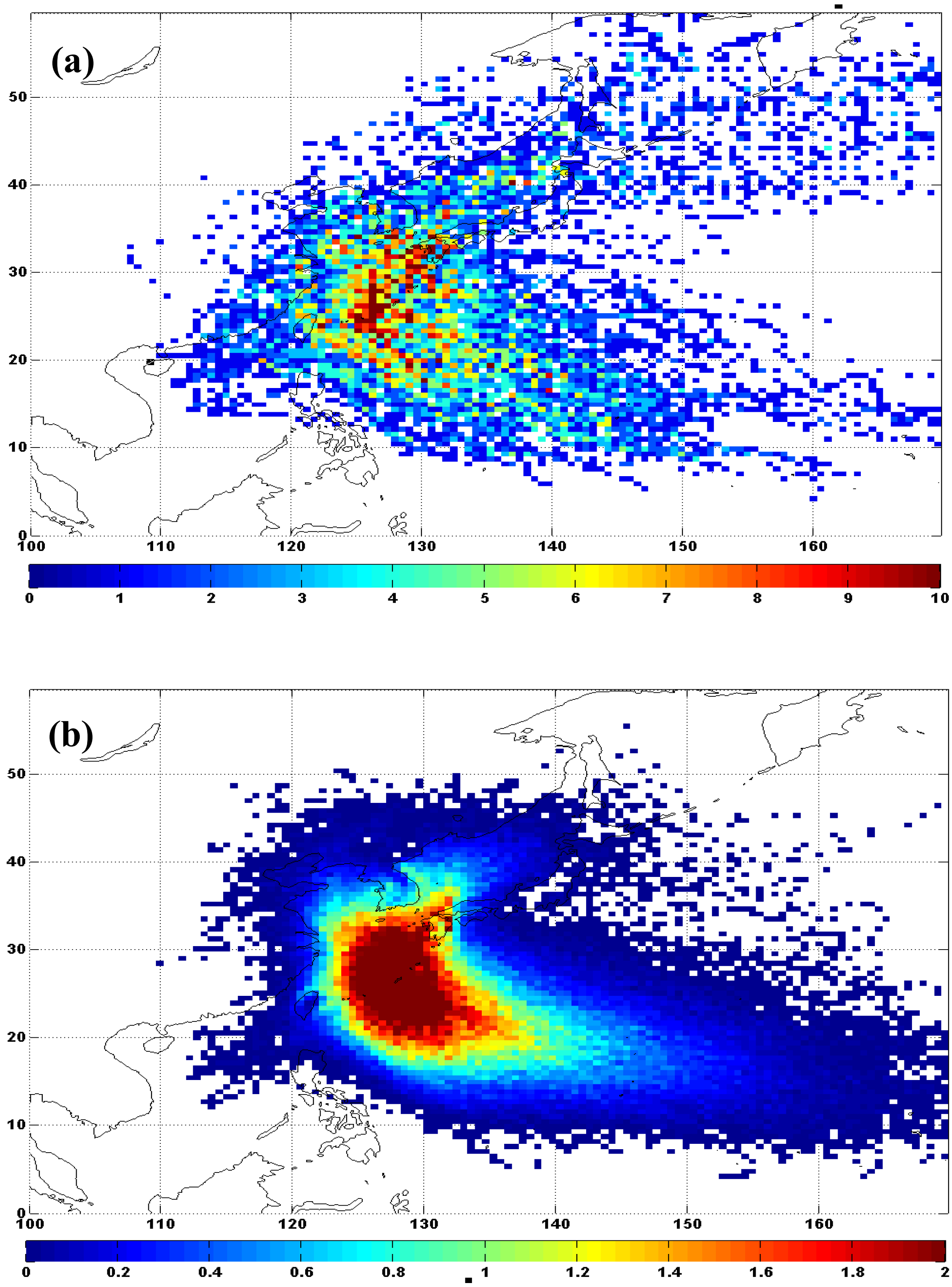

Figure 5.2 Annual number of typhoons affecting the Korean Peninsula passing through each grid. (a) observations (IBTrACS), (b) ensemble member mean of simulation under past climate condition ($d4PDF_{past}$), (c) ensemble member mean of projection under future climate condition ($d4PDF_{future}$) and (d) future change between $d4PDF_{past}$ and $d4PDF_{future}$. Blue and red colors in legend of (d) mean the decrease and increase, respectively

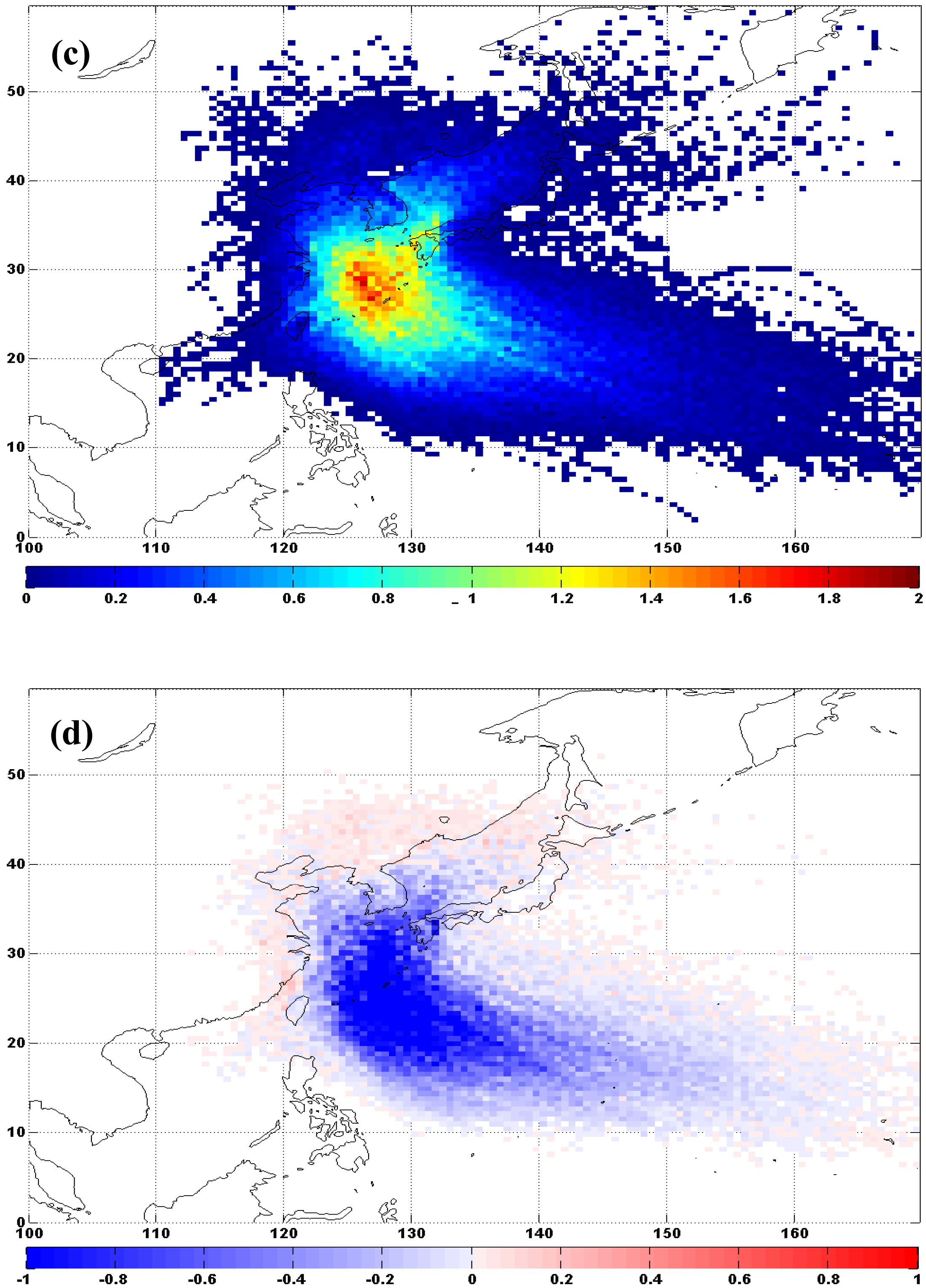

Figure 5.2 Annual number of typhoons affecting the Korean Peninsula passing through each grid. (a) observations (IBTrACS), (b) ensemble member mean of simulation under past climate condition ($d4PDF_{past}$), (c) ensemble member mean of projection under future climate condition ($d4PDF_{future}$) and (d) future change between $d4PDF_{past}$ and $d4PDF_{future}$. Blue and red colors in legend of (d) mean the decrease and increase, respectively

the given scenario is different.

5.3.3 Minimum central pressures

Finally, the feature of minimum central pressures of the typhoons were analyzed. Figure 5.3 indicates the probability and probability density function of minimum central pressure of the typhoons. Mean values of the minimum central pressure are 981.7 hPa and 971.35 hPa for IBTrACS and $d4PDF_{past}$, respectively (see Figure 5.3 (d)). The difference between both is about 10.35 hPa. The mean value of $d4PDF_{past}$ is smaller than 10.35 hPa. Mori and Takemi (2016) indicated MRI-AGCM3.2H tends to have a lower central air pressure due to the weak representation of wall cloud. In fact, the results of ensemble experiments using same GCM model used in Chapter 4 showed similar results. However, this difference cannot be neglected in projecting storm surge simulation. To examine whether two data sets of the minimum central pressure of the typhoons between IBTrACS and $d4PDF_{past}$ come from populations with a common distribution, the quantile-quantile (q-q-) plot of those and a 45 degree reference line are shown in Figure 5.4. Before the calibration of values of the minimum central pressure from $d4PDF_{past}$, points representing the relationship of the minimum central pressure between two data sets are in a straight line above the 45 degree reference line. That means the two data sets come from populations whose distributions differ only by a shift in location. So, the values of minimum central values from $d4PDF_{past}$ and $d4PDF_{future}$ were linearly calibrated. After the calibration of the values, the points are approximately on the reference line. In other words, the probability distribution for $d4PDF_{past}$ is in good agreement to one of IBTrACS.

Mean values of the minimum central pressure for $d4PDF_{past}$ after the bias correction and $d4PDF_{future}$ are 981.70 hPa and 973.54 hPa (refer to Figure 5.3 (d)), respectively. Future change in the mean values is about 8.16 hPa. Typhoons under the future climate are stronger than ones under the past climate. Furthermore, significant future change of the minimum central pressure is evident when intense typhoons whose pressures are smaller than 940 hPa.

From the discussion, under present climate condition, the number of typhoons around KP was underestimated comparing to the observations, while the general trend of the tracks of them was consistent with one of the observations. Also the mean value of the minimum central pressure of them is smaller than observations by 10.35 hPa. Since this difference cannot be neglected in projecting future SSHs, the mean values for d4PDF were linearly calibrated. The bias corrected values will be used to project future storm surges. Under future climate condition, the number and intensity of the typhoons around KP are anticipated to decrease and the general typhoon track were projected to shift to the northwest. Subsection 5.4 projects the future SSHs with specific return periods around the KP and particular points in the KP.

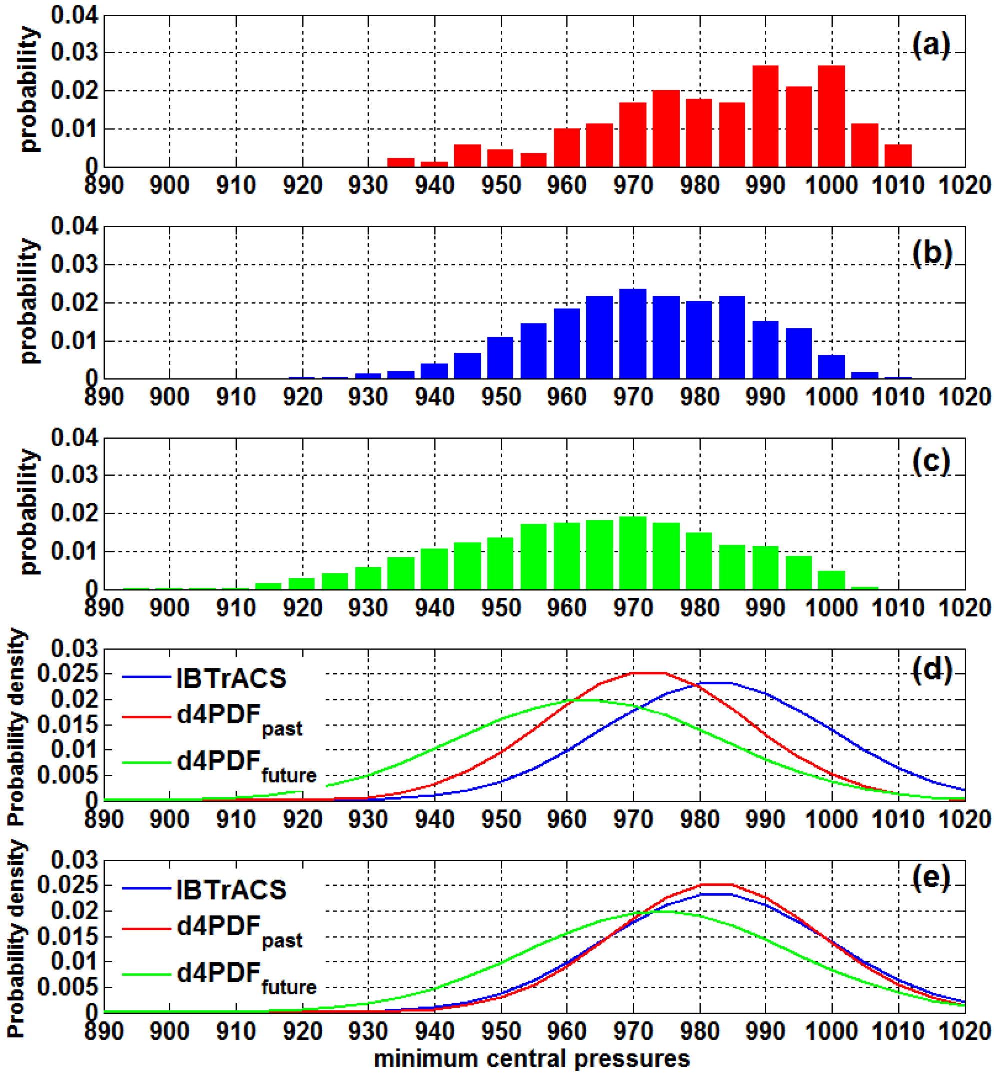

Figure 5.3 Probability of minimum central pressure of typhoons affecting the Korean Peninsula: (a) observations (IBTrACS), (b) mega ensemble simulation under past climate condition (d4PDFpast), (c) mega ensemble projection under future climate condition (d4PDFfuture). Probability density function of (d) without the correction of bias between IBTrACS and $d4PDF_{past}$ and (e) with correction of the bias

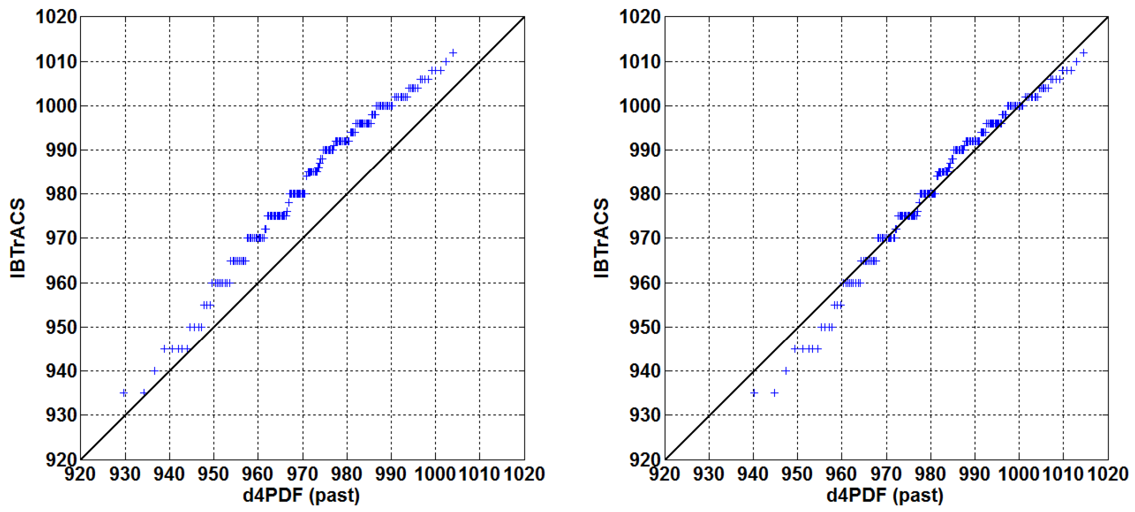

Figure 5.4 The quantile-quantile (q-q) plots of the minimum central pressure for between observations (IBTrACS) and mega ensemble simulation ($d4PDF_{past}$): (left) without the correction of bias between IBTrACS and $d4PDF_{past}$ and (right) with correction of the bias

5.4 Projection of future storm surge heights

A series of storm surge simulations were conducted using strong typhoon data with the minimum center pressure of 970hPa or less after the calibration of that for reason of computational expense. The number of the typhoon was 1,428 in the past climate and 1,522 in the future climate which correspond to 6,000 years and 5,400 years of data, respectively. Maximum SSHs on each grid for every typhoon event from the simulation results were used as maximum value data for extreme value statistical analysis to evaluate the future storm surge risk to the KP.

Generally, when estimating probability value of SSH with the particular return period, extreme value distributions such as Gumbel, Fréchet or Weibull distributions are employed to extrapolate the probability value because of the small number of the maximum value data for evaluation. However, in this study, the probability value were calculated directly from order statistics of the maximum SSHs without using any extreme value distributions. The return period of R-year of an extreme storm surge event is calculated as following:

$$R = \frac{1}{\lambda(1-P)} \tag{5.18}$$

where λ is an annual average incidence of events and P is a cumulative probability which is estimated using plotting position formulae. For the plotting position, in this study, Weibull formula (Weibull, 1939) in Equation (5.2) were employed following the recommendations of Makkonen (2006).

$$P = \frac{m}{N+1} \tag{5.19}$$

where P is the cumulative probability associated m^{th} smallest value of the maximum SSHs data, m is the rank of the value of the maximum SSHs which has a value of 1 for the largest value and N is the total number of the maximum SSHs. SSH with 100-year return period under the past and the future climates is assessed on regional scale (D2, D4 in Figure 5.5 (left)) and on specific points in D4 (refer to Figure 5.5 (right)).

First, the extreme SSHs along the KP are estimated by above mentioned nonparametric method. Figure 5.6 shows spatial distributions of the SSHs in the 100-year return period under the past and future climates and future change of the SSH. Under the past climate, high SSHs are distributed in the center areas of the western region and the southern region in the KP. On the other hand, the locations of the vulnerable area to storm surge shift to the north area of the western region where the capital area including Seoul is located and to the west area of the southern regions in the KP under the future climate. This characteristic of future change to area where high SSHs occur coincide with one to typhoon track shift. SSH around the KP is projected to increase under the future climate except for some areas in the south coast. The magnitude of future change of SSH vary spatially. Yasuda *et al.* (2014) conducted the projection of future SSHs in East Asia including the KP based on the output using MRI-AGCM3.2S with ensemble mean SSTs from the CMIP3 (Coupled Model Intercomparison Project phase 3, 2007) under SRES A1B. They reported that SSHs around the KP under the future climate would increase along the south coast and decrease along the west coast, being in disagreement with our findings. They used similar scenario based projections by the same AGCM but the period of projections are 25 years time-slice both the past and future. Therefore there are small number of extreme TCs at particular locations, although they examined the extreme value analysis for 100-years return events by 25-years

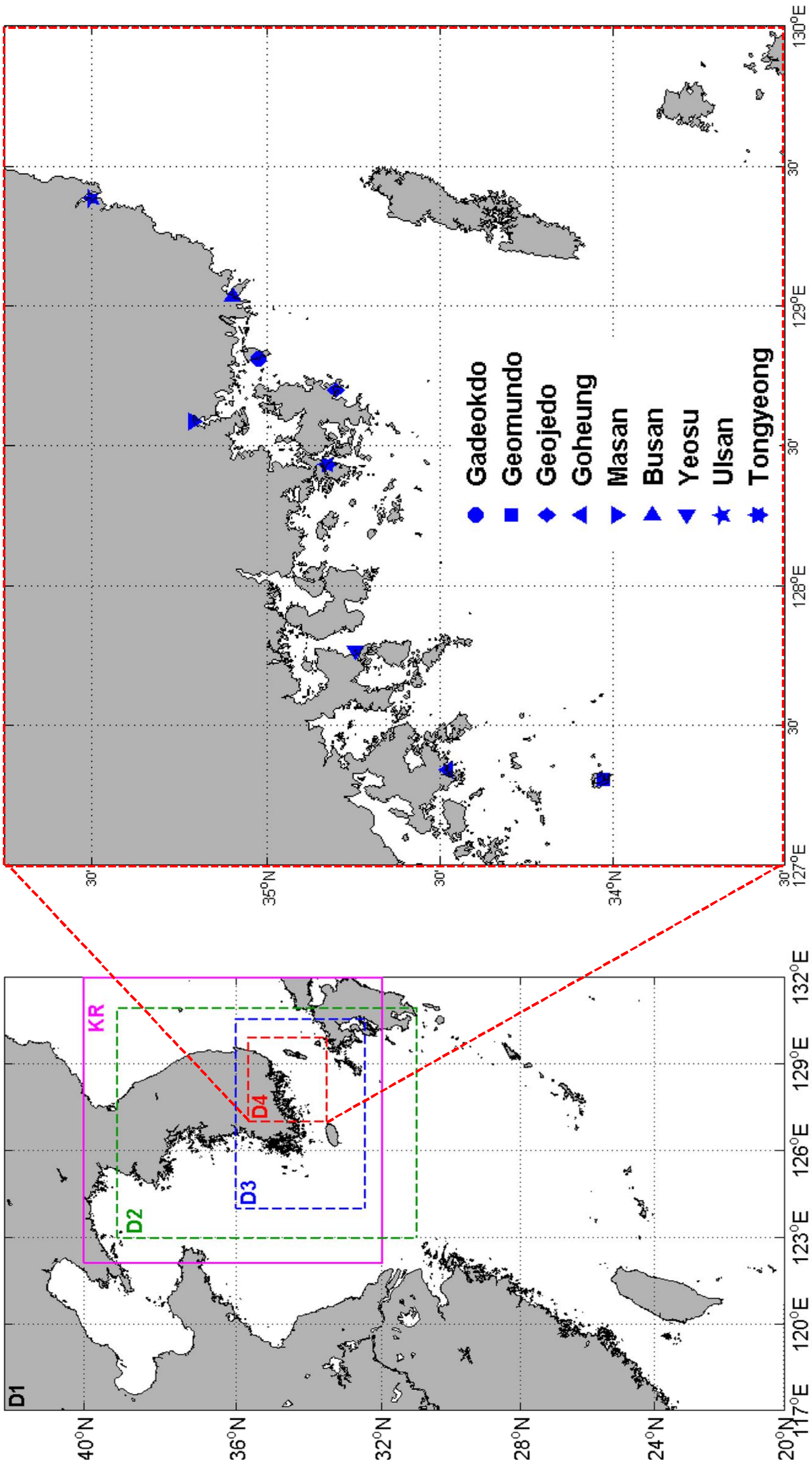

Figure 5. 5 Calculation domains for storm surge projections (abbreviated as ñD#ò, # is the number of domain) (left) and tidal observation stations in D4 (right)

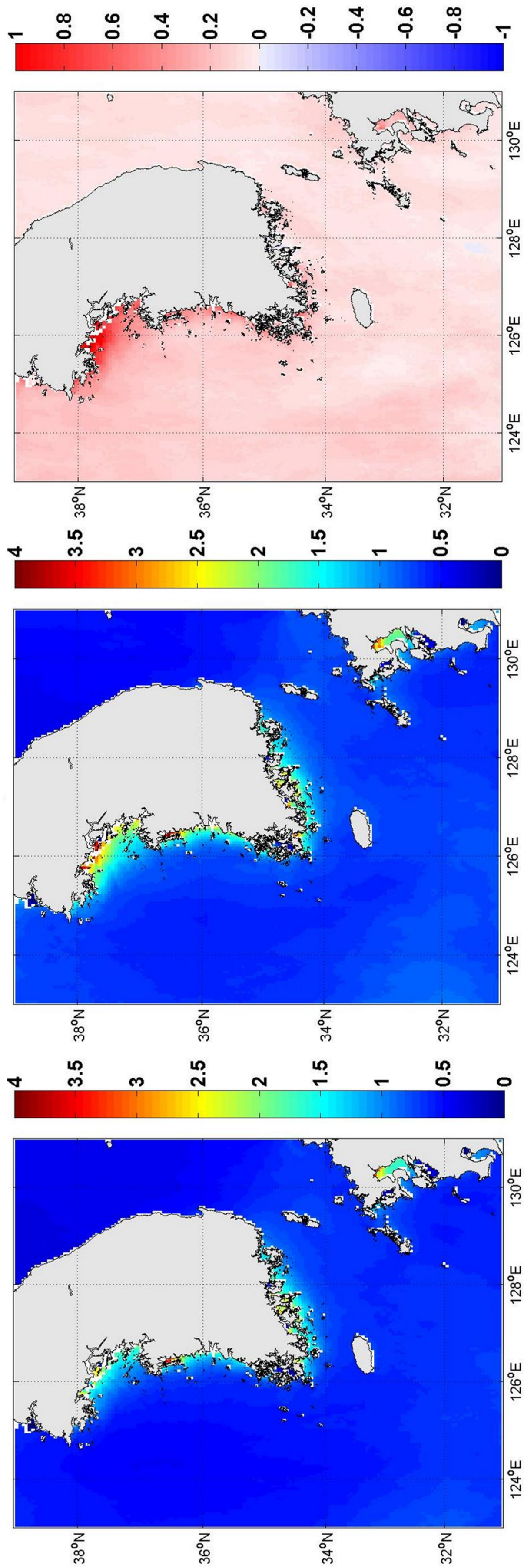

(a) past climate

(b) future climate

(c) future change

Figure 5.6 Spatial distributions of storm surge heights (m) along the Korean Peninsula (D2) with 100-year return period. (a) past climate and (b) future climate and (c) future change projections. Only few typhoons have reached the KP by 25-years time-slice experiments. Although mean value of minimum central pressure of typhoons extracted from the output was underestimated than one of observation typhoon dataset, they used the typhoons without correction of values of the minimum central pressure. For such a reason as mentioned, disagreement between our and their findings resulted from the number of ensemble experiments, reproducibility of typhoons and calibration of minimum center pressure of typhoons.

Next, the results for the southeastern area of the KP are discussed based on finer scale nesting domain. Figure 5.7 presents spatial distributions of SSH with 100-year return period under the past and future climates and future change of the SSH. From Figure 5.7 (a), it can be seen that the high SSHs take place in the west and center area and most severe SSH occurs a bay (marked with ñAò in the Figure) with 3.57 m. The most areas of the west will be projected to vulnerable to storm surge under the future climate as described in Figure 5.7 (b). Value of the highest SSH is estimated at 4.12 m the bay. As shown in Figure 5.7 (c), the SSH for overall areas increase under the future climate compared with those under the past climate except for some areas ranging between 127.7ºE-128 ºE and 34.6ºN-35 ºN. Pronounced increase of the SSH will be projected to take place in the west and center areas of the southeastern coast of the KP. The maximum variation is estimated to 0.61 m (15.4 %) in the bay. This future change may be due to the increase in the number of strong typhoons affecting the KP and the change of typhoon tracks resulting from climate change. Storm surge risk around the KP in the future is expected to increase but the extent of that sensitively vary by location. Figure 5.8 shows spatial distributions of SSH with 500-year return period under the past and future climates and future change of the SSH. The spatial patterns are similar to those with 100-year return period, but the value of SSHs increase around the coast. It is expected that the highest SSH take place a bay (marked with ñBò in the Figure 5.8 (a) and (b)) with 4.74 m and 5.40 m under past and future climates, respectively. The variation is estimated to 0.89 m (13.9 %) in the bay. As the return period of SSH became longer from 100 to 500, the most vulnerable area tends to move to the east. As shown in Figure 5.8 (c), the future change of SSH is projected to increase throughout overall areas except for some area ranging between 128ºE-128.3 ºE and 34.7 ºN-35 ºN which is an area shifted by 0.3º to the

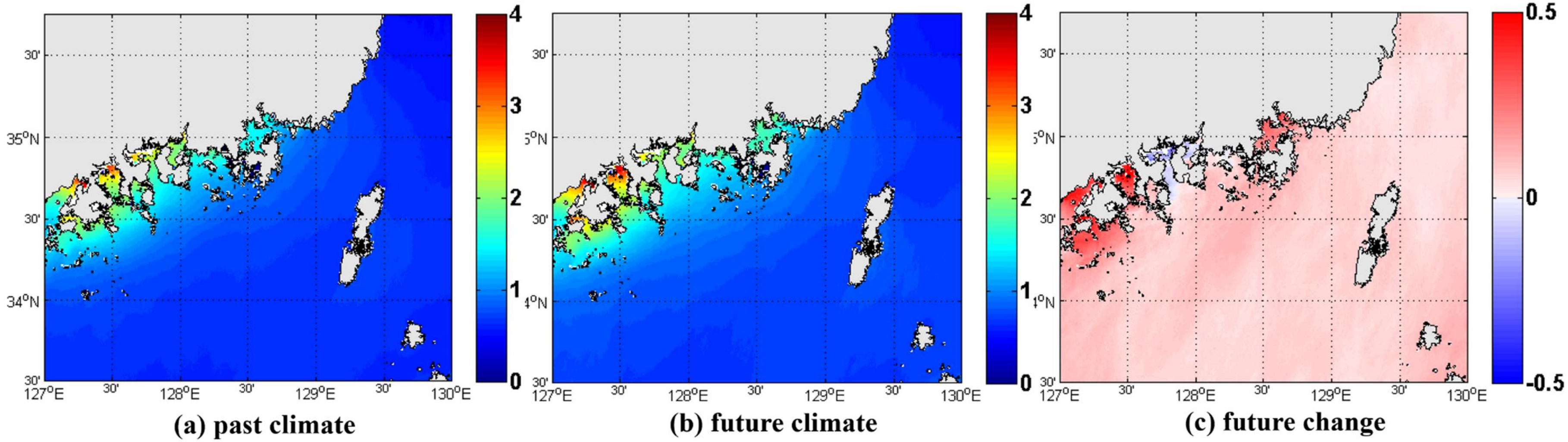

Figure 5.7 Spatial distributions of storm surge heights (m) on the southeastern area of the Korean Peninsula (D4) with 100-year return period. (a) past climate, (b) future climate and (c) future change

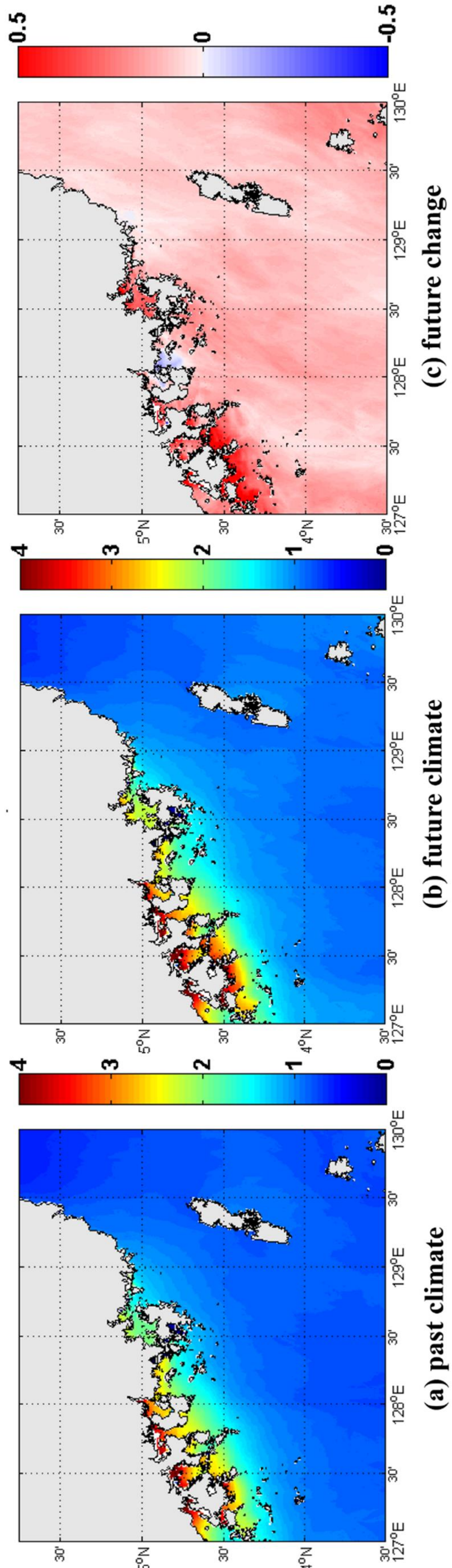

Figure 5.8 Spatial distributions of storm surge heights (m) on the southeastern area of the Korean Peninsula (D4) with 500 -year return period. (a) past climate, (b) future climate and (c) future change

east and 0.1° to the north, compared with one with 100-return period. These differences of the value of the highest SSH and the vulnerable areas according the return period of SSH result mainly from the change in typhoon characteristics over time.

Finally, SSHs with particular return periods on specific locations in D4 is assessed. As shown in Figure 5.9, all the locations have no significant changes for shorter return periods around 50 years. However the differences of SSHs between the past and future climate conditions become clearer for longer than 100-years return periods except few location (e.g. Yoesu). For example, the future change for Gadeokdo, Geomundo, Geojedo and Goheung remain stable until 30-year return period, but it has changed since then. On the other hand, the noticeable future change for Masan, Busan and Tongyeong is shown after 50-year return period. Of the eight locations, the future change is most apparent in Masan. There is no big difference until 50-year return period. From then on there is variation between the past and the future climates and the maximum difference is up to 0.88 m. In the historical, the largest observed SSHs was 2.34 m at Masan tidal station in 2003. This value corresponded one with the 600-year return period under the past climate, but it is expected to occur once in 200-year under the future climate. Minor future change is projected to be shown at Goheung. The maximum difference by climate change is up to 0.3 m. On the other hand, the point with the smallest change in the future climate is Busan. There is no noticeable difference throughout the entire calculation period.

As discussed above, it is expected that the aspect and variation of future change of the SSH for the southeastern area of the KP vary according to the place/region and its return period. This is thought to be due to the increase of the number of strong typhoons affecting the KP and the change of typhoon tracks resulting from climate change. In addition, it is also expected that those for the western area of the KP differ depending on the place/region. The variation of future change of the SSH for the western area is projected to be greater than that of the southeastern area. However, since these founding for the western area is obtained from simulations with a relatively coarse mesh, it is considered to necessary to simulate using a find mesh.

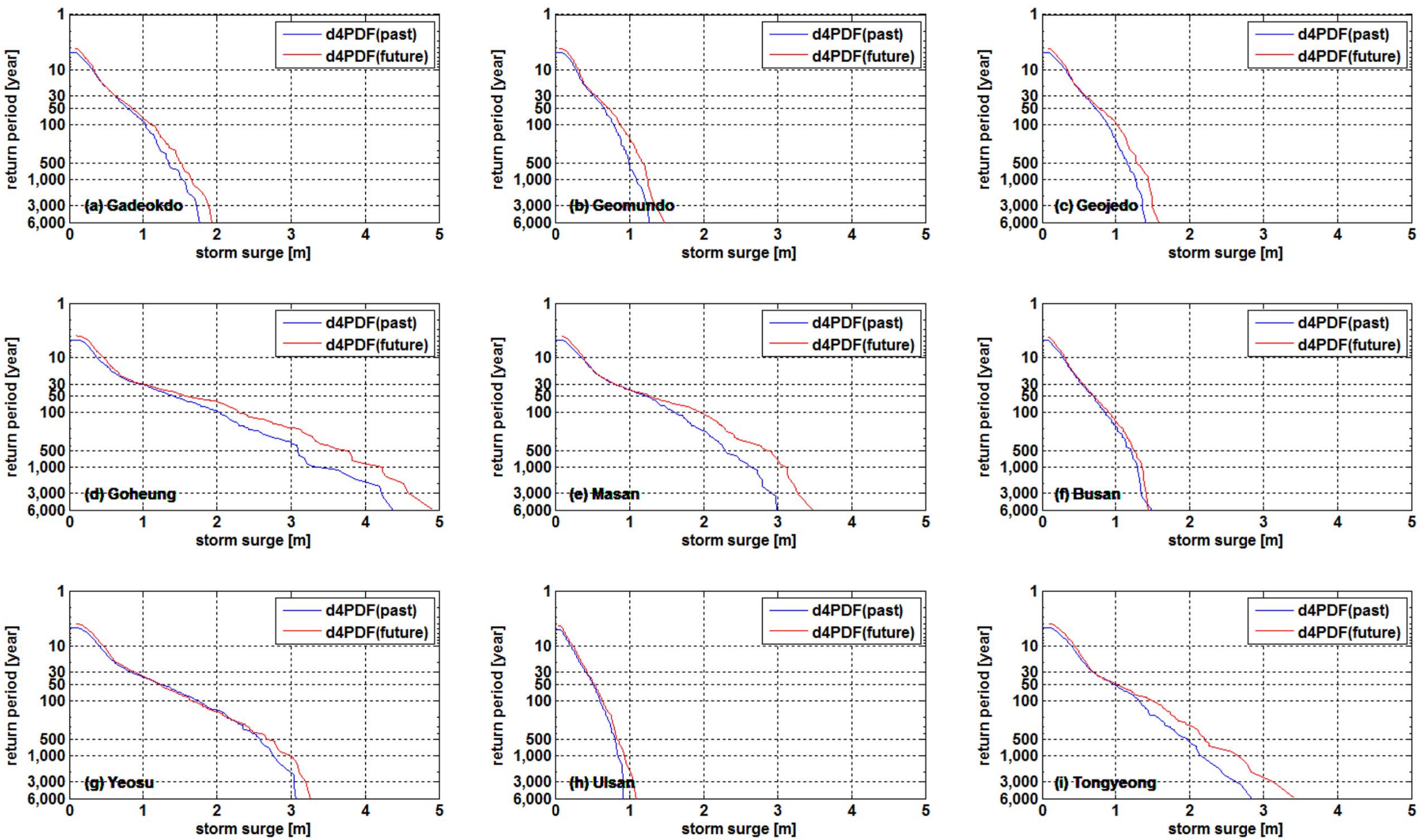

Figure 5.9 Storm surge heights (m) with specific return periods at specific location in the southeastern part of the Korean Peninsula. E ach panel indicate the locations as (a) Gadeokdo, (b) G eomundo, (c) Geojedo, (d) Goheung, (e) Masan, (f) Busan, (g) Yeosu and (h) Tongyeong whose locations are shown in Figure 5.5 (right). Blue and red lines in each panel indicate storm surge heights with specific return periods under past and future climate conditions, respectively.

5.5 Summary

This chapter projected the future storm surge heights around the Korean Peninsula and assessed the its future change based on typhoon data from mega ensemble experiments over 5,000 years using MRI-AGCM3.2H. Here, we used the typhoon data affecting around the Korean Peninsula (hereafter, typhoons around KP) which are pass through the region of 32°N ~ 40°N and 122°E ~ 132°E.

First, the reproducibility of the typhoon data under present climate was estimated by comparison with observed typhoon data. The yearly average number of the typhoons was underestimated comparing to the observations, while the general trend of the tracks of them corresponded with the observations. But, the mega-ensemble experiment produced large samples of storm surge event under past and future climates. As the mean value of the minimum central pressure of them is smaller than observations by 10.35 hPa, the value of minimum central pressure were linearly calibrated. The typhoons with the corrected values were used to project future storm surges.

Nest, future change of the typhoons were assessment. The numbers of typhoons approaching the KP was expected to be significantly reduced in the future climate condition by 38%. The general typhoon tracks including the locations of typhoon genesis and lysis were projected to shift to the northwest. The typhoons under the future climate are stronger than ones under the past climate. Furthermore, significant future change of the minimum central pressure is evident when intense typhoons whose pressures are smaller than 940 hPa.

Finally, to project the future change of storm surge heights, a series of storm surge simulations for the coast in the KP were conducted by using the corrected the typhoons data. The locations of the vulnerable area to storm surge shift to the north area of the western region and to the west area of the southern regions in the KP under the future climate. This characteristic of future change to area where high SSHs occur coincide with one to typhoon track. SSH around the KP is projected to increase under the future climate except for some areas in the south coast. The magnitude of future change of SSH vary spatially. The maximum variation was estimated to 0.61 m (15.4%) with 100-year return period in the west area of the southeastern coast of the Korean Peninsula. In the future, we plan to conduct inundation analysis by selecting several storm surge vulnerable area in the southeastern area

of the KP under the future climate and to re-examine the storm surge heights in the western area of the KP under the past and future climates using a find mesh.

Chapter 6.
Conclusions

Tropical cyclones generating extreme winds, rainfall and storm surge are one of the elements that pose hazards to low lying coastal areas. Among the tropical cyclone-related disasters, salt water flooding associated with storm surge is the primary cause of death. The long-term assessment of storm surge is one of the important factors in coastal risk reduction. Furthermore, it is expected for global climate change resulting in leading to more severe tropical cyclones to change future storm surge heights and other coastal disaster aspects depending on oceans and regions. Therefore, quantifying the impact of climate change on tropical cyclone-induced storm surges requires explicit modeling of the development of storms and induced surges at regional scales under projected climates.

This study was conducted targeting the Korean Peninsula (hereafter, KP) which located in Northwest Pacific region toward following objectives:

(1) To identify a storm surge vulnerable region around the KP under the past climate

(2) To evaluate the reproducibility of the numerical model for a regional scale by considering various typhoons characteristics and topographic features of the coastline

(3) To suggest a method to improve the reproducibility of the numerical model considering topographic characteristics of the coastline

(4) To assess the uncertainties of projection of future SSHs based on results of ensemble experiments with different global warming scenarios and different spatial pattern of sea surface temperatures (hereafter, SST) using a single global climate model (hereafter, GCM)

(5) To project future SSHs based on results of mega ensemble experiments using a single GCM and to identify a storm surge vulnerable region around the KP under the future climate

Main finding in the study are summarized below.

In the Chapter 2, the storm surge heights higher than 1 m were observed at 10 tidal stations in the southern coastal area and at 3 tidal stations in the western coastal area since 2000. Value of the highest storm surge height became 2.61 m which was observed at Yeosu tidal station in the southern coastal area. Six typhoons produced the storm surge heights of over 1.0 m around the KP. In addition, a series of hindcasting of storm surge for the southeastern coastal area by the six typhoons was conducted to evaluate the reproducibility of numerical model according to typhoon characteristics and the different terrain characteristics. It was found that when the distance between the center of the typhoon and the tidal station is small and the tidal station is located to the right side of the typhoon track, the storm surge heights tend to be overestimated. This is especially pronounced among tidal stations that have complex coastlines. However, when the distance between them is large, the storm surge heights tend to be underestimated regardless of relative position between them. So, it is necessary to consider topographical features to correct the bias.

In chapter 3, the formulas for the model bias correction using the coastline complexity factors were drawn and validated. The simulated results for four of the six typhoons were used to derive the bias correction formulas. The proposed bias correction formulas improved the modelὂs performance by 18 % to 30 %. In validation, the simulated results of the remaining two were used. The RMSE of results without bias correction was reduced by 11 % to 14 % by applying the bias correction method. In general, the root mean square error of results with bias correction decreased by 14 % to 23 % by applying the bias correction. It can be seen that the bias correction method considering the coastline complexity can improve modelǿs accuracy.

Chapter 4 discussed the uncertainties of the projection of the storm surge heights under present and future climate conditions based on projected typhoons by ensemble experiments with three global warming scenarios and four spatial pattern of sea surface temperatures (SST) using MRI-AGCM3.2H. A series of storm surge simulations for the coast in the KP were conducted by using the typhoons data from each ensemble experiment. The vulnerable area to future storm surge and the extent of future SSHs depend on the spatial pattern of SST and the global warming scenario.

Chapter 5 projected the future storm surge heights around the KP and assessed the its future change based on typhoon data from mega ensemble experiments over 5,000 years using MRI-AGCM3.2H. The locations of the vulnerable area to storm surge shift to the north area of the western region and to the west area of the southern regions in the KP under the future climate. This characteristic of future change to area where high SSHs occur coincide with one to typhoon pathway. SSH around the KP is projected to increase under the future climate except for some areas in the south coast. The magnitude of future change of SSH vary spatially. The maximum variation was estimated to 0.61 m (15.4%) with 100-year return period in the west area of the southeastern coast of the Korean Peninsula.

In the future, we plan to conduct inundation analysis by selecting several vulnerable area to storm surge under the future climate.

Reference

Ahn, S.H., Kim, B.J., Lee, S.L. and Kim, H.K., 2008. The Characteristics of Disaster by Track of Typhoon Affecting the Korean Peninsula. *Journal of the Korean Society of Hazard Mitigation*, **8**, pp. 29-36.

Anthes, R.A., 1982. Tropical Cyclones, their Evolution, Structure and Effects. 1st Edition, American Meteorological Society, pp. 208.

Arakawa, A. and Schubert, W. H., 1974. Interaction of cumulus cloud ensemble with the large-scale environment, Part I. *Journal of the Atmospheric Sciences*, **31**, pp.674-701.

Bender, M.A., Kuntson, T.R., Tuleya, J.J., Sirutis, J.J., Vecchi, G.A., Garner, S.T. and Held, I.M., 2010. Modeled impact of anthropogenic warming on the frequency of intense Atlantic hurricanes, *Science*, **327**, pp.454-458.

Bengtsson, L., Hodges, K.I, Esch, M., Keenlyside, N., Kornblueh, L., Luo, J.J. and Yamagata, T., 2007. How may tropical cyclones change in a warmer climate? *Tellus*, **59**, pp.539-561.

Bourke, R. H. and Garrett, R. P., 1987. Sea ice thickness distribution in the Arctic Ocean. *Cold Regions Science and Technology*, **13**, pp.259ï 280.

Carr, J.R. and Benzer, W.B., 1991. On the practice of estimating fractal dimension. *Mathematical Geology,* **23**, pp.945-958. DOI: 10.1007/BF02066734.

Cha, S.H. and Kwon, K.W., 2001. The Analysis of Fractal Characteristics in River Basin using GIS. *Journal of the Korean Association of Geographic Information Studies,* **4**, pp.51-60.

Choi, E.S. and Moon, I.J., 2008. The variation of extreme values in the precipitation and wind speed during 56 years I Korea, *Atmosphere*, **18**, pp.397-416.

Choi, H.W. and Chang, T.W., 1999. Properties and Fractal Analysis of Joints around the Moryang Fault. *Journal of Engineering Geology,* **9**, pp.119-134.

Choi, K.S. and Kim, B.J., 2007. Climatological characteristics of tropical cyclones making landfall over the Korean Peninsula. *Journal of the Korean Meteorological Society*, **43**, pp. 97-109.

Coupled Model Intercomparison Project Phase 3 (CMIP3), 2007. http://www-pcmdi.llnl.gov/ipcc/about_ipcc.php Last access May 29, 2017.

Deser, C., Phillips, A., Bourdette, V. and Teng, H., 2012. Uncertainty in climate change projections: the role of internal variability. *Climate Dynamics*, **38**, pp.527ï 546.

Deushi, M. and Shibata, K., 2011. Development of a Meteorological Research Institute Chemistry-Climate Model version 2 for the Study of Tropospheric and Stratospheric Chemistry. *Papers in Meteorology and Geophysics*, **62**, pp.1ï 46.

Digital Typhoon Data Base, 2014. Typhoon images and information. http://www.digitaltyphoon.org/. Last access August 1, 2016.

Elsner, J.B., Kossing, J.P. and Jagger, T.H., 2008. The increasing intensity of the strongest tropical cyclones. *Nature*, **455**, pp.92-95.

Emanuel, K., 2005. Increasing destructiveness of tropical cyclones over the past 30 years, *Nature*, **436**, pp.686-688.

Foreman, M.G.G. and Neufeld, E.T., 1991. Harmonic tidal analyses of long time series. *International Hydrographic Review,* **68**, pp.85ï 108.

Fractalfoundation, 2016. Fractal Dimension of Coastlines. http://fractalfoundation.org/OFC/OFC-10-4.html. Last access August 1, 2016.

Fujita, T., 1952. Pressure distribution within typhoon. Geophysical Magazine, 23, pp.437-451.

General Bathymetric Chart of the Oceans (GEBCO). 2003. British Oceanographic Data Centre Centenary Edition.

Godin, G., 1991. The analysis of tides and currents. In: Parker, B.B (Ed.), Tidal Hydrodynamics. Wiley, New York, pp.675ï 709.

Goto, C. and Sato, K., 1993. Development of Tsunami numerical simulation system for Sanriku Coast in Japan. *Report of the Port and Harbor Research Institute.* **32**, pp.3-44 (in Japanese).

Grassberger, P., 1983. On efficient box counting algorithms. International Journal of Modern Physics C, **4**, pp. 515ï 523.

Hirahara, S., Ishii, M. and Fukuda, Y., 2014. Centennial-scale sea surface temperature analysis and its uncertainty. *Journal of Climate*, **27**, pp.57ï 75. doi: 10.1175/JCLI-D-12-00837.1.

Hjelmfelt, A. T., 1988. Fractals and the river length-catchment area ratio. *Water Resources Bulletin,* **24**, pp.455-370.

Hur, D.S., Yeom, G.S., Kim, J.M., Kim, D.S. and Bae, K.S., 2006(a). Estimation of Storm Surges on the Coast of Busan. *Journal of Ocean Engineering and Technology*, **20**, pp.37-44.

Hur, D.S., Yeom, G.S., Kim, J.M., Kim, D.S. and Bae, K.S., 2006(b). Storm Surge Characteristics According to the Local Peculiarity in Gyeongnam Coast. *Journal of Ocean Engineering and Technology*, **20**, pp.45-53.

Intergovernmental Panel on Climate Change (IPCC), 2007. The physical science basis. Contribution of working group I to the fourth assessment report of the intergovernmental panel on climate change. Cambridge. pp. 976.

Intergovernmental Panel on Climate Change (IPCC). 2013. Climate change 2013: The physical science basis. Contribution of working group I to the fifth assessment report of the intergovernmental panel on climate change. Cambridge University Press, Cambridge, UK and New York, USA; 1533. DOI:10.1017/CBO9781107415324.

Kain, J.S. and Fritsch, J.M., 1993. Convective parameterization for mesoscale models: the Kainï Fritsch scheme. The representation of cumulus convection in numerical models. *American Meteorological Society*, pp 165-170

Kang, T.S., Moon, S.R., Nam, S.Y. and Shim, J.S., 2010. The Vulnerability of the Reclaimed Seashore Land Attendant Upon Storm Surge/Coastal Inundation. *Journal of Ocean Engineering*, **24**, pp.68-75.

Kay, J. E., Deser, C., Phillips, A., Mai, A., Hannay, C., Strand, G., Arblaster, J.M., Bates, S.C., Danabasoglu, G., Edwards, J., Holland, M., Kushner, P., Lamarque, J.F., Lawrence, D., Lindsay, K., Middleton, A., Munoz, E., Neale, R., Oleson, K., Polvani, L. and Vertenstein, M., 2015: The Community Earth System Model (CESM) Large Ensemble Project: A Community Resource for Studying Climate Change in the Presence of Internal Climate Variability. *Bulletin of the American Meteorological Society*, **96**, 1333ï 1349.

Kim, S.Y., 2007. Effect of large tidal variation on storm surge in the western coastal sea of Korea. Ph.D thesis. Kyoto University.

Kim, S.Y., Oh, J.H., Suh, K.D., Yasuda, T. and Mase, H., 2014. Evaluation of storm surges around the Korean peninsula in present and future climates. *Proceedings of the Thirty-Fourth International Conference on Coastal Engineering*, Seoul, Korea, June 15-20, 2014.

Kim, S.Y., Yasuda, T. and Mase, H., 2008. Numerical analysis of effects of tidal variations on storm surges and waves. *Applied Ocean Research*, **30**, pp. 311-322.

Kitoh, A. and Endo, H., 2016. Changes in precipitation extremes projected by a 20-km mesh global atmospheric model. *Weather and Climate Extremes*, **11**, pp.41-52.

Kitoh, A., Ose, T., Kurihara, K., Kusunoki, S., Sugi, M. and KAKUSHIN Team-3 Modeling Group, 2009. Projection of changes in future weather extremes using super-high-resolution global and regional atmospheric models in the KAKUSHIN Program: Results of preliminary experiments. *Hydrological Research Letters*, **3**, pp.49ï 53, doi:10.3178/hrl.3.49.

Klinkenberg, B., 1992. The fractal properties of topography: A comparison of methods. *Earth Surface Processes and Landforms,* **17**, pp.217-234.

Klinkenberg, B., 1994. A review of methods used to determine the fractal dimension of linear features. *Mathematical Geology,* **26**, pp.23-46.

Knabb, R.D., Rhome, J.R. and Brown D.P., 2005. Tropical cyclone report Hurricane Katrina 23-30 August 2005. National Hurricane Center, p.43.

Knapp, K.P., Kruk, M.C., Levinson, D.H., Diamond, H.J. and Neumann, C.J., 2010. The international best track archive for climate stewardship (IBTrACS) unifying tropical cyclone data. *Bulletin of the American Meteorological Society*, **91**, pp.363-376.

Kuntson, T.R., McBride, J.L., Chan, J., Emanuel, K., Holland, G., Landsea, C., Held, I., Kossin, J.P., Srivastava, A.K. and Sugi, M., 2010. Tropical cyclones and climate change. *Nature Geoscience*, **3**, pp. 157-163.

Kwon, J.I., Park, K.S., Lee, J.C., Jun, K.C., Lee, D.Y. and Lim, H.S., 2007. An operational prediction system for storm surges in the Korean Coast. JCOMM Scientific and Technical Symposium on Storm Surges, 2-6 October, 2007, Seoul, Republic of Korea

Lapidez, J.P., Tablazon, J., Dasallas, L., Gonzalo, L.A., Cabacaba, K.M., Ramos, M.M.A., Suarez, J.K., Santiago, J., Lagmay, A.M.F. and Malano, V., 2015. Identification of storm surge vulnerable areas in the Philippines through the simulation of Typhoon Haiyan-induced storm surge levels over historical storm tracks. *Natural Hazards and Earth System Sciences*, **15,** pp.1473-1481. DOI: 10.5194/nhess-15-1473-2015.

Lin, N., Emanuel, K., Oppenheimer, M. and Vanmarcke, E., 2012. Physically based assessment of hurricane surge threat under climate change. *Nature climate change*, **2**, pp.462-467.

Makkonen, L., 2006. Plotting position in extreme value analysis. *Journal of Applied Meteorology and Climatology*, **45**, pp.334-340.

Mandelbrot, B. B., 1967. How long is the coast of Britain? Statistical self-similarity and fractional dimension. *Science,* **156**, pp.636-638.

Mandelbrot, B. B., 1982. The fractal geometry of nature: W. H. Freeman, San Francisco, 468 p.

Marani, A., Rigon, R. and Rinaldo, A., 1991. A note on fractal channel networks. *Water Resources Research,* **27**, pp.3041-3049.

Matsumoto, K., Takanezawa, T. and Ooe, M., 2000. Ocean tide models developed by assimilating TOPEX/POSEIDON altimeter data into hydro-dynamical model: A global model and a regional model around Japan. *Journal of Oceanography,* **56**, pp.567-581.

Mizuta, R., Murata, A., Ishii, M., Shiogama, H., Hibino, K., Mori, N., Arakawa, O., Imada, Y., Yoshida, K., Aoyagi, T., Kawase, H., Mori, M., Okada, Y., Shimura, T., Nagatomo, T., Ikeda, M., Endo, H., Nosaka, M., Arai, M., Takahashi, C., Tanaka, K., Takemi, T., Tachikawa, Y., Temur, K., Kamae, Y., Watanabe, M., Sasaki, H., Kitoh, A., Takayabu, I., Nakakita, E. and Kimoto, M., 2016. Over 5000 years of ensemble future climate simulations by 60 km global and 20 km regional atmospheric models. *Bulletin of the American Meteorological Society*. doi:10.1175/BAMS-D-16-0099.1, in press.

Mizuta, R., Oouchi, K., Yoshimura, H., Noda, A., Katayama, K., Yukimoto, S., Hosaka, M., Kusunoki, S., Kawai, H. and Nakagawa, M., 2006. 20-km-mesh global climate simulations using JMA-GSM modelð mean climate statesð . *Journal of the Meteorological Society of Japan*, **84**, pp.165-185, doi:10.2151/jmsj.84.165.

Mizuta, R., Osamu, A., Tomoaki, O., Kusunoki, S., Endo, H. and Kitoh, A., 2014. Classification of CMIP5 Future Climate Responses by the Tropical Sea Surface Temperature Changes. *SOLA*, **10**, pp. 167-171.

Mizuta, R., Yoshimura, H., Murakami, H., Matsueda, M., Endo, H., Ose, T., Kamiguchi, K., Hosaka, M., Yukimoto, S., Kusunoki, S. and Kitoh, A., 2012. Climate Simulation Using MRI-AGCM3.2 with 20-km Grid. *Journal of the Meteorological Society of Japan*, **90A**, pp.233-258. DOI:10.2151/jmsj.2012-A12.

Moon, S.R., Kang, T.S., Nam, S.Y. and Hwang, J., 2007. A Study on Scenario to establish Coastal Inundation Prediction Map due to Storm Surge. *Journal of Korean Society of Coastal and Ocean Engineers*, **19**, pp.492-501.

Moon, S.R., Park, S.J., Kang, J.W. and Yoon, J.T., 2006. Numerical Simulations of Storm Surge/Coastal Flooding at Mokpo Coastal Zone by MIKE21 Model, *Journal of Korean Society of Coastal and Ocean Engineers*, **18**, pp.348-359.

Mori, N. and Takemi, T., 2016. Impact assessment of coastal hazards due to future changes of tropical cyclones in the North Pacific Ocean. *Weather and Climate Extremes*, **11**, pp. 53-69.

Murakami, H. and Sugi, M., 2010. Effect of model resolution on tropical cyclone climate projections. *SOLA*, **6**, pp.73-76

Murakami, H., Mizuta, R. and Shindo, E., 2012a. Future changes in tropical cyclone activity projected by multi-physics and multi-SST ensemble experiments using the 60-km-mesh MRI-AGCM. *Climate Dynamics*, **39**, pp. 2569-2584.

Murakami, H., Mizuta, R. and Shindo, E., 2012b. Future changes in tropical cyclone activity projected by multi-physics and multi-SST ensemble experiments using the 60-km-mesh MRI-AGCM. *Climate Dynamics*, **39**, pp. 2569-2584.

Murakami, H., Wang, B. and Kitoh, A., 2011. Future change of western North Pacific typhoons: projections by a 20-km-mesh global atmospheric model. *Journal of Climate*, **24**, pp.1154-1169.

Murakami, H., WANG, Y., Yoshimura, H., Mizuta, R., Sugi, M., Shindo, E., Adachi, Y., Yukimoto, S., Hosaka, M., Kusunoki, S., Ose, T. and Kitoh, A., 2012a. Future Changes in Tropical Cyclone Activity Projected by the New High-Resolution MRI-AGCM. *American Meteorological Society*, **25**, pp.3237-3260.

Nakajo, S., Fujiki, H., Kim, S.Y., Mori, N., Shibutani, Y. and Yasuda, T., 2015. A Parametric study on potential of storm surge in Tokyo bay. *Journal of Japan Society of Civil Engineers Series B2 (Coastal Engineering),* **71**, pp.199-204. DOI: 10.2208/kaigan.71.I_199.

Nakajo, S., Mori, N., Kim, S.Y. and Yasuda, T., 2013. Consideration of applicability of stochastic tropical cyclone model for probability assessment of storm surge. *Proceedings of 7th International Conference on Asian Pacific Coasts,* September 24-26, 2013 Bali, Indonesia; pp.613-619.

National Disaster Risk Reduction and Management Council, 2013. FINAL REPORT re EFFECTS of Typhoon ñYOLANDAò(HAIYAN), SitRep 60, NDRRMC, Quezon City, Philippines.

National Typhoon Center (NTC), 2016. http://typ.kma.go.kr/TYPHOON/statistics/statistics_02_1.jsp. Last access August 1, 2016.

Oh, J.H., Shu, K.D. and Kim, Y.O., 2011. Trend Analyses of Intensity and Duration of Typhoons That Influenced the Korean Peninsula during Past 60 Years. *Journal of the Korean Society of Civil Engineers*, **31**, pp. 121-128.

Okubo, P.G. and Aki, K., 1987. Fractal Geometry in the San Andreas Fault System, *Journal of Geophysical Research,* **92**, pp. 345-355.

Oouchi, K., Yoshimura, J., Yoshimura, H., Mizuta, R., Kusunoki, S. and Noda, A., 2006. Tropical cyclone climatology in a global-warming climate as simulated in a 20 km-mesh global atmospheric model: Frequency and wind intensity analysis. *Journal of the Meteorological Society of Japan*, **84**, pp.259-276.

Park, J.K., Kim, B.S., Jung, W.S., Kim, E.B. and Lee, D.G., 2006. Change in Statistical Characteristics of Typhoon Affecting the Korean Peninsula. *Atmosphere*, **16**, pp. 1-17.

Park, K.S., Lee, J.C., Jun, K.C., Kim, S.I. and Kwon, J.I., 2009. Development of an Operational Storm Surge Prediction System for the Korean Coast. *Ocean and Polar Research*, **31**, p.369-377.

Pawlowicz, R., Beardsley, B. and Lentz, S., 2002. Classical tidal harmonic analysis including error estimates in MATLAB using T_TIDE. *Computers & Geosciences,* **28**, pp.929-937.

Philip, S.R. 1994. Structural and lithological controls on coastline profiles in Fife, *Eastern Britain. Terra Nova,* **6**, pp.251-254. DOI: 10.1111/j.1365-3121.1994.tb00492.x.

Randall, D. and Pan, D.M., 1993. Implementation of the Arakawaï Schubert cumulus parameterization with a prognostic closure. The representation of cumulus convection in numerical models. *American Meteorological Society*, pp.137-144.

Rayner, N.A., Parker, D.E., Horton, E.B., Folland, C.K., Alexander, L.V. and Rowell, D.P., 2003. Global analysis of sea surface temperature, sea ice, and night marine air temperature since the late nineteenth century. *Journal of Geophysical Research*, **108**, 4407.

Rosso, R., Bacchi, B. and Barbera, P.L., 1991. Fractal relation of mainstream length to catchment area in river networks. *Water Resources Research,* **27**, pp.381-387.

Rozynski, G., Hung, N.M. and Ostrowski, R., 2009. Climate change related rise of extreme typhoon power and duration over South-East Asia Seas. *Coastal Engineering Journal*, **51**, pp.205-222.

Schiermeier, Q., 2010. Most powerful hurricanes on the rise, *Nature*, doi:10.1038/news.2010.24.

Seo, S.N., 2008. Digital 30sec gridded bathymetric data of Korea Marginal Seas ï KorBathy30s. *Journal of Korean Society of Coastal and Ocean Engineers*, **20**, pp.110-120.

Shibutani, Y., Nakajo, S., Mori, N., Kim, S.Y. and Mase, H., 2015. Estimation of worst-class tropical cyclone and storm surge and its return period ï case study for Ise Bay -. *Journal of Japan Society of Civil Engineers series B2 (Coastal Engineering),* **71**, pp.1513-1518. DOI: 10.2208/kaigan.71.I_1513.

Shim, J.S., Min, I.K. and Yoon, J.J., 2017. Hydraulic Experiments on Sinkable Floating Storm Surge Barrier under Various Wave Actions. *Journal of Coastal Research*, **79**, pp.184-188.

Stowasser, M., Wang, Y. and Hamilton, K., 2007. Tropical cyclone changes in the western North Pacific in a global warming scenario. *Journal of Climate*, **20**, pp.2378-2396.

Sugi, M., Murakami, H., Yoshimura, J., 2009. A reduction in global tropical cyclone frequency due to global warming. *SOLA*, **5**, pp.164-167.

Suh, S.W., Lee, H.Y., Kim, H.J. and Park, J.S., 2012. Near Real-time Immediate Forecasting of Storm Surge Based on Typhoon Advisories. *Journal of Korean Society of Coastal and Ocean Engineers*, **24**, pp.352-365.

Takayama, T., 2002. Present numerical simulations of storm surge and their problems to solve, *Lecture Notes of the 38th Summer Seminar on Hydraulic Engineering,* 02-B-6.

Takayama, T., Amamori, H., Kim, T.M., Mase, H., Kang, Y.K. and Kawai, H., 2004. Characteristics of storm surge and wave disasters caused by Typhoon 0314 (MAEMI) in Korea. *Annuals of Disaster Prevention Research Institute Kyoto University,* **47A**, pp.99-111.

Tarboton, D. G., Bras, R. L. and Itrube, I.R., 1988. The fractal nature of river networks. *Water Resources Research,* **24**, pp.1317-1322.

United Nations Atlas of the Oceans, 2016. Facts. http://www.oceansatlas.org/facts/en/. Last access May 1, 2017

Unoki, S. and Isozaki, I., 1966. Study on atmospheric pressure and wind effects comparison in the storm surge. *Journal of Japan Society of Civil Engineers Series B2 (Coastal Engineering),* **13**, pp.248-253.

Vousdoukas, M.I., Voukouvalas, E., Annunziato, A., Giardino, A. and Feyen, L., 2016. Projections of extreme storm levels along Europe. *Climate Dynamics,* **47**, pp.3171-3190. DOI: 10.1007/s00382-016-3019-5.

Walsh, K., Lavender, S., Murakami, H., Scoccimarro, E., Caron, L.P. and Ghantous, M., 2010. The tropical intercomparison project. Hurricanes and climate change. Springer, Berlin, pp.1-24.

Walsh, K.J.E., Fiorino, M., Landsea, C.W. and McInnes, K.L., 2007. Objectively determined resolution-dependent threshold criteria for the detection of tropical cyclones in climate models and reanalyses. *Journal of Climate*, **20**, pp.2307-2314.

Webster, P.J., Holland, G.L., Curry, J.A. and Chang, H.R., 2005. Changes in tropical cyclone number, duration, and intensity in a warming environment. *Science*, **16**, pp.1844-1846.

Weibull, W., 1939. A statistical theory of strength of materials. *IVB-Handlingar,* **151**, pp.1-45.

Wessel, P. and Smith, W.H.F., 1996. A global self-consistent, hierarchical, high-resolution shoreline database. *Journal of Geophysical Research,* **101**, pp.8741-8743. DOI: 10.1029/96JB00104.

WMO, 2006. Statement on tropical cyclones and climate change. WMO/CAS tropical meteorology research program report 4.

Woodruff, J.D., Irish, J.L. and Camargo, S.J., 2013. Coastal flooding by tropical cyclones and sea-level rise, *Nature,* **504**, pp.44-52.

Yang, S.K. and Kim, S.B., 2014. A Height Simulation on Storm Surges in Jeju Island. *Journal of Environmental Science International*, **23**, pp. 459-472.

Yasuda, T., Hayashi, Y., Mori, N. and Mase, H., 2010. A Stochastic Typhoon Model Applicable to Storm Surge and Wave Simulations for Climate Change Projection. *Journal of Japan Society of Civil Engineers Series B2 (Coastal Engineering),* **66**, pp.1241-1245.

Yasuda, T., Nakajo, S., Kim, S.Y., Mase, H., Mori, N. and Horsburgh, K., 2014. Evaluation of Future Storm Surge Risk in East Asia based on State-of-the-art Climate Change Projection. *Coastal Engineering,* **83**, pp.65ï 71. DOI: 10.1016/j.coastaleng.2013.10.003.

Yasuda, T., Nakajo, S., Kim, S.Y., Mase, H., Mori. N. and Horsburgh, K., 2014. Evaluation of future storm surge risk in East Asia based on state-of-the-art climate change projection. *Coastal Engineering*, **83**, pp. 65-71.

Yokoi, S. and Takayabu, Y.N., 2009. Multi-model projection of global warming impact on tropical cyclone genesis frequency over the western North Pacific. *Journal of the Meteorological Society of Japan*, **87**, pp.525-538.

Yokoi, S., Takayabu, Y.N. and Chan, J.C.L., 2009. Tropical cyclone genesis frequency over the western North Pacific simulated in medium resolution coupled general circulation models. *Climate Dynamics*, **33**, pp.665ï 683

You, S.Y. and Seo, J.W., 2009. Numerical Study of Storm Surges and Tide around Korea Using Operational Ocean Model. *Marine Geodesy*, **32**, pp.243-263, DOI: 10.1080/01490410902869656

Yukimoto, S., Adachi, Y., Hosaka, M., Sakami, T., Yoshimura, H., Hirabara, M., Tanaka, T.Y., Shindo, E., Tsujino, H., Deushi, M., Mizuta, R., Yabu, S., Obata, A., Nakano, H., Koshiro, T., Ose, T. and Kitoh, A., 2012. A new global climate model of Meteorological Research Institute: MRI-CGCM3ð model description and basic performanceð . *Journal of Meteorological Society of Japan*, **90**, pp.23ï 64. doi:10.2151/jmsj.2012-A02.

Yukimoto, S., Yoshimura, H., Hosaka, M., Sakami, T., Tsujino, H., Hirabara, M., Tanaka, T.Y., Deushi, M., Obata, A., Nakano, H., Adachi, Y., Shindo, E., Yabu, S., Ose, T. and Kitoh, A., 2011. Meteorological research institute-earth system model v1 (MRI-ESM1)ð model description. Technical Reports of the Meteorological Research Institute, 64, 88pp.

Zhao, M., Held, I.M., Lin, S.J. and Vecchi, G.A., 2009. Simulations of global hurricane climatology, interannual variability, and response to global warming using a 50 km resolution GCM. *Journal of Climate*, **22**, pp.6653-6678

Zhu, X., Cai, Y., Yang, X., 2004. On Fractal Dimensions of Chinaŝ Coastlines. *Mathematical Geology,* **36**, pp.447-461. DOI: 10.1023/B:MATG.0000029299.02919.f8.